PERMEABLE AND STRETCHABLE BIOELECTRONIC DEVICES AND SYSTEMS USING LIQUID METAL

ZHUANG QIUNA

PhD

The Hong Kong Polytechnic University

2024

The Hong Kong Polytechnic University

School of Fashion and Textiles

Permeable and Stretchable Bioelectronic Devices and Systems Using Liquid Metal

Zhuang Qiuna

A thesis submitted in partial fulfilment of the requirements

for the degree of Doctor of Philosophy

August 2023

CERTIFICATE OF ORIGINALITY

I hereby declare that this thesis is my own work and that, to the best of my knowledge and belief, it reproduces no material previously published or written, nor material that has been accepted for the award of any other degree or diploma, except where due acknowledgement has been made in the text.

_____(Signed)

Qiuna Zhuang (Name of Student)

Abstract

Permeable stretchable electronics have emerged as a promising avenue for next-generation bio-integrated electronics due to their ability to enhance physiological comfort during long-term wear. However, existing technologies lack a universal fabrication method for incorporating permeable stretchable materials into a mass-producible way. Furthermore, highly stretchable 3D integrated circuits with complex functions and skin-like softness and permeability are yet to be achieved.

This study presents a wafer-scale patternable strategy for the high-resolution fabrication of supersoft, stretchable, and permeable liquid metal microelectrodes (Plms) and their implantation as a neural interface for high spatiotemporal mapping and intervention of electrocorticography (ECoG) signals in living rats. In addition, a micropatterning technology of PlmHs on polyacrylic acid (PAA) hydrogels has been developed for permeable transparent bioelectronics. Finally, a permeable and 3D integrated electronic skin (WPE-skin) possessing skin-like softness and stretchability, outstanding permeability, and robust electronic integration capable of sensing, signal processing, analysis, intervention, and communication in a wireless manner has been proposed. The comprehensive studies open a new avenue to bridge soft and stretchable biology with electronic functions and integrations using LM.

In summary, this work studied the feasibility of developing permeable stretchable LM-based bioelectronics consisting of materials, fabrications, devices, and systems. Various LM-based bioelectrodes, bioelectronic devices, and systems have been successfully demonstrated. Such comprehensive studies open a new avenue to bridge soft and stretchable biology with electronic functions and integrations using LM. In principle, these fabrication and integration strategies are expected to have significant impact in permeable bioelectronics are also versatile to other bioelectronic devices and systems.

List of Publications

Published Papers:

1. **Q. Zhuang**, …, X. Yu*, Z. Zheng*, Wafer-patterned, permeable, and stretchable liquid metal microelectrodes for implantable bioelectronics with chronic biocompatibility, *Sci. Adv.* 9, eadg8602 (2023) (Featured article).

2. **Q. Zhuang**, …, Q. Huang*, Z. Zheng*, Liquid-metal-superlyophilic and conductivity-strain-enhancing scaffold for permeable superelastic conductors, *Adv. Funct. Mater.*, 31, 2105587 (2021).
3. Z. Ma, Q. Huang, Q. Xu, **Q. Zhuang**, …, Z. Zheng*, Permeable superelastic liquid-metal fibre mat enables biocompatible and monolithic stretchable electronics. *Nat. Mater.* 20, 859–868 (2021)
4. S. Wang, Y. Gao*, Q. Huang, X. Guo, A. Yang, Y. Zhang, **Q. Zhuang**, …, Z. Zheng*, Inkjet-Printed Xerogel Scaffolds Enabled Room-Temperature Fabrication of High-Quality Metal Electrodes for Flexible Electronics, *Adv. Funct. Mater.*, 32, 2203730 (2022)
5. Y. Gao, H. Hu, J. Chang, Q. Huang, **Q. Zhuang**, …, Z. Zheng*, Realizing High-Energy and Stable Wire-Type Batteries with Flexible Lithium-Metal Composite Yarns, *Adv. Energy Mater.*, 11, 2101809 (2021)
6. Z. Ma, Q. Huang, N. Zhou, **Q. Zhuang**, …, Z. Zheng*, Stretchable and conductive fibers fabricated by a continuous method for wearable devices, *Cell Reports Physical Science*, 4, 101300, (2023)
7. J. Chang, H. Hu, J. Shang, R. Fang, D. Shou, C. Xie, Y. Gao, Y. Yang, **Q. Zhuang**, …, Z. Zheng*, Rational Design of Li-Wicking Hosts for Ultrafast Fabrication of Flexible and Stable Lithium Metal Anodes, *Small*, 18, 2105308 (2022)

8. Q. Liu, Zhenlu Yu, **Q. Zhuang**, …, B. Zhang*Anti-Fatigue Hydrogel Electrolyte for All-Flexible Zn-Ion Batteries, *Adv. Mater.*, 35, 2300498, (2023).
9. F. Chen, **Q. Zhuang**, …, Z. Zheng*, Wet-adaptive electronic skins, *Adv. Mater.*, 35, 2305630, (2023)
10. M. Wu, **Q. Zhuang**, …, X. Yu*, Stretchable, Skin-Conformable Neuromorphic System for Tactile Sensory Recognizing and Encoding, *InfoMat*, 5, e12472 (2023)

Paper in Preparation:

1. **Q. Zhuang**, …, X. Yu*, Z. Zheng*, Wireless permeable three-dimensional integrated electronic skins, In preparation
2. **Q. Zhuang**, …, X. Yu*, Z. Zheng*, Wafer-patterned and tissue-like hydrogel microelectrodes for conformal, transparent, and low-impedance biointerfaces. In preparation

Patent:

1. Wafer-scale-patterned, permeable, and stretchable liquid metal microelectrodes for implantable bioelectronics with chronic biocompatibility, Z. Zheng, **Q. Zhuang**, 19 Jan. 2023 (Filed), US 63/480,603
2. Tensile conductive yarn and manufacturing method therefor, Z. Zheng, Z., Ma, **Q. Zhuang**, 05 May 2022, WO 2022/089510 A1

Acknowledgements

I am grateful for the opportunity to pursue my Ph.D. studies under the guidance of my supervisor, Prof. ZHENG Zijian. His extensive knowledge and insightful opinions have been invaluable to me throughout my research journey. I would also like to express my appreciation to Prof. Xinge Yu for his encouragement and advice during times of struggle.

I am thankful to the members of our research group, AIMD, for their enthusiasm and willingness to help others. I would like to give special recognition to Dr. Kuanming Yao, Dr. Qiyao Huang, Dr. Quanjing Mei, Dr. Chi Zhang, Dr. Zhuogui Lei, Ms. Mengge Wu, Mr. Fan Chen, Dr. Xian Song, and Dr. Yufei Zhang for their instructive discussions, professional training, and selfless assistance during my lab activities.

I also want to acknowledge myself for persevering in pursuing what I am truly interested in and hope to make a difference in this research field. I am grateful for the support of all technicians and partners who have offered me a hand during experiments, and I acknowledge the financial support from the Hong Kong Polytechnic University.

Table of Contents

List of Tables

List of Figures

List of Abbreviations

Internet of things	IoT
polymer poly(dimethylsiloxane)	PDMS
Polyvinyl alcohol	PVA
integrated circuits	ICs
silicon	Si
Liquid Metal	LM
Eutectic Gallium-Indium alloy	EGaIn
poly(styrene-*block*-butadiene-*block*-styrene)	SBS
electrocardiography	ECG
ultraviolet	UV
atomic force microscope	AFM
permeable liquid-metal-based microelectrodes	Plms
dimethylsulfoxide	DMSO
Permeable stretchable LM-based microelectrodes	Plm
LM-based hydrogel microelectrodes	PlmH
Electrocorticography	ECoG
Three-dimensional	3D
Wireless permeable 3D integrated electronic skin	WPE-skin
Near-field communication	NFC

Chapter 1: Introduction

1.1 Background

The pursuit of information, technology, and energy has always been a driving force behind human development. Recent advancements in the Internet of Things (IoT) and artificial intelligence have ushered in a new era where electronics and machines offer unparalleled convenience[1,2]. This has led to a demand for a new generation of electronics that are flexible, foldable, twistable, and stretchable to meet various application needs, including wearable and epidermal electronics, robotics, touch displays, stretchable circuits, antennas, sensors, and actuators.

However, in addition to electronic performance, physiological comfort is also crucial for long-term wearability. Sweat is constantly secreted from sweat glands and evaporates to the outer environment[3–5] at a rate of about 200-600 g m^{-2} day^{-1}. Most stretchable electronics are currently fabricated on compact impermeable polymeric thin films, which can hinder moisture evaporation and cause skin allergies or inflammation[6,7]. Hence, developing wearable electronics and e-skins with good permeability is paramount.

Permeable and stretchable electrodes are vital components of permeable stretchable electronics. They require outstanding permeability, stretchability, conductivity, and electrical stability to enable efficient operation of bio-integrated electronics[8]. However, these deformable electronics are usually unstable under strain and can suffer from mechanical fracture and dramatically reduced conductance, leading to signal transfer issues, power consumption problems, and noise enhancement. Therefore, conductors should be both mechanically and electrically stable to ensure reliable performance.

Fabrication and system-level integration of permeable stretchable electronics are technically challenging due to the need for complex, high-density, multilayered functional devices and circuits[9,10]. Patterning techniques play a crucial role in this process. However, current technologies lack the ability to incorporate permeable stretchable materials into mass-producible devices. Therefore, it is highly important to develop high-performance permeable stretchable electronic devices and systems with high resolution, multifunctionality, and outstanding wearing/implanting comfort.

1.2 Research Objectives

In light of the potentials and challenges in permeable stretchable electrodes, this project aims at fabricating ideal permeable stretchable electrodes in a scalable way More specifically, this project focus on several following objectives:

1. To develop a suitable patterning technique for permeable and stretchable liquid-metal-based electrodes with high resolution and high throughput.

2. To fabricate targeted permeable and superelastic substrates for the transfer of the electrodes. The stretchable substrates should be permeable to permeate gas, water moisture, and liquid for improving physiological comfort during long-term wearing.

3. To explore the properties of the patterned liquid metal electrodes in terms of patterning features, stretchability, conductivity, electrical stability, permeability, and biocompatibility.

4 To integrate the permeable stretchable circuits with high-performance electronic components on a system-level by developing stretchable and reliable electrical interfaces between soft circuits and rigid components.

1.3 Research Originality

Permeable stretchable bioelectronics offer unique advantages for long-term bio-integrated electronic applications. However, the key component, the electrodes, must meet high standards of electrical and mechanical performance while also being permeable to air, moisture, and liquid for optimal comfort and biosensing capability. Unfortunately, current permeable stretchable electrodes lack a suitable patterning technique with high resolution and throughput, presenting a significant obstacle to their mass production. In addition, current permeable stretchable bioelectronics are lacking a complex system-level integration due to the low-integration-density and unstable electrical interfaces with rigid components.

This research aims to address these challenges by proposing rational strategies for high-density fabrications and integrations of permeable stretchable bioelectronics using liquid metal. By doing so, we hope to overcome the trade-off dilemma between stretchability and conductivity while also providing insights into material design, device fabrication, and system-level integration for desirable permeable stretchable electrodes, devices, and systems. Ultimately, this research has the potential to enable scalable and high-density production of permeable stretchable bioelectronics, representing a significant step forward in this field.

1.4 Outline of the Report

The report is organized as follows:

Chapter 1 gives a brief introduction about the general background of the research project topic and the challenges. The research objectives as well as the significance and values are also included.

Chapter 2 illustrates the rationale of permeable stretchable bioelectronics and reviews the historical development and recent progress of stretchable conductors and electronics, and the research gaps in the fabrication of permeable stretchable bioelectronics with high resolution and density.

Chapter 3 introduces the experimental methodology in detail, including materials, fabrication processes, and instruments, as well as the characterization procedures.

Chapter 4, 5, 6, and 7 present the outcomes and has a rational discussion about the results.

Chapter 8 concludes the research results and proposes the outlook, limitations, and future work plan.

Chapter 2: Literature Review

2.1 Introduction of Permeable Stretchable Bioelectronics

Traditional electronics are integrated on rigid silicon wafers which cannot suit the soft and curved surface of biology and other items. The first try in stretchable conductors is the all-polymer field-effect transistor by printing technique[11]. Since then, material science in organic semiconductors and new printing technologies have been emerging[12–15]. To meet the market demand and future anticipation, scientists are committed to developing more compelling and technically challenging stretchable electronics. These electronics can not only be bent but twisted, compressed, and stretched. In general. There are two methods to fabricate such electronics: one is by structural design and transformation to confer stretchability, and the other is to fabricate intrinsically stretchable electronics by modifying the conductivity and electrical stability of the stretchable polymers[16]. The latter one consists of stretchable conductive composite fabrication and conjugated polymer engineering (or introducing additive in the conjugated polymer). However, under daily activities, the skin will secrete sweat sensibly or insensibly, making the skin wet, while existing dense film-based flexible electronics may induce the accumulation of sweat in the skin surface due to the poor permeability and further resulting uncomfortable sensation ever skin allergies or inflammation[6,7].

Stretchable electronics with porous structures, in terms of permeable electronics or breathable electronics, which could allow the transport of gas, moisture vapor, and water, have been reported in recent years[8].

In consequence, the permeability to gas, moisture, and liquid is highly important for the fabrication of on-skin electronics. Textiles and porous-thin films have been developed as the substrate of permeable electronics since the porous geometry, while the

permeability of these materials is mainly affected by porosity, thickness, as well as materials' properties. Therefore, promising strategies to fabricate permeable electronics are to engineer the porous structure and thickness of electronics substrates to enable permeability to the air, moisture, and liquid.

The ability of moisture vapor permeability, which is defined previously as the amount of moisture vapor penetrated through the materials since a certain period, is reflected in terms of water vapor transmission rate (WVTR)[8]. ASTM E96E is the often-used standard for measuring the WVTR, where the moisture vapor permeability can be measured by covering the materials at the top of a lidless water container and weighting the water loss per hour (or per day) per square meter (g/h m^2 or g/d m^2). To ensure a healthy thermal and moisture exchange microenvironment, the value of moisture vapor permeability is commended better than 200 g/d m^2 for wearable and on-skin electronics. Air permeability can be measured by measuring the air velocity that passes through materials with a certain area and at a specified differential air pressure between the top and bottom surface of the material and is denoted as $cm^3\ s^{-1}\ cm^{-2}$ (or $m\ s^{-1}\ cm^{-2}$). Both water vapor transmission rate and air permeability can be directly used for the assessment and comparison of the "breathability" of different kinds of permeable electronics. Higher the values of water vapor transmission rate and air permeability, the better permeability the materials have.

Substrates for permeable stretchable electronics mainly include fibrous textiles (fibers/yarns/fabrics) and porous, thin films. To render such substrates electrically conductive, stretchable conducting materials are introduced via either intrinsically stretchable materials or structural engineering of non-stretchable materials (extrinsically stretchable).

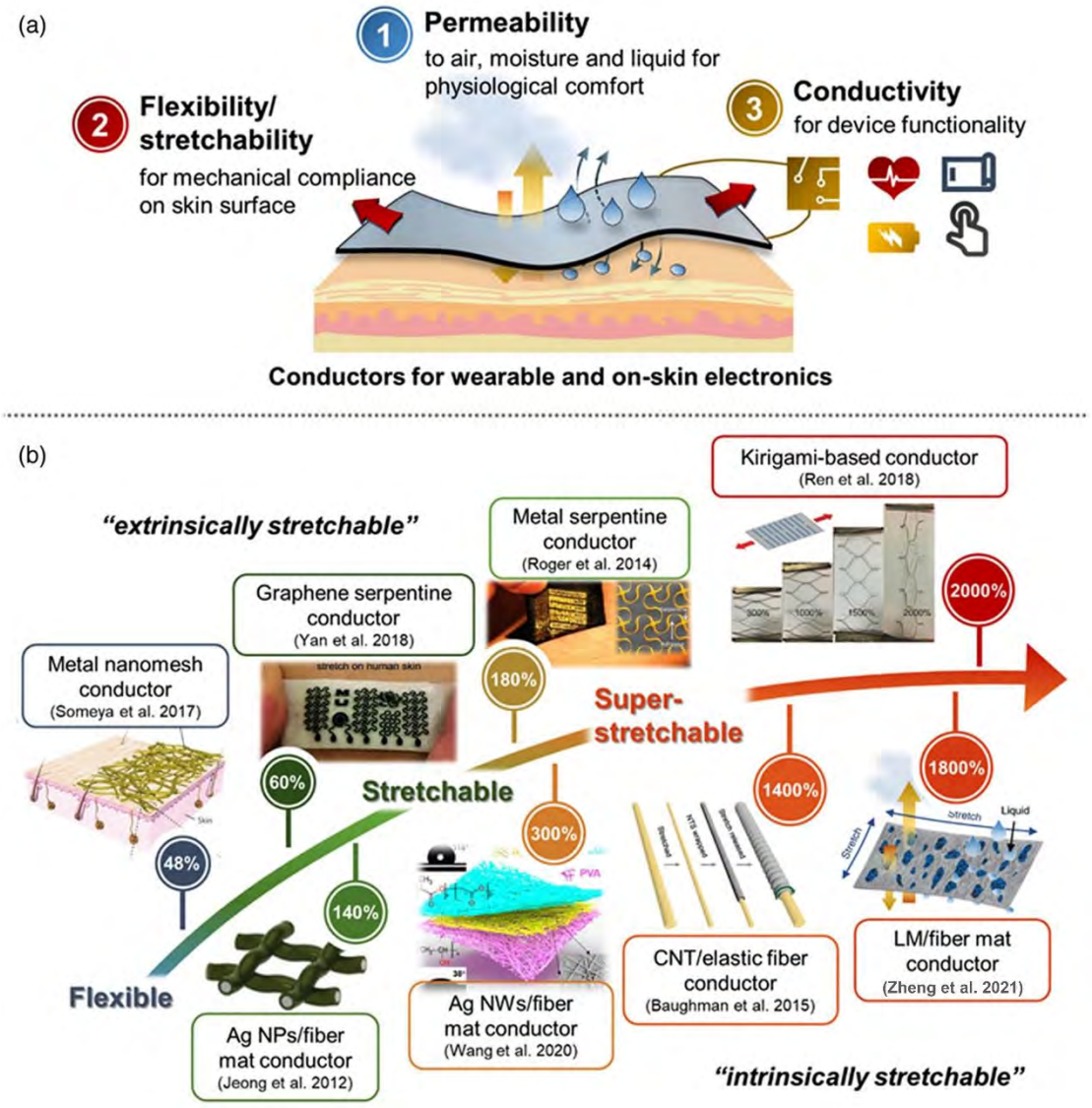

Figure 2.1 Current permeable stretchable electrodes including extrinsically stretchable ones and intrinsically stretchable ones[8].

Structurally, any material, stiff or soft, is bendable and can bear a certain extent of strains when it is ultrathin. For instance, silicon nanoribbon (100nm thickness) can stand about 0.0005% strain[16]. Other strategies have been reported including the wavy configuration of silicon membrane and integration with elastomer substrate (10%~20% strain)[17,18], noncoplanar serpentine (0.15%~140%)[19], coiled spring (<=2%)[20], mesh layout designs (0.01%~57%)[21]. The polymer poly(dimethylsiloxane) (PDMS) is usually used as the elastic substrate, and the rigid electrical element material is still the

conventional silicon. This structurally stretchable building method is limited by the complicated and laboring configuration process involving Cr/SiO_2 deposition and technically challenging transfer printing method. Furthermore, stretchable electronics via structural engineering can only bear really low strain (<2%), which is of marginal importance in practical application.

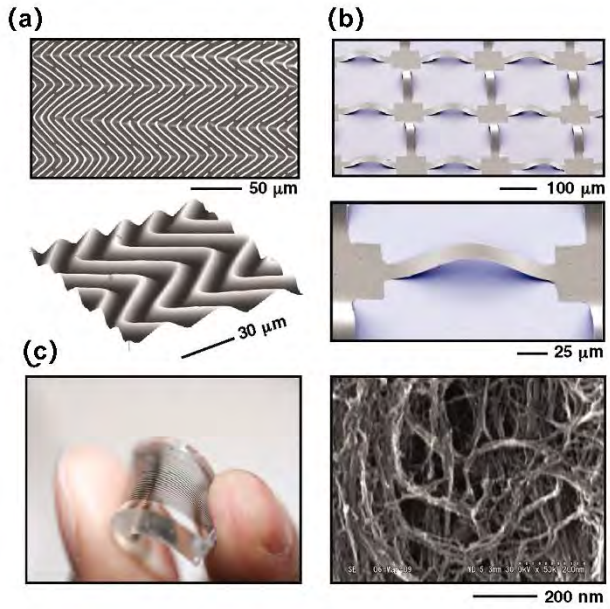

Figure 2.2 Structurally stretchable electronic materials including (a) Stretchable silicon membrane (~100-nm thickness) configured in a wavy shape and bonded to a piece of rubber, and (b) Stretchable silicon membrane (~100-nm thickness) patterned into a mesh geometry and bonded to a rubber substrate, (c) Printed conductive lines of printed carbon nanotubes gel on the PDMS[16].

Intrinsically, stretchable conducting materials mainly include stretchable conductive composites. For stretchable conductive composite, the conductivity is determined by the conductive pathway formed in the elastic substrate. Many elastic substrates were reported for the fabrication of conductive composites. Elastomer substrates serve as the stretchability contributor, which is significant for the mechanical stability of the percolation network of the conductive composite. Some parameters are decisive in fabricating stretchable conductive composite including elastic modulus, chemical

structure, and chemical affinity to conductive fillers. Compared with chemically and irreversible chemically crosslinked polymers (PDMS and Ecoflex) by covalent bonds between polymer chains, physically crosslinked force is more moderate[22,23], which could be beneficial for conductive filler regulation and shape variation.

In terms of inherent stretchability, SBS and SEBS with the highest Young's modulus are the best candidates to withstand the external stress and would not be easily broken. Besides, with proper structure design, the stretchability can be enhanced. For example, hydrogels (Young's modulus of 29 kPa) with ionic and irreversible chemical crosslinking, of which the maximum strain could be improved by 19 times (2300%)[24].

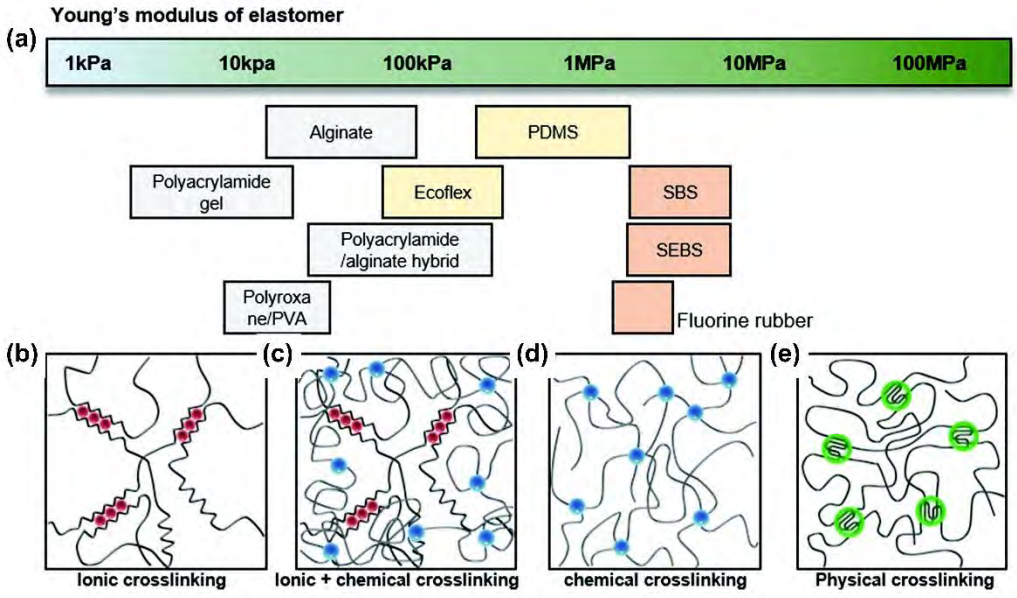

Figure 2.3 Chart for various types of elastomers and their crosslinking methods[1]. (a) Young's moduli of various elastomeric matrices. The modulus can vary depending on the fraction of polymer component, type of crosslinker, and curing temperature. The moduli of nanocomposites increase as nanomaterials are embedded in pure elastomer substrates (b) physical hydrogels crosslinked by ion–polymer complexation. (c) A hybrid of physically crosslinked and chemically crosslinked hydrogels, (d) chemically crosslinked elastomer, and (e) physically crosslinked elastomer.

Since most polymers are nonconducting and cannot be directly used as conductors, conductive fillers are the major contributor of stretchable conductive composites. According to the rationale above, the percolation threshold, morphology, size, and distance matter a lot in electron transportation efficiency. Based on the theoretical deduction and experiment verification, conductive fillers with a high aspect ratio (nanowires, nanorods) tend to form a better percolation conductive network because, in a certain polymer matrix, higher-aspect-ratio fillers can form a conductive pathway with fewer junctions and thus lower junction resistance. Moreover, the selected conductive fillers should possess high conductivity. In light of this, several materials have been chosen as the proper candidates, including carbon materials, noble metals, and some conducting polymers.

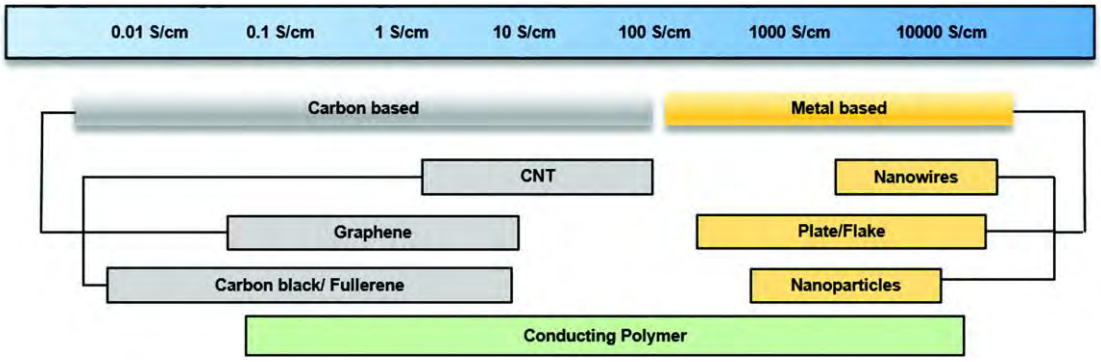

Figure 2.4 Conductivity flow chart for various types of conductive fillers based on carbon- and metal-based materials and conducting polymers[1].

2.2 Liquid Metal (LM)

2.2.1 Advantages of LM for Permeable Stretchable Bioelectronics

LM is a type of liquid-state conductive material with high stretchability (infinite) and conductivity (> 10^4 S/cm). Recent studies have revealed that gallium (Ga) metal based LMs, including EGaIn (Ga alloyed with Indium (In)), and Galinstan (Ga alloyed with

In and Tin (Sn)), have the advantages in low toxicity, high electrical conductivity (~34,000 S/cm), and high thermal conductivity (Figure 2.5)[25,26]. They have been investigated as promising conducting materials for stretchable interconnects, antennas, soft robotics, and bioelectronics.

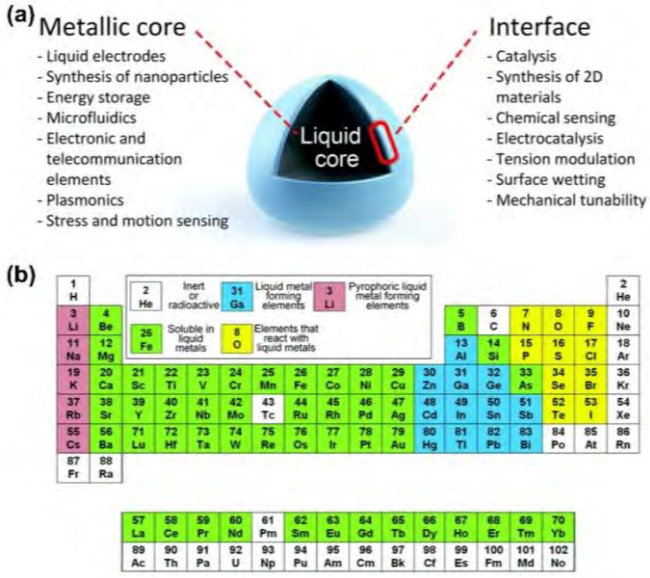

Figure 2.5 (a) Schematic of a liquid metal droplet showing applications of liquid metals that take advantage of the liquid core or the interfacial region near and at the surface. (b) Liquid metal base elements, in blue, and other elements that take part in forming alloys and compounds in other colors, depending on their roles[26].

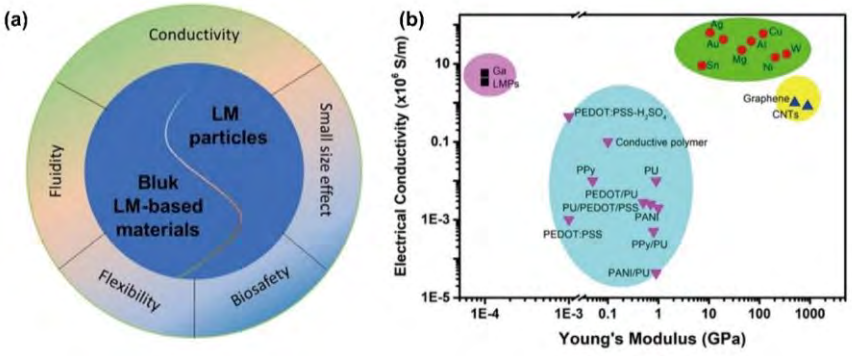

Figure 2.6 Advantages of LM in permeable stretchable electronics including (a) The properties of liquid metal materials[25]. (b) Comparison of electrical conductivity and Young's modulus of

conductive materials. Each background area indicates a set of materials as follows: Ga-based LM (purple), traditional metals (green), carbon material (yellow), and conductive polymer (blue).

Compared with other reported stretchable electronics materials, LM-based stretchable conductors can provide promising stretchability, conductivity, electrical stability, and most importantly, maintain biocompatibility and permeability with porous/fibrous substrates. Notably, Ga and In possesses outstanding biocompatibility without showing obvious toxicity under the present test conditions. However, the toxicity is always dose-related, so that the mass loading of LM should be under control for implantation.

Table 1 Summary of electrical and mechanical properties of permeable stretchable conductors.

Materials	Conductivity ($S\ cm^{-1}$)	Max. Stretchability	Durability	Change of resistance under stretching	Permeability ($g\ m^{-2}\ day^{-1}$)	Ref.
LM-Ag-SBS	12,346	2,500%	1,000 cycles (1,000%)	2.5 (2,500% strain)	695	[27]
Au/PVA mat	18868	48%	10,000 cycles (25 %)	100% (25% strain)	809	[7]
Au nanofilm	N.A.	35%	1000 cycles (20%)	140% (34% strain)	N.A.	[28]
LM/SBS mat	18,000	1,800%	100 cycles (1800%)	4.1% (1,800% strain)	724	[6]
Ag nanoparticles/SBS mat	5,400	140%	300 cycles (140%)	59% (100% strain)	N.A.	[29]
AgNW/PU	125.4	4000%	1,000 cycles (50%)	~100 (400% strain)	N.A.	[30]
LM micromesh	~55.6	400%	1000 cycles (100%)	11 (400% Strain)	384	[31]
Graphene/silicone elastomer sponge	45.6	1,000%	1,000 cycles (500%)	6% (1,000% strain)	~900	[32]
Au/Ti/PI kirigami film	N.A.	95%	2000 cycles (30%)	1.3 (40% strain)	480	[33]
AgNW-SEBS	22,300	62%	1000 cycles (100%)	1.5 (15% strain)	580	[34]

LM liquid metal, **SBS** poly(styrene-butadiene-styrene), **PVA** polyvinyl alcohol, **AgNW** silver nanowire, **PU** polyurethane, **PI** polyimide, **SEBS** styrene ethylene butylene styrene,

2.2.2 Compositing LM for Stretchable Bioelectronics

Owning superior properties like high conductivity, stretchability, and biocompatibility, LM is a promising candidate for permeable stretchable electronics. However, the high surface tension of LM (e.g., 718 mN/m for galinstan), LM is difficult to wet and spread on the surface of a substrate[27]. When printed onto polymeric substrates of stretchable devices or mixed with a polymer matrix, LM dewets from the polymer surface and forms separated microdroplets that significantly hinder the electrical pathway. The rapid formation of an insulating oxide layer on the surface of the microdroplets, once exposed to the air, further decreases the conductivity. researchers have proposed strategies using LM. To harness the rheological properties of LM, two strategies were proposed. One is to composite LM into elastic substrates for stretchable conductive composite, the other is to pattern LM onto the substrates. For compositing LM into elastic substrates, microchannel fabrication and the encapsulation of LM particles were two methods[20,35–39].

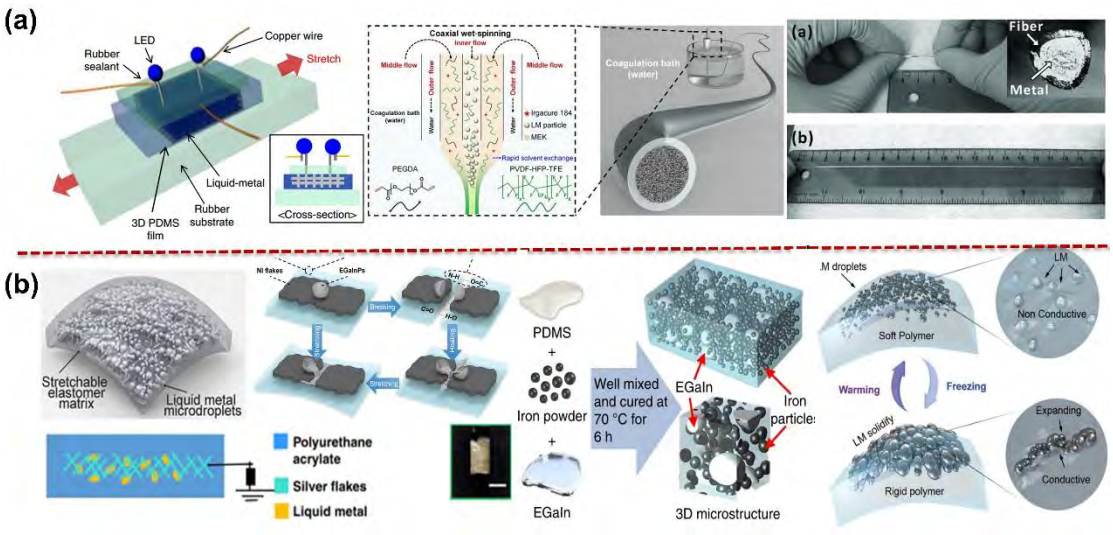

Figure 2.7 Strategies for compositing LM into stretchable electronics including (a) microchannel fabrication and (b) encapsulation LM particles into the elastic substrates[20,35–39].

In the past decade, several strategies have been developed to enhance the wettability of LM. One common strategy is to encapsulate LM microdroplets with surfactant polymers, which enables good air stability and wettability of LM[40]. Nevertheless, the encapsulation approach unavoidably creates less-conductive junctions among the LM particles, and hence seriously decreases the conductivity of the conductor, typically by orders of magnitude. Another method is to modify the substrate with a thin layer of metal that can wet LM[27].

2.2.3 Patterning LM for Stretchable Bioelectronics

Patterning LM onto the elastic substrates is another strategy for fabricating LM-based stretchable electronics[41]. To tackle the high surface tension of LM, two methods were proposed consisting of assistance of the oxide skin (mainly Ga_2O_3), surface modification (introducing of functional group, thin metal layer for alloying, etc.).

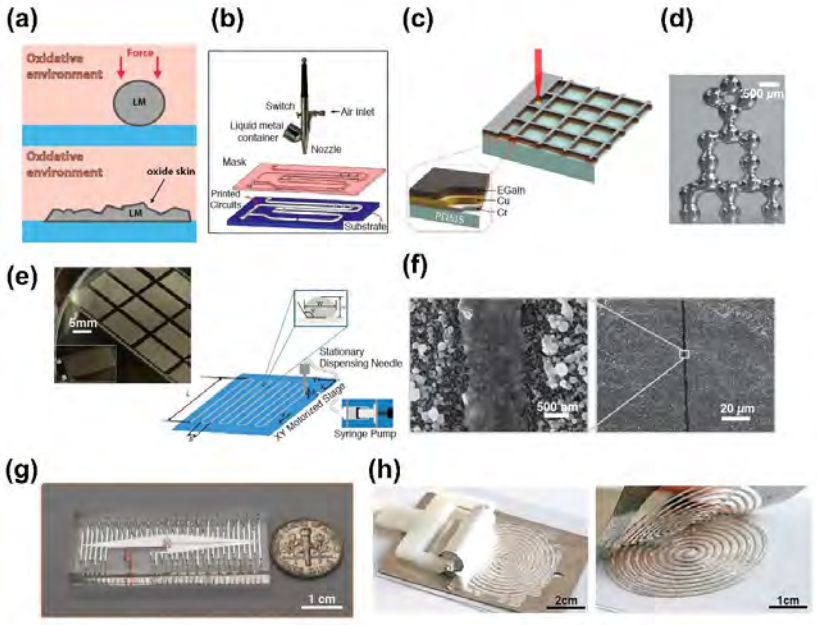

Figure 2.8 Patterning methods rely on stabilization by the oxide skin[41]. (a) Schematic of the patterning principle. LM is shaped into a specific form through mechanical force in an oxidative environment, and its stability is ensured by the formation of a new oxide skin.. (b) Atomized

spraying. (c) Laser machining. (d) 3D printing. Reproduced with permission from ref (33). (e) Direct writing. (f) Sintering of nanosized LM particles. (g) Injection in microfluidic channels. (h) Rolling through a stencil mask.

By taking advantage of the difference between LM-lyophobic and LM-lyophilic surface, selective wetting of LM was achieved, that is, LM could selectively wet on the lyophilic region while not wet on the lyophobic area.

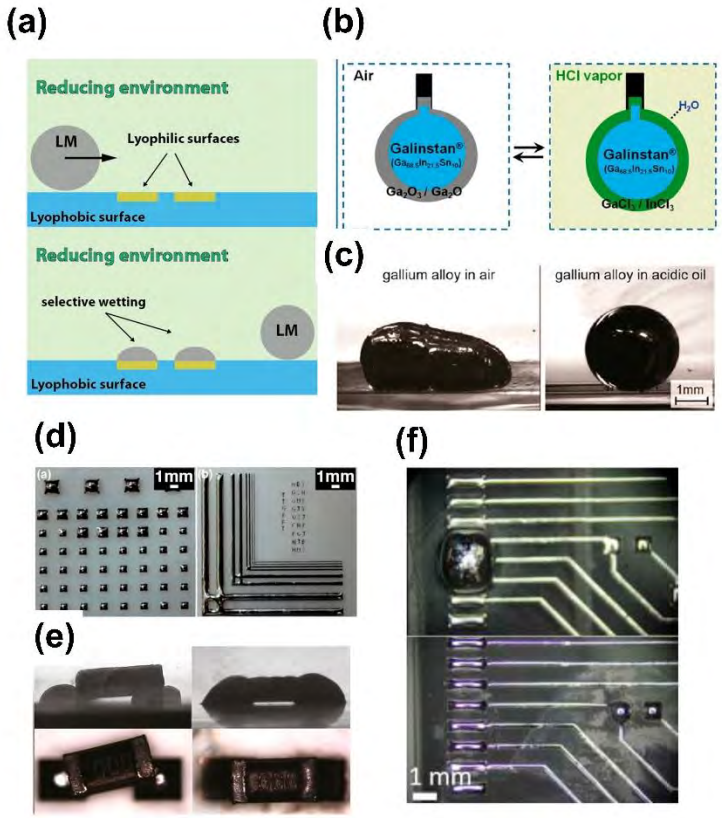

Figure 2.9 Patterning methods relying on selective wetting in reducing environment[41]. (a) Schematic representation of how LM selectively wets a lyophilic substrate in a reducing environment. (b) Schematic diagram of the chemical reaction between Ga oxides consisting of Ga_2O_3 and Ga_2O and HCl vapor. (c) Effect of acidified siloxane oil on LM. (d) Various LM patterns from selective wetting of Au/Cr thin film in HCl reducing environment. (e) Digital images showing the self-alignment of a component with LM patterns for surface mounting before and after HCl vapor treatment and (f) images showing a circuit with and without LM bridging during the

deposition step.

In summary, LM could be patterned onto the elastic surface utilizing various techniques[42] including imprinting, 3D printed stacking, injection and freeze casting, microcontact printing, selective wetting, direct laser patterning, stencil lithography, and suspension 3D printing.

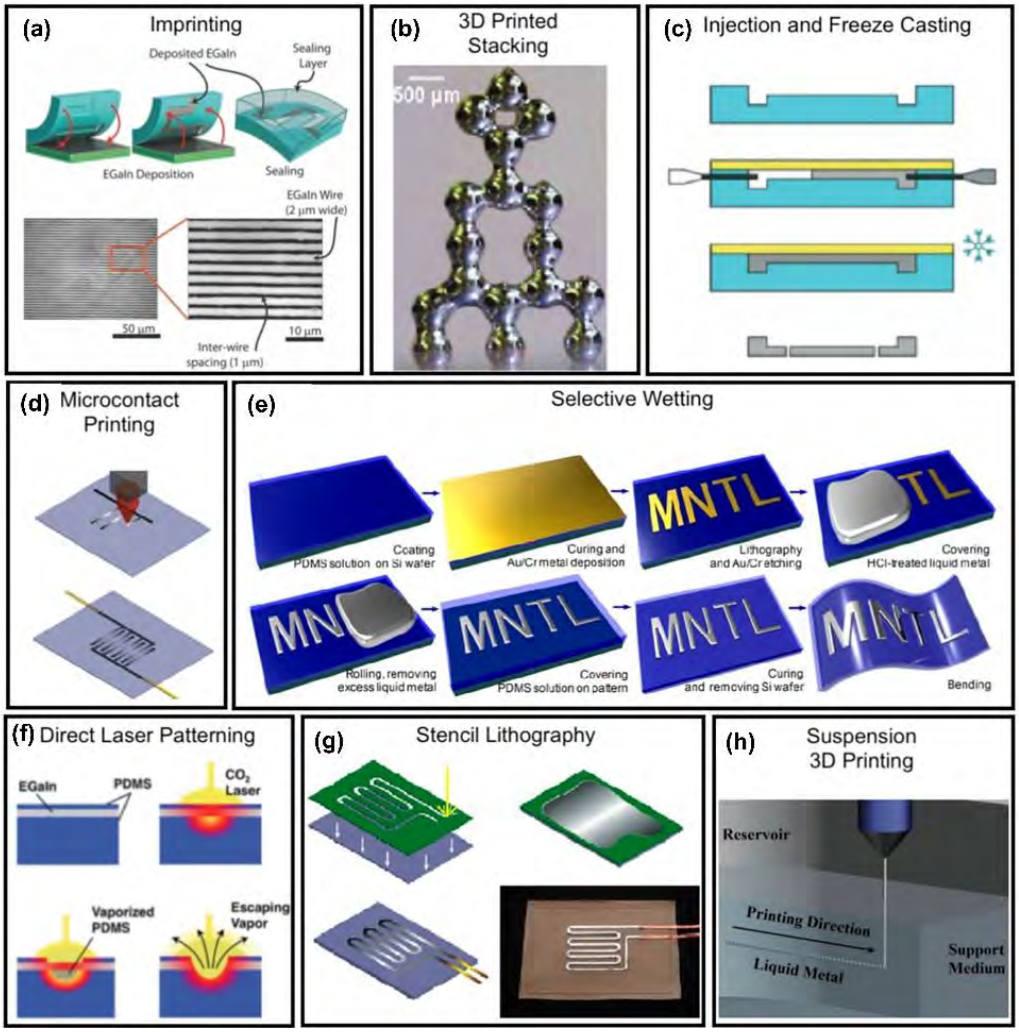

Figure 2.10 Methods to pattern liquid metal including various techniques including imprinting, 3D printed stacking, injection and freeze casting, microcontact printing, selective wetting, direct laser patterning, stencil lithography, and suspension 3D printing[42].

2.3 Fabrications for Permeable Stretchable Bioelectronics

2.3.1 Challenges in Fabricating Permeable Stretchable Bioelectronics

Traditional silicon (Si) integrated circuits (ICs) have been showing unparalleled performance in terms of low power consumption, high performance, and reliability compared with organic electronics[43]. Si is mature and well compatible with the current fabrication technologies of electronics. However, the form factor of rigid Si limits its utilization in flexible and stretchable electronics. Therefore, thinned Si IC technology was developed for flexible electronics by grinding, reaction, wet or dry etching to selectively remove Si. For instance, an ultrathin Si wafer with a thickness of ~ 25 μm could achieve a bending radius of 5 mm. In addition, Si wafers in the shapes of nanoscale ribbons, wires, or membranes are flexible. Nevertheless, thinned Si wafers are extremely fragile, which can be easily damaged by external heat and conventional assembly equipment, limiting the scalable production of Si-based stretchable and flexible electronics.

Performance parameters	Printed electronics	Silicon ICs
Charge carrier mobility ($cm^2 V^{-1} s^{-1}$)	~ 1 (organics)	~ 1000
Switching speed (MHz)	~ 1	~ 5000
Operating voltage (V)	~ 10	~ 1
Lifetime (yr)	~ 0.1	~ 10
Substrate softness – elastic modulus^{-1} (GPa^{-1})	~ 2.5^{-1} (plastics)	~ 180^{-1}
Large-area scalability (m^2)	~ 100	-
Printing speed (ms^{-1})	~ 1	-

Figure 2.11 Performance comparison and utilization of printed electronics and silicon ICs in FHE systems in terms of charge-carrier mobility, switching speed, operating voltage, lifetime, substrate softness, large-area scalability, and printing speed comparison between the two technologies. The data are color-coded in light blue (desirable) and red (not desirable) to show the complementary nature of printed electronics and silicon ICs[43].

Instead of simply using Si-based inorganic materials, structural engineering of organic materials and rigid inorganic devices is an effective strategy for fabricating hybrid electronics with circuit-level stretchability. Due to constraints in mechanical and configurational design, mostly with stiff active component island and fractal interconnect bridge, the fabrications are usually sophisticated, and the surface density of functional components within an array in a single layer will reach a bottleneck[44–47].

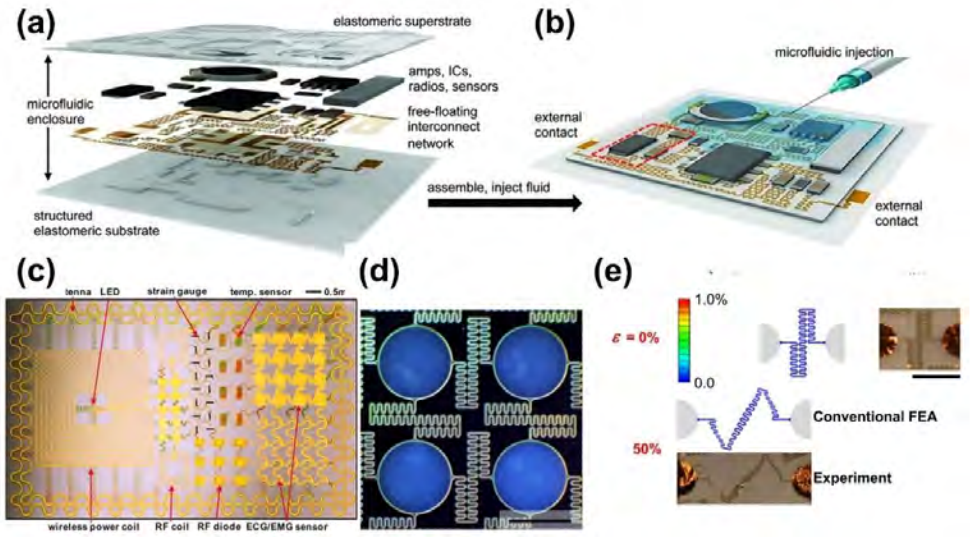

Figure 2.12 (a) Schematic illustrations of key components in a soft, stretchable electronic system that integrates strain-isolated device components and a free-floating interconnect network in a thin elastomeric microfluidic enclosure and (b) the system after assembly[44]. (c) Image of a demonstration platform for multifunctional electronics with physical properties matched to the epidermis[47]. Mounting this device on a sacrificial, water-soluble film of Polyvinyl alcohol (PVA), placing the entire structure against the skin, with electronics facing down, and then dissolving the PVA leaves the device conformally attached to the skin through van der Waals forces alone, in a format that imposes negligible mass or mechanical loading effects on the skin. (d) Optical images of electrode pads and fractal inspired interconnect on a silicon wafer (top panel; top-down view; ~4-unit cells), and (b) optical images and corresponding finite element analyses of symmetric deformation modes at 0% strain and 50% strain[45,46].

Further, when adopting structural engineering, localized stress and mechanical mismatch are usually generated not only at the island/bridge interface but the device/biology interface[48]. For one thing, the localized stress at the island/bridge interface can lead to mechanical failure and poor reliability of stretchable electronic devices, for another thing, the mechanical mismatch between soft organs and hard devices causes discomfort and unsatisfying wearability of bio-integrated electronics.

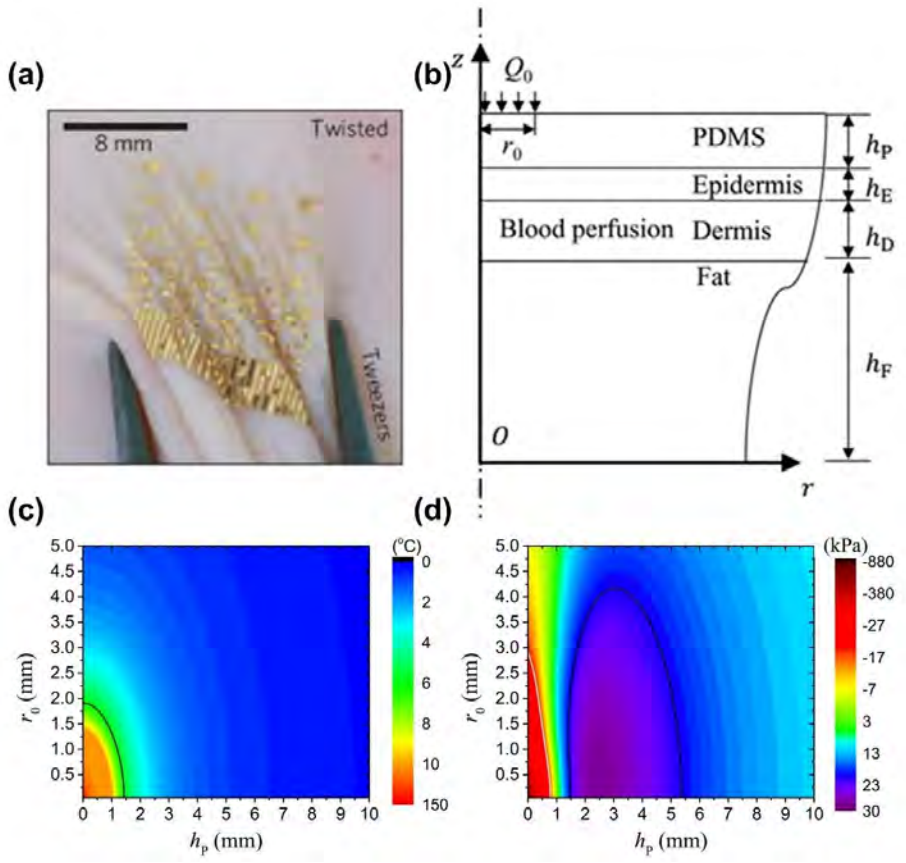

Figure 2.13 (a) An EED consisting of temperature sensors and heaters on a skin in a twisting motion and (b) schematic diagram of the cross-sectional structure for the EED/skin system. (c) The maximum temperature increases and (d) the maximum principle stress σ_{max} at the EED/skin interface varies with the size of the heating component and the substrate thickness[48].

Considering the higher mechanical deformability and robustness, improved skin compatibility, intrinsically stretchable polymer materials could be a rational selection instead. However, the production of intrinsically stretchable materials and devices is

still in its infancy. The main limitation for the high-resolution and mass production of intrinsically stretchable electronics is the lack of scalable micro/nanopatterning methods for intrinsically stretchable and soft materials.

This challenge mainly originates from two aspects. Firstly, unlike inorganic materials, polymeric materials lack chemical orthogonality with photoresists and developers used in traditional patterning techniques such as photolithography, electron beam lithography (EBL), and nanoimprint lithography. These polymeric materials degrade, swell, or dissolve during processing with nonorthogonal solvents, thus showing an adverse effect on the performance[49]. Particularly, orthogonality is critical in printing devices with multi-layer structure[50]. In this way, orthogonal solvents should be carefully selected for the individual layers, in which the solvent used in one deposition does not dissolve any previous layer. However, it's usually challenging[51,52].

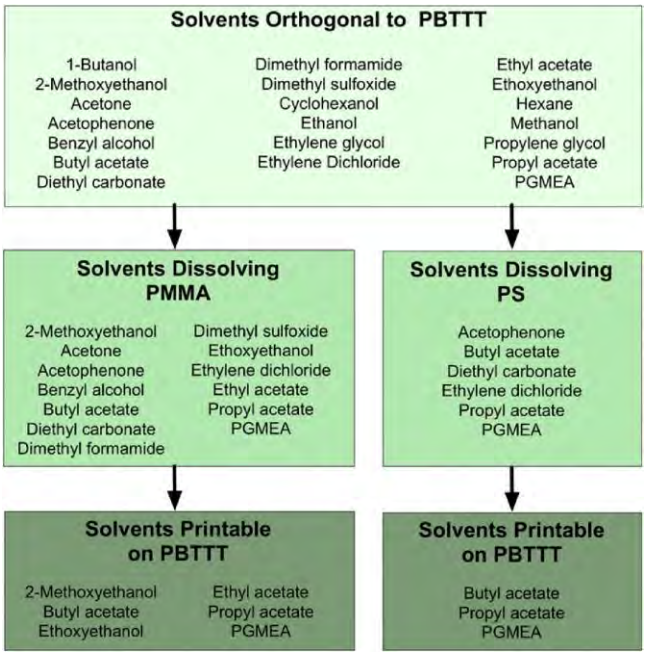

Figure 2.14 Schematic summarizing the solvents orthogonal to organic semiconductor (Poly(2,5-bis(3-hexadecylthiophen-2-yl)thieno[3,2-b]thiophene (PBTTT), the solubility of polymer dielectrics (Poly(methyl methacrylate) (PMMA), and Polystyrene (PS). in the orthogonal solvents, and their printability on PBTTT[52].

The second concern is the low thermal budget of the polymeric materials[43]. Due to low glass transition temperature (Tg), polymers used for stretchable electronics cannot sustain high-temperature processes such as soldering and thin-film deposition like thermal evaporation, E-beam deposition, and atomic layer deposition.

Moreover, permeable stretchable substrates are known to be polymeric, porous, and rough, which is even more challenging to be pattern than compact and flat polymer thin films[20]. The porous and rough structure largely hinders the patterning features, intact electrical interconnects, and normal functions of stretchable and soft electronics. Therefore, it's challenging but indispensable to manufacture intrinsically stretchable and soft materials on permeable substrates for enhancing the wearing coziness and physical health during long-term applications.

2.3.2 Current Patterning Techniques for Permeable Stretchable Bioelectronics

There are two routes to introduce conductivity for permeable substrates, that is, surface coating/patterning or fabrication of conductive material-substrate composites. Briefly, patterning methods for permeable stretchable electronics were reported including inkjet printing[53–55], screen/stencil printing[6,56–58], spray coating with mask[59,60], pen-writing[61–64], physical vapor deposition (PVD) with mask[7,65], textile method[66,67], and laser engraving and cutting[32,68,69].

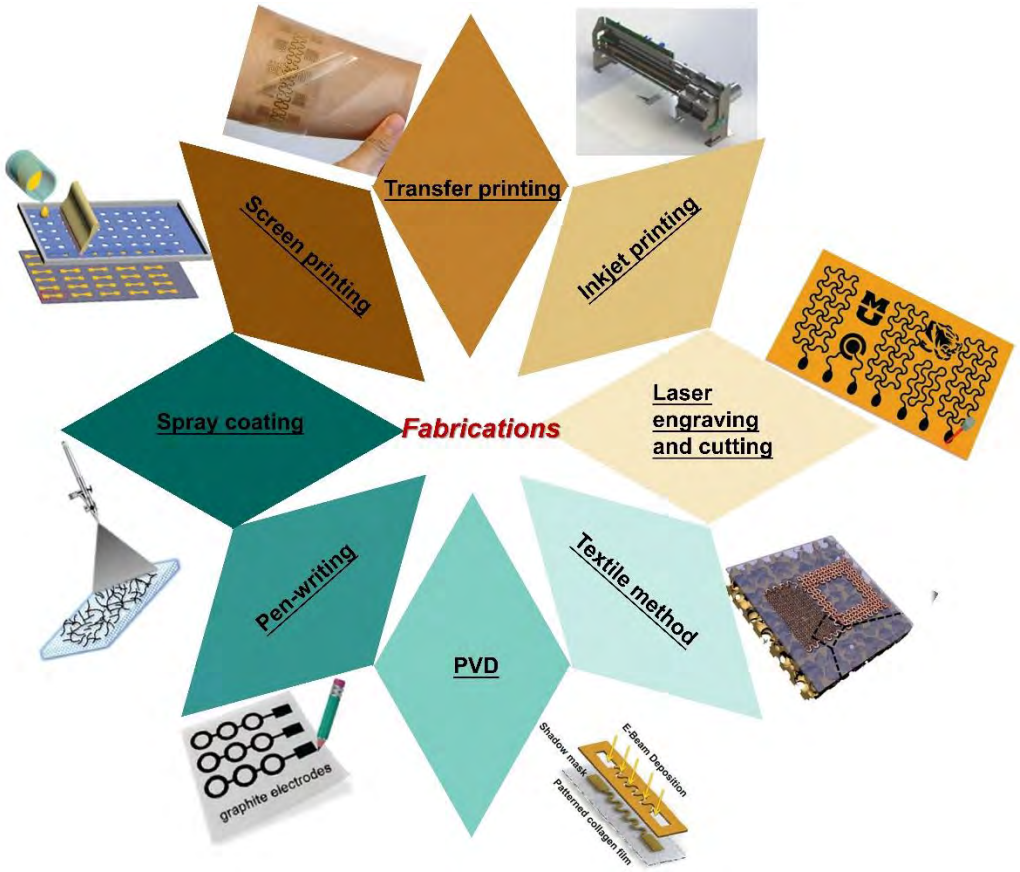

Figure 2.15 The state-of-the-art fabrications of permeable stretchable electronics.

Transfer printing is a typical technique combining the advantages of mature IC technology and versatile substrate selection. Generally, the transfer printing process consists of two steps including retrieval/pick-up of inks from the donor substrate and printing/delivery of inks onto the receiver substrate. Firstly, At the beginning of the retrieval process, the stamp is brought into contact with the ordered and releasable inks on the donor substrate. The retrieval process can either selectively manipulate specific inks or non-selectively and parallelly for high throughput. The working principle involves a three-layer (stamp/ink/substrate) system with two interfaces (stamp/ink and ink/substrate)[70]. To enable a successful transfer printing, the adhesion of the stamp/ink interface should be stronger than the ink/substrate interface during retrieval while be weaker when printing. Due to the independence of external stimuli at the ink/substrate interface mostly, this adhesion strength is regarded as a constant (red solid line). While

the adhesion strength at the stamp/ink interface could be modulated by stimuli like lateral movement and peel velocity (black solid line).

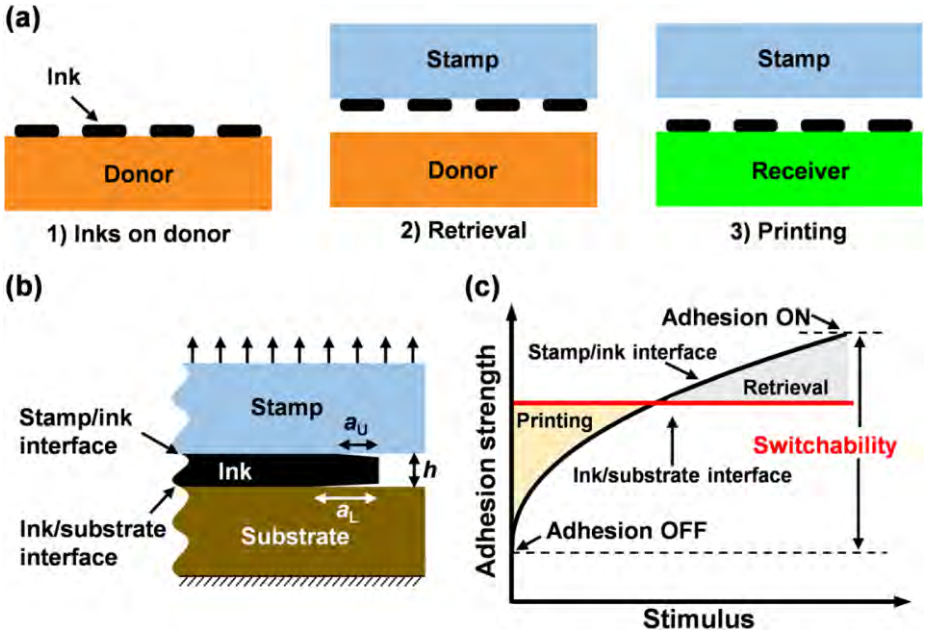

Figure 2.16 Operating process and principles of transfer printing. an Illustration of the transfer printing process. (1) Inks are prepared on the donor substrate in a releasable manner. (2) Retrieval process: an elastomer stamp is used to retrieve the inks. (3) Printing process: inks are printed onto the receiver substrate. The two interfaces in the stamp/ink/substrate structure. The strength of adhesion can be modulated by an external stimulus, which results in a switchable adhesive state between high (ON) and low (OFF) adhesion[70].

Strategies for modulating the adhesion strength at the stamp/ink interface were proposed including surface chemistry, kinetically control, laser-driving, gecko-inspired structure, and aphid-like structure[32,68,69,71,72].

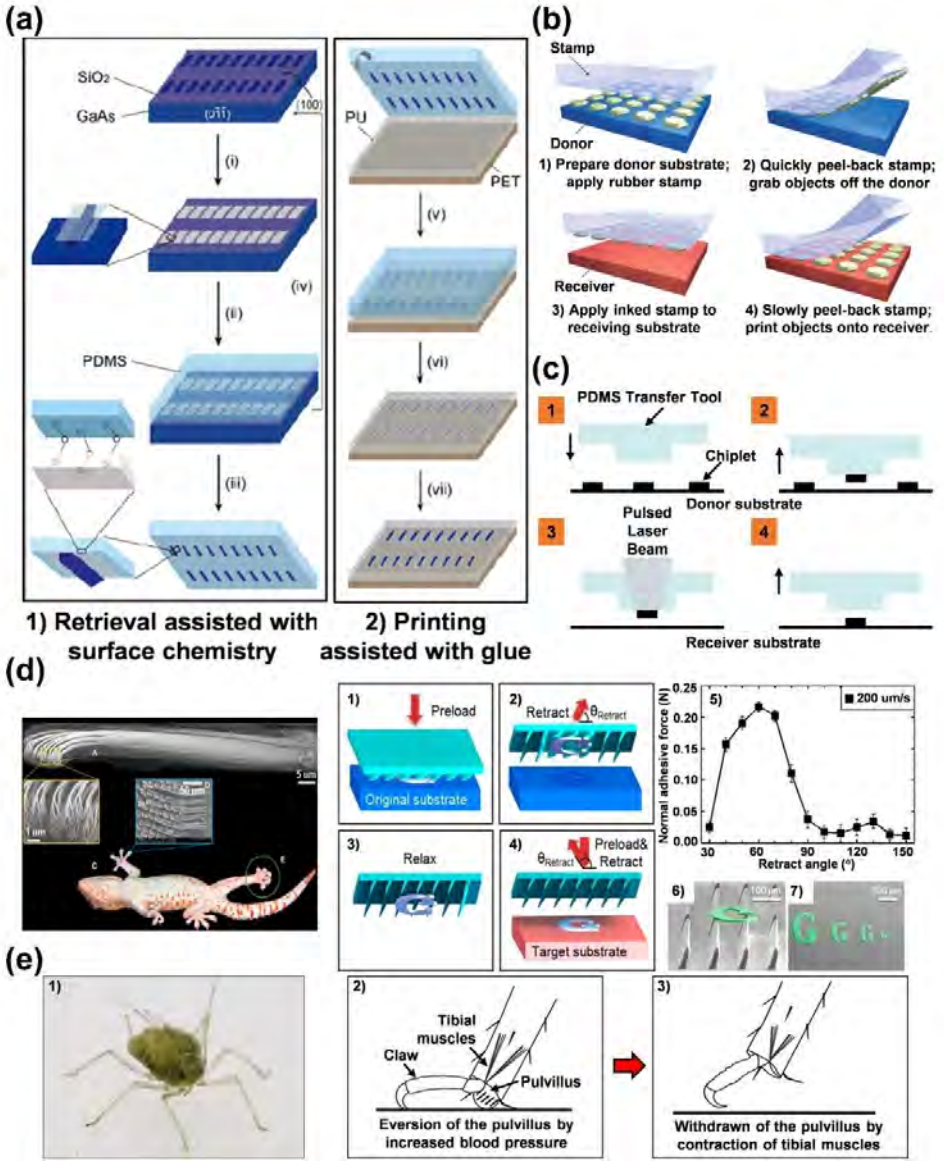

Figure 2.17 Strategies for modulating the adhesion strength at the stamp/ink interface were proposed including (a) surface chemistry, (b) kinetically control, (c) laser-driving, (d) gecko-inspired structure, and (e) aphid-like structure[32,68,69,71,72].

Screen/stencil printing is a scalable and low-cost printing technology that brushed functional inks with the designed screen or stencil. Stretchable conductive tracks can be printed with inks such as Ag/AgCl, metallic and carbon-based inks[73]. Factors such as viscosity of the ink, weight percentage of the solid content, and the filler size show influence on the printability of the inks.

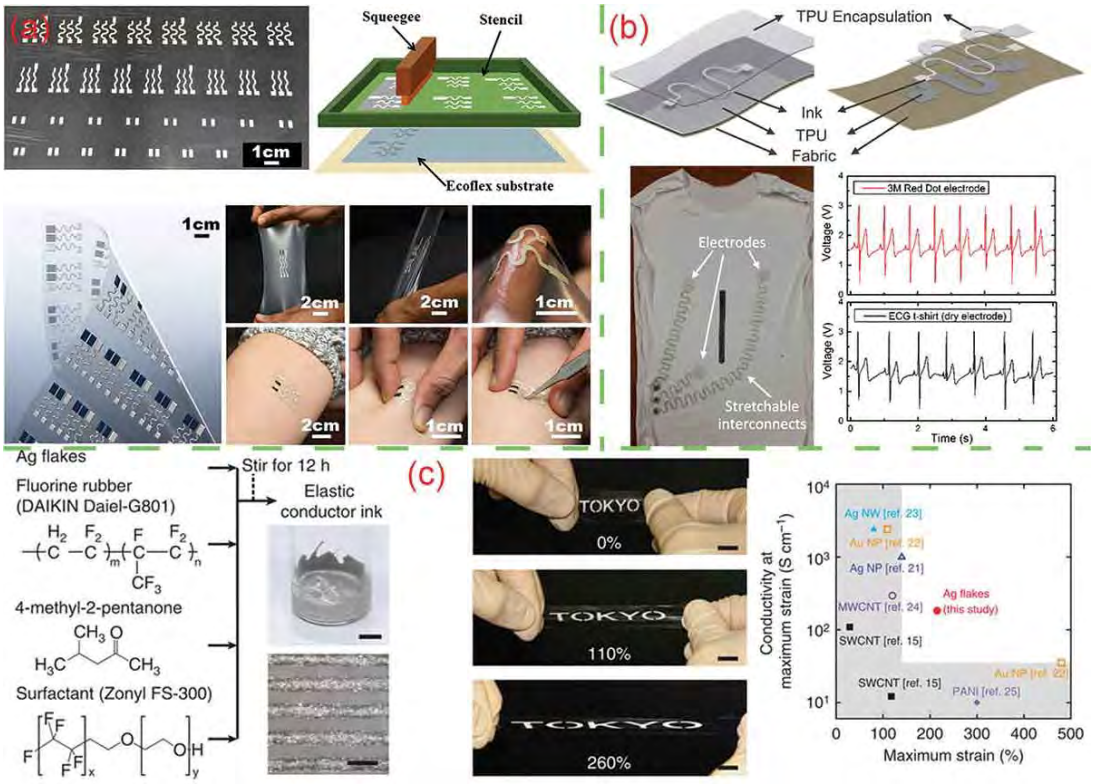

Figure 2.18 (a) Schematic (top left) of screen-printing of a stretchable array of electrochemical sensors using tailored functional inks, and photographs showing different stretching states; (b) Stretchable structure used to connect an electrocardiography (ECG) sensor (top left), inner side of as-prepared ECG T-shirt and recorded ECG signals; (c) Chemical formulas of stretchable Ag flakes-based functional ink, printed elastic conductor and demonstration of the stretchability, and a comparison of this work with other conductive stretchable conductors[73].

The inkjet printing technique is a non-contact patterning approach with a high resolution of ~ 10 μm in the linewidth. Typically, inkjet printing is classified into two types including continuous inkjet mode and drop-on-demand mode. CIJ mode shows advantages in high-speed and thick-layer printing, while drop-on-demand mode facilitates a more precise and thinner deposition of patterns. The size of fillers/particles mixed in the inks for inkjet printing should be compatible with the nozzle size to minimize the probability of clogging. The largest size of the fillers should fulfill the threshold $(D/2a) \geq 150$, where a is the largest size of fillers, and D is the nozzle's inner diameter[74].

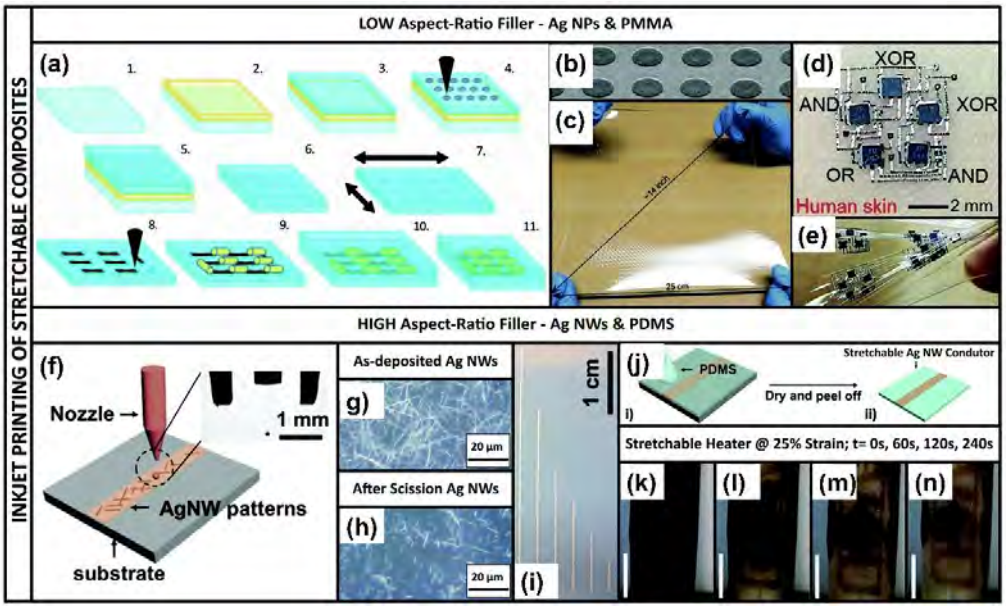

Figure 2.19 Inkjet Printing of stretchable applications[74]. (a) Assembly of stretchable circuits with an ink of PMMA mixed with and Ag NPs. (a1–6, b and c) A substrate of PMMA rigid islands is produced first, and (a8–11) the deposition of conductive tracks and components follows, attaining (d and e) custom stretchable circuits in the end. This process was highlighted due to the use of a low aspect-ratio filler in printable ink, the Ag NPs. (f) Delivery of stretchable conductive patterns with ink composed of Ag NWs. The NWs were (g and h) shortened by ultrasonic-scission. (i) Tracks with lengths greater than 1 cm were delivered on PET foil and (j) impregnated in PDMS to attain a stretchable product, like (k-n) a heater shaped with the letters ‘‘VCU’’ that operated correctly under straining. Scale bars: 1 cm (k-n).

The pros and cons of each patterning technique were summarized in the following table. To sum up, the resolution and fabrication density of these methods is far away from low from that of the standard patterning methods for traditional Si electronic (Table 2).

Table 2 Summary of current fabrication of permeable stretchable electronics.

Patterning method	Resolution (μm)	Density (/cm^2)	Advantages	Disadvantages	Ref.
Inkjet printing	50~3,000	2.85~0.48	Relatively high resolution, cost-effectiveness, and low material consumption.	Limited printing speed, nozzle clogging, coffee-ring issues.	27,53,54,75
Screen/stencil printing	1,000~10,000	0.05~0.2	Industrially scalable capability, low resistance of thick ink.	Time-consuming screen plate preparation.	6,56,58,76
Laser engraving and cutting	100~10,000	0.16~0.67	High efficiency, versatility, cost-effectiveness.	Limited material selection	32,68,69
Pen-writing	300~10,000	0.2~0.44	Cost-effectiveness, easy handling.	Limited ink selections, only for simple structures.	61–63,77
PVD with mask	300~2,000	4~11	High-quality deposited thin film	Relatively low resolution.	65,78
Spray printing	200~10,000	0.08~1.27	Rapid processing	Poor repeatability, and low material consumption.	59,60,79
Textile method	100~10,000	0.4~2	Compatibility with the production of textiles.	Limited by the conductive fiber/yarn selections.	66,67,80
Transfer printing followed by pore drilling	110	0.15	High resolution, complex patterns, compatibility with conventional IC technology.	Multi-step fabrication, low transfer rate when the resolution is high.	81

2.4 Potential Applications of Permeable Stretchable Bioelectronics

2.4.1 Advantages of Permeable Stretchable Bioelectronics

Permeable and stretchable bioelectronics have several advantages over traditional impermeable, rigid, and bulky electronics. Firstly, their permeability allows for better integration with biological tissues, minimizing the foreign body response and increasing long-term biocompatibility[82]. This is particularly important for implantable

devices, as it can reduce the risk of rejection or infection. Secondly, their relatively lower modulus enables a more conformal contact with curved or irregular surfaces[6,82], in comparison to their impermeable counterparts, making them suitable for a wide range of applications, such as wearable sensors or biomedical implants.

Permeable and stretchable bioelectronics with high WVTR value can not only fulfill the basic requirement of insensible perspiration of human skin (i.e., > 20 $g/m^2/h$), but allow skin to "breathe" normally without any discomfort or inflammation under long-term coverage with wearable devices or under intensive training conditions with high perspiration rate (i.e., average ~1000 $g/m^2/h$ of a person). Overall, permeable and stretchable bioelectronics offer a promising platform for the development of next generation bioelectronic devices and systems that can better interface with biology including continuous healthcare monitoring, biomedicine, virtual/ augmented reality (VR/AR), and soft robotics.

2.4.2 Applications in Biomedical Engineering

Electrophysiological signals are critical vital signs for continuous long-term monitoring, as they provide essential clinical cues about an individual's health status. These signals include electrocardiograph (ECG)[83], electromyography (EMG), and electroencephalogram (EEG)[84]. ECG captures electrical signals that reveal the heart's beating process, and continuous monitoring can aid in early diagnosis of cardiovascular disease and ensure prompt management. EMG records electrical signals from skeletal muscles, which can evaluate neuromuscular functions, especially for patients with stroke or Parkinson's disease. EMG signals can also be analyzed for ergonomics, sports science, physiotherapy, rehabilitation, or electrical stimulation. EEG monitoring records brain activity-related electrical potential and can provide vital information on neuronal activities, making it useful for diagnosing brain-related diseases such as epileptic seizures, stroke, and neuromuscular diseases.

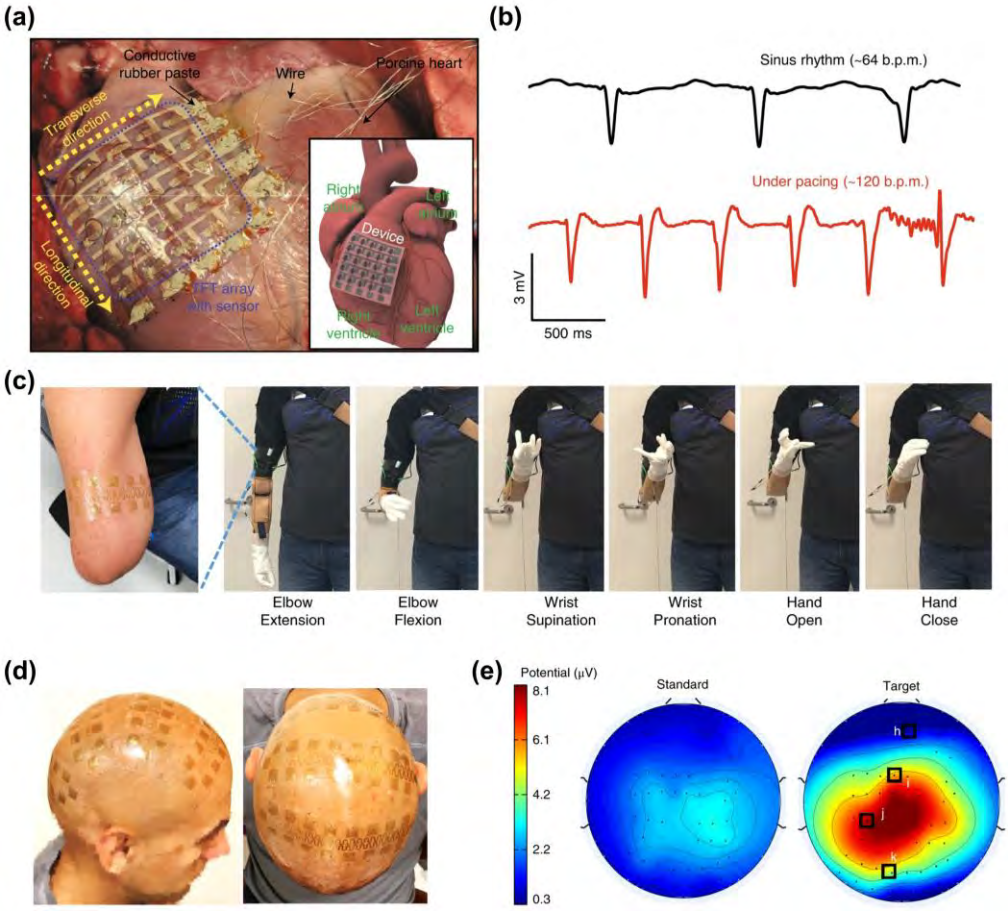

Figure 2.20 Permeable stretchable bioelectronics potentially for continuous electrophysiological monitoring. (a) Digital image of a fully rubbery transistor active matrix on a porcine heart. TFT, thin-film transistor[83]. (b) Representative single-voltage trace from the electrode array with and without pacing. (c) Digital images of a large-area EMG device attached on the amputated upper limb of a subject[84]. (d) Digital images of 68 EEG electrodes covering the scalp of the subject. (e) The scalp mapping image showing the potential difference between target (right) and standard (left) conditions.

Bioelectronics that are both permeable and stretchable have the potential to measure a range of biophysical signals, including temperature, strain, pressure, tactile sensations, and sound[85]. These signals can provide valuable information about an individual's health status, as well as aid in disease prevention, diagnosis, and treatment, physical therapy, and rehabilitation when measured in a continuous, long-term, and comfortable

manner. For example, changes in body temperature have been linked to insomnia, sleep quality, stroke, skin disease, and cognitive functions. Continuous measurement of localized body temperature despite large deformation is crucial for understanding the thermal principle of homeostasis and evaluating complex health conditions.

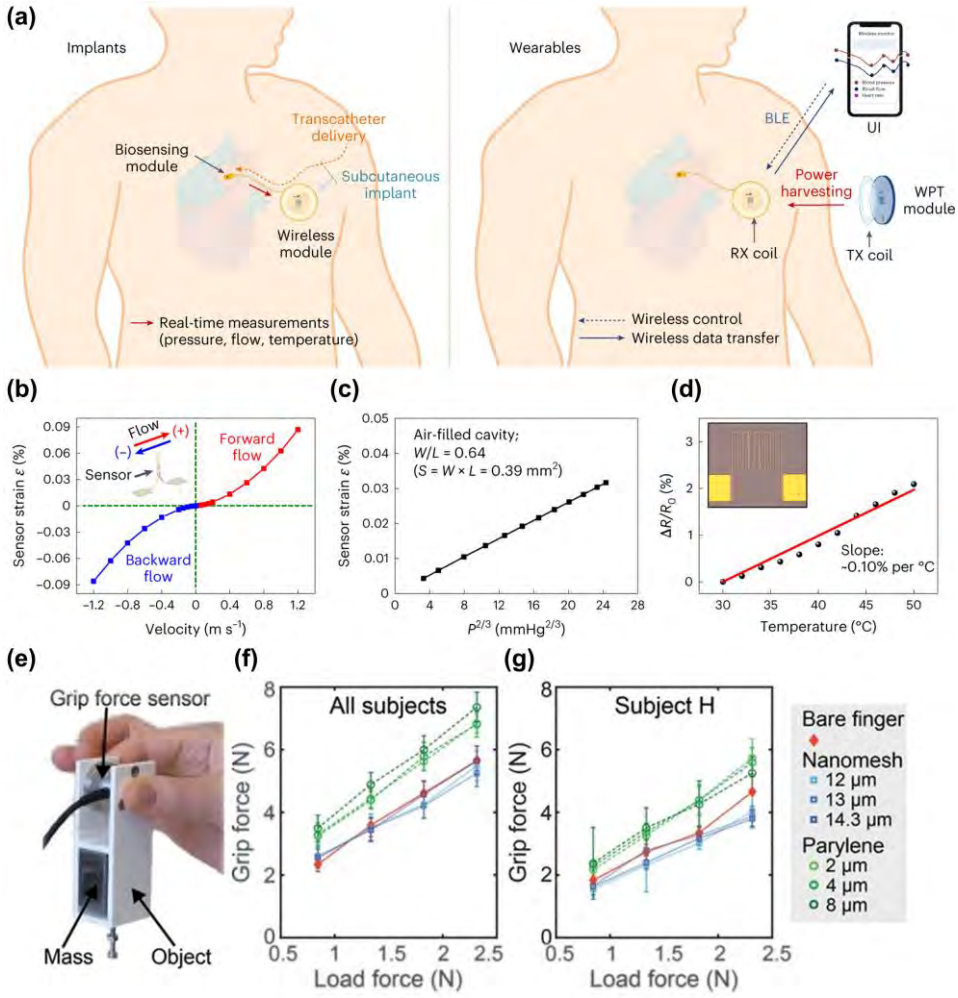

Figure 2.21 Permeable stretchable bioelectronics potentially for continuous biophysiological monitoring. (a) Battery-free, implantable or wearable biosensing module that measures blood pressure, flow velocity and temperatures in the cardiovascular system[86]. (b) Simulation results showing a second-order empirical relationship between the strain in the Si-NM (ε) and the bi-directional flow velocity (v; m/s). (c) Strains of the Si-NM strain gauge as the function of external pressure of blood flow. (d) Temperature sensing performance of the wearable devices. (e)-(g) Experiment setup and the output performance of the subtle sensation effect[65].

In addition to biophysical signals, molecular-level biochemical markers from the human body are a critical and direct indicator of human health. However, traditional clinical practices involve invasive blood retrieval, which can be painful and carries the risk of infection, such as finger pricking in glucose monitoring for diabetics. Soft, on-skin bioelectronic devices have gained significant attention[87] as they provide a non-invasive, continuous method for label-free measurements of disease-related chemical biomarkers from body fluids such as sweat and blood, as well as skin volatolomics. Sweat, for example, contains a range of chemical components, including metabolites (e.g., glucose, lactate, and uric acid), electrolytes (e.g., sodium, potassium, calcium, and chloride), exogenous agents (e.g., drugs and ethanol), proteins, and hormones. This makes sweat one of the ideal body fluids for biomedical sensing.

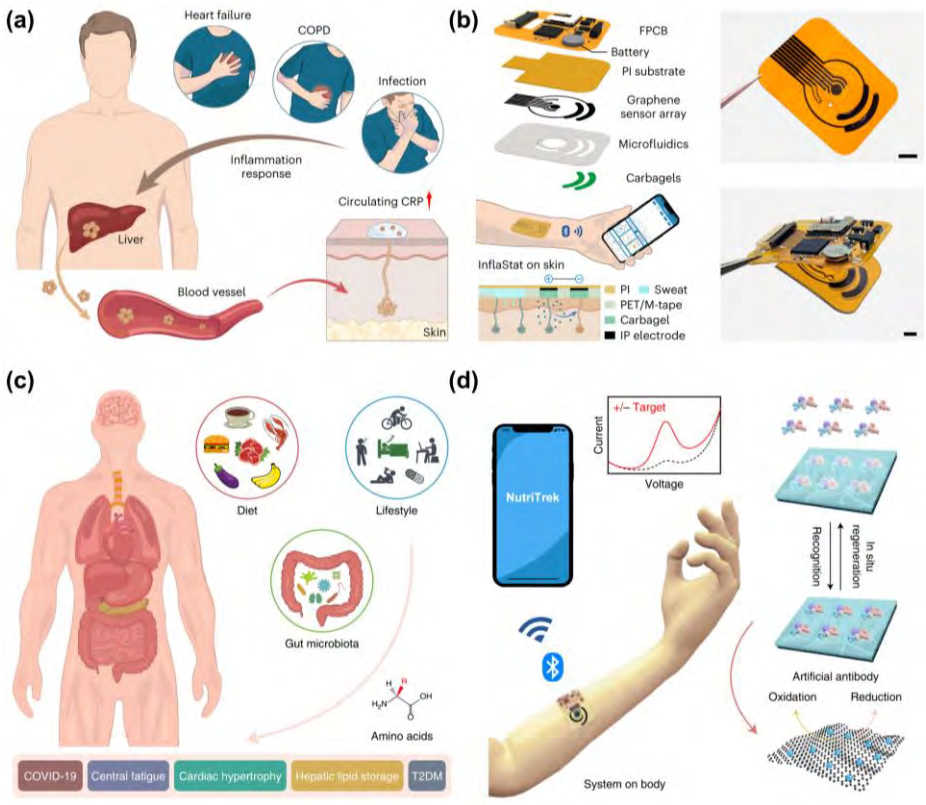

Figure 2.22 Permeable stretchable bioelectronics potentially with biochemical sensing functions. (a) Circulating CRP, released from inflammatory responses, is closely related to various chronic and acute health conditions and could be secreted via the sweat gland. (b) Schematic of wearable

biochemical sensor containing an iontophoretic module, microfluidic module, and multiplexed biochemical sensor array[88]. (c) Circulating nutrients such as AAs are associated with various physiological and metabolic conditions. (d) Schematic illustration of the wearable 'NutriTrek' for continuous metabolic monitoring by a synergistic fusion of LEG, RARs and artificial antibodies[89].

2.4.3 Applications in Future VR/AR

VR and AR are increasingly important in human-machine interactive applications, such as entertainment, remote communication, and training. The future of VR/AR lies in creating a fully immersive experience that includes not only interactive images and sounds but also sensations of touch. Haptic interfaces, developed using mechanoreceptors[90] or electrotactile effects[91], can replicate these sensations. However, most VR/AR devices rely on bulky wires and battery packs that are loosely coupled to the body through textiles, tapes, and straps to provide necessary control. A wireless, monolithically integrated platform with outstanding permeability and stretchability could potentially improve the long-term wearing comfort of VR/AR devices in practical applications.

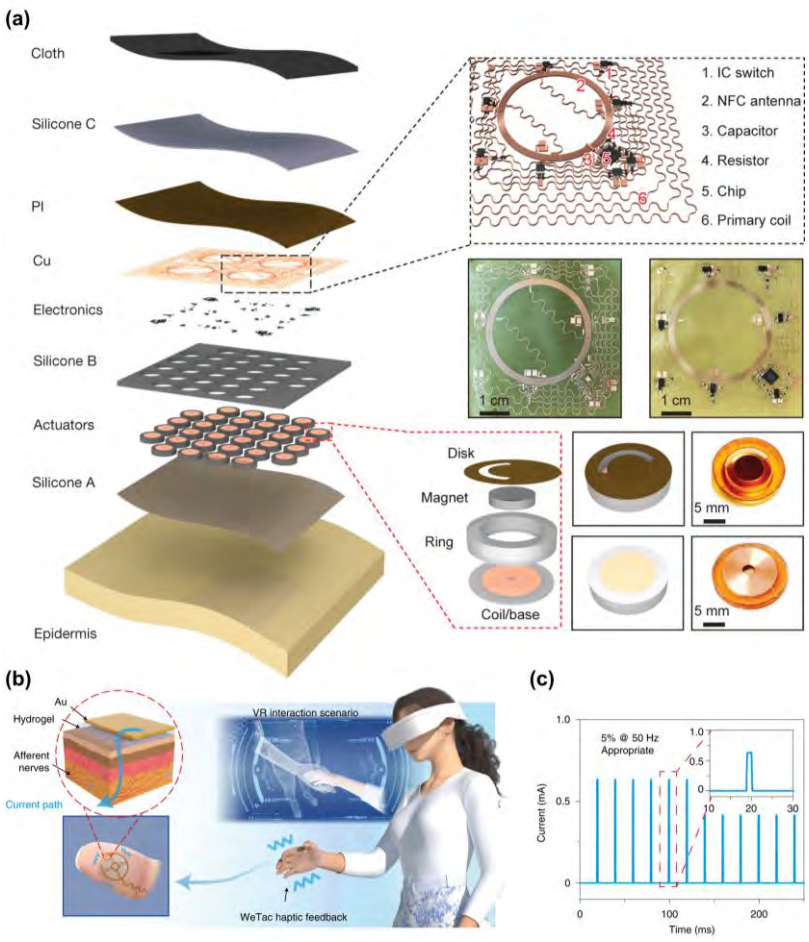

Figure 2.23 Permeable stretchable bioelectronics potentially for future VR/AR. (a) Exploded-view schematic illustration of a haptic interface with 32 independently controlled actuators[90]. (b) Schematics of the electrotactile mechanism and an application in virtual experience haptic feedback. (c) Typical waveform of pulsed current for inducing tactile sensation[91].

2.4.4 Applications in Future Soft Robotics

Permeable stretchable bioelectronics are promising for future wearable rehabilitation exoskeleton with characteristics of soft, lightweight, and comfortable to wear for extended periods, which can be difficult to achieve given their size and weight[92]. In addition, permeable stretchable bioelectronics with superior biocompatibility and miniaturized size are promising for future medical robots for complex surgical procedures[93].

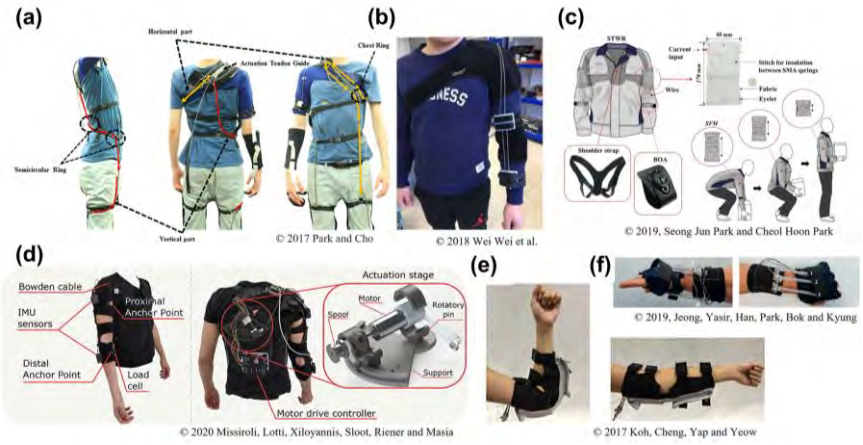

Figure 2.23 Permeable stretchable bioelectronics potentially for soft exoskeletons. Examples of current robotic wearable devices for the upper limb[92] including (a) passive suit for the assistance of the shoulder elevation, (b) cable-driven suit for the assistance of the elbow flexion-extension, (c) shape memory alloy (SMA) suit for the assistance of elbows flexion-extension, (d) cable-driven suit for the assistance of the elbow flexion-extension, (e) pneumatic sleeve for the assistance of the elbow flexion-extension, and (f) SMA glove for the assistance of the wrist flexion-extension and ulnar and radial deviation.

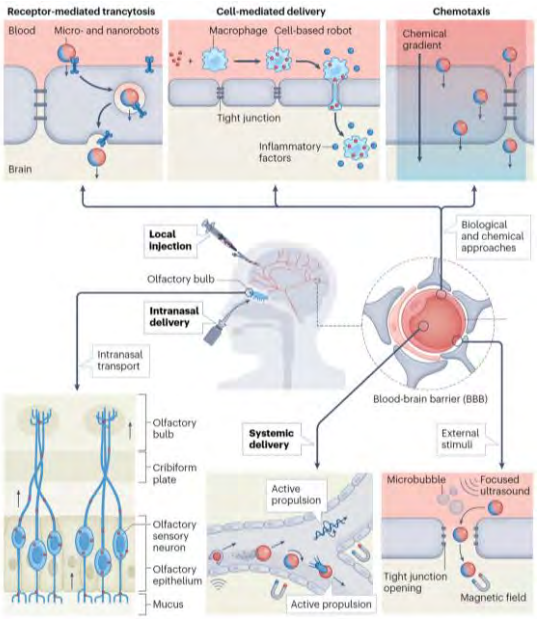

Figure 2.24 Permeable stretchable bioelectronics potentially for soft biomedical robotics[93]. The

penetration of the blood-brain barrier (BBB) and the efficiency of systemic delivery can be enhanced through biological and chemical approaches, such as receptor-mediated transcytosis, cell-mediated delivery, and chemotaxis. Additionally, external physical stimuli, such as focused ultrasound and magnetic fields, can be utilized in conjunction with the active propulsion of micro- and nanorobots to further improve the efficacy of drug and cell delivery.

2.5 Summary of Research Gaps

To sum up, stretchable conductors are the vital components of stretchable electronics, which is crucial for emerging novel technologies and information in the new era. This electronic revolution needs reliable conductors with outstanding conductivity, electrical stability as well as durability.

Further, patterning techniques are crucial but technically challenging for the fabrication of stretchable electronics, especially on permeable substrates. Currently, complex, high-density, multilayered functional devices, and circuits fabrication technology are needed that incorporate permeable stretchable material into a mass-producible way. Until now, the majority of current stretchable electronics are fabricated with impermeable elastic thin films such as PDMS and Ecoflex. Impermeable substrates can create serious health concerns during the long-term wearing of stretchable electronics. Healthy skin requires a microenvironment that is sufficiently permeable to air moisture, and liquid. For the thermoregulation of a human body, "insensible perspiration" has a basic requirement for an evaporation rate of ~600 g/m^2 per day. Inadequate permeability of stretchable electronics will cause uncomfortable sensations during wearing, such as dampness and clamminess. More seriously, a symptom like an allergy and inflammation will further result from skin irritation and occlusion due to being long-term covered with impermeable substrates.

So far, intrinsically stretchable materials with adequate permeability were reported

recently. Notably, the liquid metal fiber mat showed permeable superelastic properties with superhigh electrical stability. But multi-functional, high-density permeable stretchable electronics that are comparable with traditional Si electronics have yet to be demonstrated owning to the lack of scalable patterning micro/nanopatterning for permeable and intrinsically stretchable materials. Therefore, my project aims at the fabrication of permeable stretchable electrodes and developing patterning techniques for permeable stretchable electronics.

Chapter 3: Methodology

3.1 Materials

All the chemicals used in the experiment were used upon received without further purification unless specified. Materials. SBS grans (0.938 g/cm3) were purchased from Kraton Corporation (DX- 1118), liquid metal (EGaIn) was purchased from Sigma-Aldrich. All processing solvents, such as acetone, tetrahydrofuran, dimethylformamide, 1,2-dichloroethane chlorobenzene, are 2-propanol were used as received. Dextran was purchased from Sigma-Aldrich and used as received. Positive photoresist (AZ 5214E, Microchemicals GmbH, Germany), developer for AZ 5214E (AZ 300 MIF, Microchemicals GmbH, Germany), negative photoresist (NR9-1500P, Futurrex, Inc., USA), developer for NR9-1500P (DR6, Futurrex, Inc., USA).

3.2 Fabrication of Permeable Stretchable LM-based Microelectrodes (Plms)

Photolithography plays a significant role in the semiconductor and IC industry, involving the fabrications of ICs, microchips, and MEMS. The mechanism of this patterning technique is to define a desired pattern via exposure of a light-sensitive polymer (photo-resist) to ultraviolet (UV) light. Usually, the wavelength of UV is in the range of 193-436 nm. With the assistance of the photomask, polymer chains of photo-resist are selectively cured and thus the solubility is adjusted. After developing in a specific solvent (developer), the exposed photo-resist is removed or remained to form the desired pattern[82].

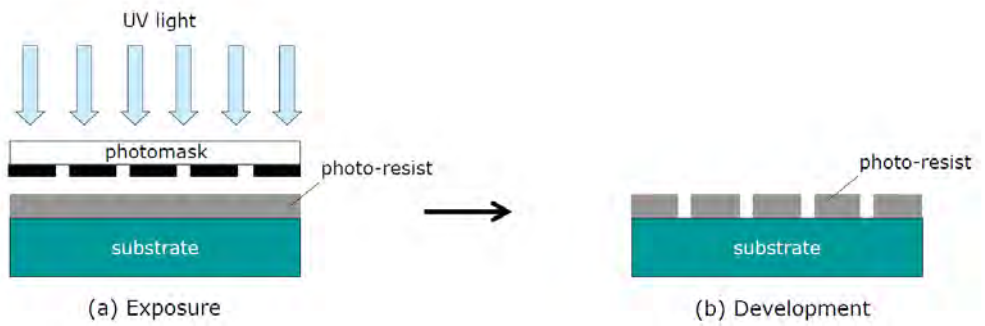

Figure 3.1 depicts the schematic illustration of the main steps in photolithography. This patterned photo-resist can be used as a protective layer in subsequent etching or deposition processes to build topography on the substrate[82].

Before patterning the Ag microelectrodes, a thin dextran layer (10 wt% in water) was spin-coated at 4,000 rpm for 40 s on the clean and dry SiO_2 wafer. Here the Ag patterns were fabricated on the dextran layer via photolithography. After spin-coating with negative photoresist NR9-1500P at 4000 rpm for 40 s, followed with the pre-baking treatment on a hotplate at 155 ℃ for 1min. The photoresist was exposed under UV light with a dose of 170 mJ/cm^2 on the mask aligner (Suss MA6). Next, the photoresist was post-baked at 105℃ for 3 min and developed in DR6 developer for 10-15 s. After rinsing the sample in water and drying with compressed nitrogen gas, a 500-nm-thick Ag layer was deposited by thermal evaporation and was lifted off in acetone.

Electrospinning is a very simple but effective and high-throughput method to fabricate fiber mats from nanoscale to microscale. Compared with other spinning methods like wet spinning, thermal drawing, and extruding, electrospinning shows several advantages including 1) versatility, in which a hundred polymers both natural and synthetic can be used, 2) simplicity, experimental setups can be easily constructed in the laboratory, 3) capability for large-scale production[94]. The porous structure of electrospun mats allows the penetration of air and moisture, and the accommodation of active materials. In addition, by using highly elastic polymers, the fiber mat can be superelastic.

The experimental setup of electrospinning is shown in the following Figure 3.2, when a high-voltage field is applied between the spinneret and the collector, the electrostatic charges accumulate at the surface of the polymer solution at the tip of the spinneret. Then, the shape of the solution is changed from a spherical surface to a cone shape (Taylor Cone) because the increased charge repulsion overcomes the surface tension of the solution, and a jet is extruded from the spinneret in a straight path and then travels with a drastic whipping toward the collector at the electrostatic field. The continuous polymeric fiber is formed during the flying of the jet due to the evaporation of the solvent and the stretching of electrostatic force. By adjusting parameters such as voltage, the concentration of polymer solution, feeding rate, collection distance, and duration, various morphology and thickness of fiber mats can be obtained.

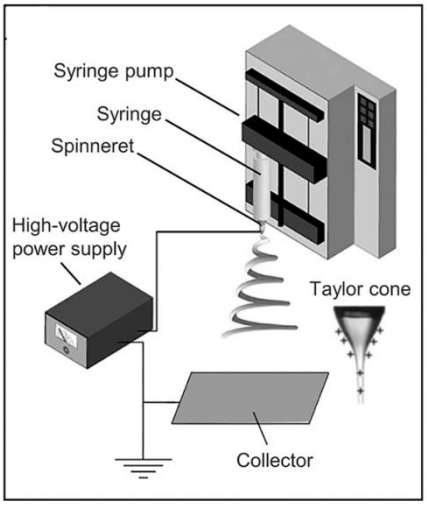

Figure 3.2 Schematic illustration of electrospinning[94].

The additive electrospinning of the SBS mat was conducted on top of the Ag patterns. Firstly, the SBS solutions were prepared by dissolving SBS particles in the mixture solution (THF/DMF =3:1) with a weight ratio of 15 wt%. Next, the SBS solution was put into the syring where the distance between the needle tip and the collector is about 20 cm. A high voltage power supply is provided at the needle tip of +18 kV and the collector of -2 kV. The feed rate of SBS solution is at 3 ml min^{-1} while the collection

time is varied to change the thickness of SBS mats. After plasma treatment, the patterns were immersed into water to dissolve the dextran layer, allowing the transfer of the Ag patterns onto the SBS mat. Finally, LM was selectively coated onto the Ag layer in the glovebox to obtain the LM microelectrodes.

3.3 Fabrication of LM-based Hydrogel Microelectrodes (PlmHs)

The fabrication of the ink on the donor substrate was similar to that of Plms. The synthesis began with dissolving acrylic acid (AA) (30.0 wt%), HMPP (0.4 wt%) and MBAACaCl2 (0.5 wt%) in the mixture of water and glycerin (50 wt%) to form solution. After exposure under UV light (wavelength 365 nm; 15 W) for 150 s, the Ag electrodes were transferred from the Si wafers to the hydrogel. Finally, LM was selectively coated onto the Ag layer in the glovebox to obtain the LM microelectrodes on the hydrogel.

3.4 Characterizations

The surface morphology and elemental mapping of the samples were collected by scanning electron microscopy (SEM, TESCAN VEGA3). Resistance of various linewidths of PLM lines (length = 10 mm) was measured via direct current (DC) I–V characteristics with a parameter analyzer (Keithley 4200A-SCS Parameter Analyzer) connected with a probe station (Micromanipulator). The resistance of PLMs under different strains was measured by the four-probe method with a source meter (Keithley 2400) coupled with a customized stretching machine (Precise). Active and passive electronic components, such as resistors, capacitors, and inductors, were characterized using an LCR meter, and the resonance frequency of the LC circuit was investigated using a network/spectrum/impedance analyzer.

The air permeability tests were conducted according to ASTM D737-08 standard using

a MO21S air permeability tester (SDL Americ, Inc.). The pressure of the airflow was set as 100 kPa. Moisture permeability tests were performed according to the standard E96/E96M-13 by the cup method. The testing duration was 72 h. Both air resistance and moisture permeability tests were performed at constant temperature (22 °C) and humidity (63%)

Electrical and mechanical characterizations of Plms. The electrical conductivity (σ) of Plms was calculated according to the formula $\sigma=L/(A\times R)$, where L, A, and R are the length, cross-sectional area, and electrical resistance of the Plm, respectively. A of Plms was determined by the surface profiler (New Zygo NexView), and the integrated polygon area was calculated using the software OriginPro 8.5. R of the Plms with different linewidths (L = 10 mm) were measured via direct current (DC) I–V characteristics with a parameter analyzer (Keithley 4200A-SCS Parameter Analyzer) connected with a probe station (Micromanipulator). The electrical resistance of Plms under different strains was measured by a four-terminal method with a source meter (Keithley 2400) coupled with a customized stretching machine (Precise).

Electrochemical Characterizations. Electrochemical impedance spectroscopy (EIS) was conducted using an electrochemical workstation (CHI 660E) with a three-electrode testing system. Ag/AgCl (2M KCl), platinum foil, and the Plm were performed as the reference electrode, counter electrode, and working electrode, respectively. 1×phosphate-buffered saline (PBS) solution (Gibco) was used as the electrolyte. Impedance and phase angle as a function of frequency ranging from 1 Hz to 10,000 Hz were recorded by an AC sinusoid signal amplitude of 10 mV. The EIS spectra of Plms stretched with various strains were acquired with the same electrochemical workstation coupled with a homemade stretching setup.

Biocompatibility tests. Specimens for the cell cytotoxicity tests included with the control sample, absorbent gauze, SBS mat, patterned Ag-SBS mat, PLM, and 20%

dimethylsulfoxide (DMSO). L-929 cells (ATCC, US) were used to investigate the in vitro cytotoxicity of all the specimens following the ISO 10993-5: 2009(E) standard. All the L-929cell were seeded in the full Dulbecco's Modified Eagle's Medium (DMEM, Hyclone, Hong Kong) supplemented with 10% fetal bovine serum (FBS, Hyclone, Hong Kong) and 1% penicillin/streptomycin (PS, Hyclone, Hong Kong) in a 24-well plate with the seeding density of cells 6×10^4/mL. After incubation for 24 hours and the verification of the cell confluency and morphology, the medium was discarded, and 1 mL of the fresh full medium was added to the culture plate. Next, 0.2 cm^2 sterile specimens were directly added to the 24-well plate to evaluate the cytotoxicity of the materials. The fresh full medium, absorbent gauze (0.2 cm^2), 20% DMSO/full medium mixture was used as a blank, negative, and positive control. All specimens were cultured at 37°C in an incubator with 5% CO^2.

After discarding the culture medium, the staining solution containing phosphate buffer saline (PBS, 200 μL), 2 μM calcein AM, and 8 μM propidium iodide (PI) was added, followed by incubation for 45 min. Then, a fluorescent microscope (Zeiss, Germany) was used to observe the cells which were rinsed with PBS. For the cell proliferation examination, 500 μL MTT solution was added to each well followed by incubation for 2 h. Next, 500 μL DMSO was added to dissolve the formazan. The absorption at 450 nm denoting the cell metabolic activity was measured with a plate reader (BioTek, US). The cell viability was determined with the absorbance ratio between the tested well and the blank control well.

The animal experiments of the specimens were performed following the ISO 10993-10:2010(E) standard. All procedures followed the ethical guidelines for experimental animals, which were approved by The Hongkong Polytechnic University. Six New Zealand White Rabbits of 2.0-3.0 kg were used for this study. Four samples (2.5×2.5 cm square) were attached to each rabbit. These samples were divided into seven groups: group 1: negative control (thin cotton cloth), group 2: positive control (thin cotton cloth

rinsed with saturated sodium dodecyl sulfonate (SDS) solution), group 3: SBS mat, group 4: SBS mat with patterned serpentine Ag (Ag-SBS mat), group 5: Plm with serpentine structure, The backs of the rabbits were shaved in advance 24 h before the attachment of the specimens. Each group had three sample patches, which were applied onto the skin underneath the gauze pads (2.5×2.5 cm) secured with the semi-occlusive medical sterile wound dressings (Hynaut, Tsingtao, China). The patches were removed after exposure to the shaved skin for 24 h. Then, after being cleaned with lukewarm water, the test sites were observed at 0 (initial), 24, 48, and 72 h after sample attachment for visible changes like erythema. The mean erythema scores (MES) were measured on a scale from 0 to 4, in which grade 0 indicated no erythema, grade 1 indicated slight erythema, grade 2 indicated moderate erythema, grade 3 indicated moderate to severe erythema, and grade 4 indicated severe erythema.

Characterizations of the shear storage modulus of PlmH. Shear storage modulus served as a metric for characterizing the crosslinking density as a function of UV exposure time. Measurements used a TwinDrive rheometer (MCR702; Anton Parr) with a 25-mm-diameter cone plate (CP25) at an amplitude and angular frequency of 1% and 1 Hz, respectively. UV exposure began at 30 s and ended at 150 s. Data were collected using the RheoCompass software (Anton Paar). Adhesion energy. Characterization involved peeling adhering specimens (50 mm × 25 mm × 2 mm) from the tissue surfaces and encapsulation/substrate materials of the devices (50 mm × 25 mm; various thicknesses for different materials).

3.5 Electrocorticography (ECoG) Neural Signal Recording

Rat surgery. All procedures following the animal studies and the experimental protocols were reviewed and approved by the Animal Research Ethics Sub-Committee, Research Committee at the City University of Hong Kong (approval number A-0664). Male Sprague Dawley rats were ordered from the Laboratory Animal Services Centre, Chinese University of Hong Kong (aged 7-8 weeks, 200-300 g). All rats were housed in Laboratory Animal Research Unit, City University of Hong Kong, under 12 h:12 h light/dark cycles until experiments. Before the surgery, the rats were firstly anesthetized with gaseous isoflurane (2 L/min air mixed with 3% isoflurane), and then deeply anesthetized with pentobarbital sodium (30 mg/kg). After anesthesia, the rat head was shaved under 37°C. The midline skin incision was first made over the craniovertebral junction. The overlying muscles were then cut and retracted to expose the skull. A craniotomy was performed using a dental drill, and then the dura was peeled off using a fine tweezer to ensure full exposure of the cerebral cortex.

For optogenetic study of PlmH, viral injection and optogenetic stimulations were needed. SD Rats were anesthetized with pentobarbital (50 mg/kg, i.p.) and placed in a stereotaxic frame. After craniotomy, a volume of 0.5 µl per hemisphere AAV5 containing CaMkii-ChR2-eYFP vectors (titer 4 x 10^12, Taitool) was injected into the somatosensory cortex region (AP -3.3 mm, ML 3.0 mm, DV 2.0 mm), at a rate of 0.2 µl min-1 with a 10 µl microsyringe with 33-gauge metal needle (Hamilton, NV, USA), controlled by a microsyringe pump (World Precision Instruments, FL, USA) and its controller (WPI). After the injection, the needle was kept in the place for an additional 5 min to facilitate the diffusion of the virus after which it was slowly withdrawn. Rats were kept for three weeks after virus injection to allow genes expression.

Three weeks later, after anesthetization the skull was exposed and small holes (8 mm wide, 10 mm long) were drilled above the cortex for electrodes placement. Two

stainless bone screws were placed into the skull surrounding the surgical openings and the dura mater was subsequently removed. Electrode arrays were placed on the cortex. Finally, a low-resistance 200 μm silver wire from each array was wrapped around one of the bone mounting screws for grounding. In the optogenetic manipulation groups, optical fiber was connected a blue light laser (MBL-473/200 mW; Fiblaser). 7-10 mW mm^{-2} 473 nm blue light was delivered to each optical fiber terminal upon somatosensory cortex region at 20 Hz (square wave with 10% duty).

Electrocorticography (ECoG) neural signal recording and electrical stimulations. The Plm array bonded on a flexible printed circuit (FPC) connector was connected to a printed circuit board with a customized FPC adaptor, and then ECoG neural signals were recorded with a multi-channel high-precision data acquisition system (PowerLab 16-35, AD Instruments). Signals were acquired and digitally band-pass filtered (1-30Hz) by matched software LabChart. Sequential electrical stimulations were performed on both the left and right forelimbs of the rat using square wave voltage pulses with various applying frequencies (1, 3, and 9 Hz) and intensities (1, 3, and 6V) generated by the stimulation output port of the PowerLab through a BNC cable. A total of 50 pulses were delivered at a frequency of 1 Hz for each stimulus condition, and 50 responses per stimulus condition were averaged. A custom Matlab code was adopted for analyzing the spectrogram of the ECoG neural signals.

Cryosection, histological staining, and observations of the brain slice. After the implantation of the Plm array, the histological status of the brain slice was first studied. To protect the tissular structure, the specimen was fixed in a PBS solution with 4 wt% formaldehyde for 24 h and transferred into 30% sucrose solution overnight, after which it was transferred to sucrose-Cryo-OCT compound before frozen sectioning. Then the brain specimen was frozen at -80 °C and sliced with the freezing microtome (CryoStar NX70) with a block thickness of 15 μm. Hematoxylin and Eosin (H&E) staining method was adopted by using the basic dye hematoxylin (BL 735A-1) for the staining

of acidic cell components (i.e., nucleic acids, glycosaminoglycans, and acid glycoproteins), and the acidic dye eosin (BL 735B) for the staining of the cell cytoplasm. Specifically, the slices were first stained with hematoxylin solution for 5 min after cleaning with DI water. Then the slices were thoroughly rinsed in DI water, followed by differentiation in the 0.1% acetic acid and 85% ethanol in water for 10 s, and rinsing again with DI water for 1 min. Next, the slices were blued in the PBS/PBST solution for 30 s and then rinsed with DI water. After washing the blued slice in ethanol for 10 s, eosin was also applied to stain the tissue for 30 s. Finally, the slices were dehydrated in ethanol (95%) and permeabilized in xylene two times (5 min each), respectively. For immunohistochemical analysis, slices were observed with the invert microscope (Nikon Eclipse Ti).

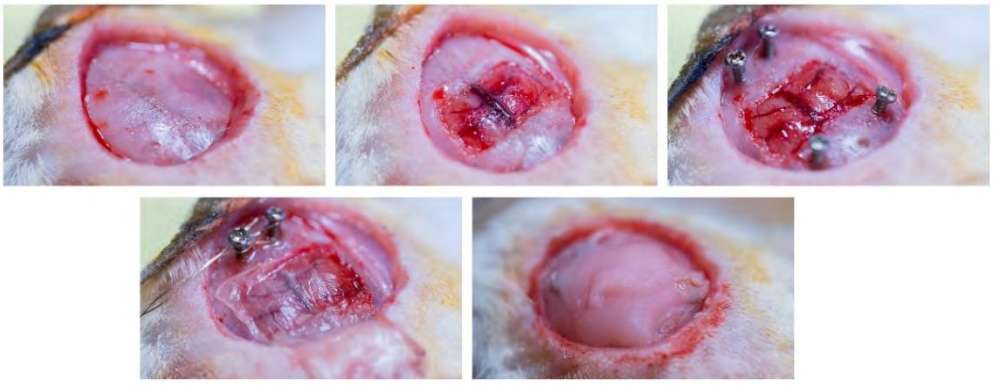

Figure 3.3 Digital images showing the procedure of craniotomy for the chronic implantation of the ECoG electrodes. Three stainless bone screws were placed into the skull surrounding the surgical openings and the dura mater was subsequently removed. Electrodes were put over the left and right cortical surfaces, respectively. The craniotomy was filled with Kwik-Sil silicone elastomer, then coated with dental cement after the Kwik-Sil was cured.

Chronic (long-term) biocompatibility test of implanted Plms. For the biocompatibility test on the brain, we implanted the electrodes (Plm, Au/PI, Au/PDMS with the same electrode design) into the cerebral cortex to evaluate their chronic biocompatibility. In this study, male ICR mice (6-8 weeks, n = 2) were anesthetized with intraperitoneal injected ketamine (100 mg/kg) and xylazine (10 mg/kg) and fixed on a stereotaxic frame. As shown in Figure 3.3, the craniotomy was performed between the bregma and lambda of the skull (AP -1.5 to -4.5; ML 0.5 to 3.5). Three stainless bone screws were placed into the skull surrounding the surgical openings and the dura mater was subsequently removed. Electrodes were put over the left and right cortical surfaces, respectively. The craniotomy was filled with Kwik-Sil silicone elastomer (World Precision Instruments, Inc.), then coated with dental cement (Megadental, Germany) after the Kwik-Sil was cured. The mice were sacrificed at 2 weeks and taken for immunohistological analysis to evaluate their biocompatibility.

We anesthetized the mice by intraperitoneal injection of ketamine (100 mg/kg) and xylazine (10mg/kg) and then perfused the mice transcardially with PBS followed by 4% paraformadehyde (PFA). The brain samples were incubated in PFA overnight and then with 30% sucrose solution for 3 days. Brains were cryosectioned at a thickness of 30 μm. The slices were stained with Iba1 antibody (Abcam, ab178846) and DAPI (nuclei marker), and observed with laser confocal microscopy (Nikon A1HD25, Japan). The regions of interest for the assessment of intensity and soma size of Iba1 positive cells were chosen from the electrode−brain interface to the tissues 600 μm beneath the interface (3 slices for each mouse). We analyzed the intensity and soma size of Iba1 positive cells using ImageJ software.

For investigating the chronic biocompatibility of various electrodes in the biceps femoris muscle, healthy male Sprague Dawley rats (aged 4-5 weeks, 200g) were utilized for biceps femoris muscle implantation. The Dawley rats were first treated with gaseous light anesthesia (isoflurane), followed by the injection of ketamine (1 wt%) for

deep anesthesia. Then a required wound (6 mm in width and 2 mm in depth) was created, with the attachment of the electrode array (Plm, Au/PI, Au/PDMS) on the surface of the biceps femoris muscle. After suturing and implanting for one week, the samples were collected and frozen sectioned (25 μm thick) using CryoStar NX70 Cryostat (ThermoFisher). Stained by H&E (Abcam) method, the slices were later observed with an invert microscope (NikonTi2-A).

3.6 Fabrication of Wireless Permeable Three-dimensional (3D) Integrated Electronic Skins

Here we patterned the permeable and stretchable LM 3D circuits (LM antennas, traces, connections, contacts, etc.) using the previous fabrication protocol for permeable stretchable LM microelectrodes. Then the Ag microcircuit was transferred to the electrospun SBS fiber mat, followed by selective wetting of LM in the glovebox. Next, another SBS fiber mat was additively electrospun onto the LM circuits, and stiff LM (80 °C, 16 h) was stencil printed as the pads and paste for the paste mask layer. The interlayer electrical interconnections were created using two methods. For thin interlayers (i.e., paste mask layer with a thickness of ~30 μm), LM pads can easily penetrate through the permeable structure for interlayer electrical connections. For thick interlayers (i.e., insulator layer between two layers of LM 3D circuits), the LM pad can fill the laser-cutting Vertical interconnect accesses (VIAs) for the interlayer electrical connections. Finally, commercially available microchips were mounted on the paste mask layer with the bonding sites (fluidic LM) and encapsulated with another permeable superelastic electrospun fiber mat.

Wireless communication. The WPE-skins typically adopted Bluetooth (BLE) integrated MCU (CC2640, Texas Instruments) to achieve data acquisition, transmission, and functional control. Code composer studio (CCS) was used for MCU programming.

The Android application used for communication by mobile devices was developed by Android Studio. A detailed circuit diagram design and the PCB design can be found in Figure 3.4. The components are listed in Table 3.

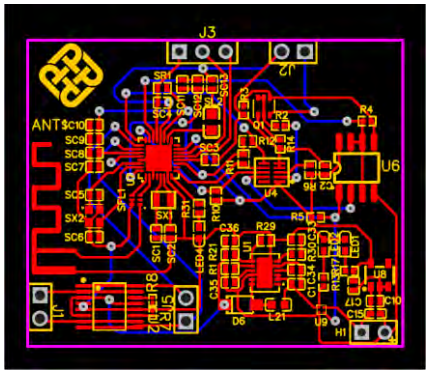

Figure 3.4 PCB design of the P3D-eskin system with wireless communication using Bluetooth technology.

Table 3 Bill of materials of the P3D-eskins using Bluetooth.

ID	Name	Designator	Footprint	Quantity	Manufacturer Part
1	50	R14,R3	R0402	2	
2	HDR-M-2.54_1x2	J1,J2,J5	HDR-M-2.54_1X2	3	
3	HDR-M-2.54_1x3	J3	HDR-M-2.54_1X3	1	
4	1k	R7	R0201	1	
5	0	R8	R0201	1	
6	TMUX7211PWR	U2	TSSOP-16_L5.0-W4.4-P0.65-LS6.4-BL	1	TMUX7211PWR
7	0.1u	C2,C15	C0402	2	
8	1uH	L21	L0603	1	
9	100	R2	R0402	1	
10	NC	R4	R0402	1	
11	10K	R5	R0402	1	
12	270	R13,R17,R31	R0402	3	
13	48k	R29	R0402	1	
14	CC2640R2FRSMR	U7	VQFN-32_L4.0-W4.0-P0.40-TL-EP	1	CC2640R2FRSMR
15	TPS22910AYZVR	U9	DSBGA-4_L0.9-W0.9-R2-C2-P0.50-BL	1	TPS22910AYZVR
16	ANTENNA	ANT1	RN-ANT	1	
17	LM258DRG4	U6	SOIC-8_L5.0-W3.2-P1.27-LS8.3-BL	1	LM258DRG4
18	TPS76933DBVR(PB-FREE)	U8	SOT-23-5_L3.0-W1.7-P0.95-LS2.8-BR	1	TPS76933DBVR(PB-FREE)
19	MBR0520	D6	SOD-123FL_L2.7-W1.8-LS3.8-RD	1	MBR0540
20	LED-0402_G	LED2,LED1,LED4	LED0402-R-RD	3	19-217/GHC-YR1S2/3T

21	10k	R6,R11	R0402	2	
22	2.4k	R10,R12	R0402	2	
23	DAC60502	U4	DRX0010A	1	DAC60502DRXT
24	FFB5551	Q1	SOT-363_SC-70-6	1	
25	4.7u	C1,C17	C0402	2	
26	2.2n	C33	C0402	1	
27	1u	C10,C34,SC3	C0402	3	
28	10n	C35	C0402	1	
29	22u	C36	C0402	1	
30	20k	R1	R0402	1	
31	1M	R21	R0402	1	
32	36.5k	R30	R0402	1	
33	LT8364EDE#PBF	U1	DFN-12_L4.0-W3.0-P0.50-BL-EP	1	LT8364EDE#PBF
34	0.1uF	SC9,SC7,SC8,SC11,SC12	C0402	5	
35	10uF	SC10,SC13	C0402	2	
36	10uH	SL2	L0603	1	
37	NO	SFL1	2450BM14G0011	1	
38	HDR-F-2.54_1x2	H1	HDR-F-2.54_1X2	1	
39	100k	SR1	R0402	1	
40	24MHz	SX2	OSC-SMD_4P-L2.0-W1.6-BL	1	TAXM24M4ZCBCDT2T
41	12p	SC1,SC2,SC5,SC6	C0402	4	
42	100n	SC4	C0402	1	
43	32.768KHz	SX1	OSC-SMD_L2.0-W1.2	1	SC-20S32.768kHz20PPM9pF

Finite element analysis (FEA) of the WPE-skin system. Static structural mechanics of the systems are analyzed through FE simulations. Material mechanical parameters are summarized in Table 4. The Poisson's ratio of LM is assumed to be the same as that of the substrate. The surface of LM hardens as a result of oxidation when heating in air and therefore the oxidation of partially oxidized LM is taken as a range from 9.8 E4 to 3.1 E5 Pa. Three systems are investigated, i.e., serpentine copper circuit, LM circuit, and a chip with LM connections. These systems are subjected to mechanical tension of 50% strain. It is noted that to facilitate comparison, the SBS substrate of the serpentine copper circuit is subjected to a strain of ~ 800% so that the strain of the circuit part is close to 50%. The stress responses are collected. The ratio of the maximum stress to the average stress is used as the stress concentration factor, i.e., $\sigma_{max}/\sigma_{avg}$.

Table 4 Summary of the input parameters for FEA of the stress distribution of LM antenna and the structured Cu antenna.

Material	Thickness (μm)	Diameter (mm)	Oxidation (Pa)	Poisson's ratio
Copper	18	~32	1.1 E11	0.34
SBS substrate	200	100	1.0 E5	0.47*
Aluminum oxide	880	-	3.75 E10	0.22
Liquid metal	50	~32	2.0 E5	0.47*
Gradient liquid metal	<900	-	9.8 E4 – 3.1 E5	0.47*

* The Poisson's ratio of liquid metal is assumed to be the same as that of the SBS substrate.

Transcutaneous electrical stimulations and the measurement of electromyography (EMG) signals. The electrical stimulation electrodes and the EMG electrodes were first integrated into the WPE-skins. Next, the output voltage and current data were measured by a DAQ (data acquisition) multi-meter system (Keithley DAQ6510) at a sampling frequency of 10 kHz. The EMG signals were measured using a high-precision data acquisition system (PowerLab 16/35, AD Instruments) and with a biological signal amplifier (BioAmp FE132, AD Instruments) with a sampling rate of 1 kHz. The raw signal data were digitally filtered by a notch filter at 50 Hz and then a low-pass filter with a cut-off frequency of 30 Hz.

Characterizations of the near-field communication (NFC) WPE-skin system. To develop a battery-free type of WPE-skin, we adopted an NFC-embedded MCU (RF430FRL152H, Texas Instruments), and modified the temperature sensing circuit from reference design (TIDM-RF430-TEMPSENSE). Characteristics of the LM inductive antenna including inductance, Q factor, impedance, and phase were characterized using an impedance analyzer (E4991B, Keysight Technologies). The mobile app GUI for temperature sensing is "RF430FRL152H Demo" provided by Texas Instruments.

Chapter 4: Wafer-scale-patterned Permeable, and Stretchable LM Microelectrodes (Plms)

4.1 Introduction

Stretchable and soft electronics are having an edge over rigid and brittle electronic devices in human-machine interactive applications such as soft robotics[84,95], biomedical treatment[96,97], healthcare monitoring[65,98], and augmented reality[90,91]. Among which the intrinsically stretchable material is a rational selection due to their low modulus, dielectric and renderable properties[10]. However, as discussed in the literature review part, manufacturing such materials and devices still poses an enormous challenge owing to their incompatibility with traditional electronic technologies concerning high temperature and organic solvent treatment. Currently, some strategies have been proposed including lithography-based (photolithography, stencil, imprinting, transfer printing), injection, additive (inkjet printing, 3D printing), and subtractive printing (laser ablation, in-plane recapillarity. Nevertheless, most reported substrates for these electronics show limited permeability toward air and perspiration. The limited permeability impedes the long-time wearing comfort of these wearable electronics and even causes inflammation. Yet, permeable substrates are known to be porous and rough, which hinders the patterning features, intact electrical interconnects, and normal functions of stretchable and soft electronics. Therefore, it's challenging but indispensable to manufacture intrinsically stretchable and soft materials on permeable substrates for enhancing the wearing coziness and physical health during long-term applications.

Recently, gallium-based liquid metal (LM) has been widely reported as a highly conductive (>3 x 10^4 S/cm), soft (modulus ~0 MPa), and biocompatible material for the fabrication of bioelectronics through various patterning strategies, which include

lithography-enabled patterning, injection, additive process, and subtractive process. However, moat existing patterned electronics were neither permeable nor biocompatible. Alternatively, current patterning techniques on permeable substrates including inkjet printing, screen/stencil printing, laser engraving and cutting, pen writing, physical vapor deposition (PVD) with mask, spray printing, textile method, transfer printing, which showed relatively low resolution (50~1000 μm) and device density (0.05~11components or devices/cm^2), thus hindering the integration of high-density and multifunctional bioelectronics with integrated circuit (IC) technology.

Here we developed a new technology for micropatterning of permeable stretchable electronic devices and systems using liquid metal (LM). By taking advantage of the permeable structure, wafer-scale microelectronic devices are integrally transferred within minutes upon etchant exposure. Further, LM selectively wet the micropatterns on the porous mat, enabling the soft, stretchable, and biocompatible electronics on the permeable mat. The resulting LM microelectrodes showed a minimum patterning feature of ~2 μm and an ultrahigh density of 75,500 components/cm^2 and 100 devices/cm^2 on a system level for a neural-machine interface.

4.2 Fabrication of Plms and the Patterning Features

Figure 4.1a shows a schematic of the scalable microfabrication process of permeable LM-based microelectrodes (pLM). The fabrication consisted of four fundamental steps: microstructure fabrication of Ag patterns on the water-soluble sacrificial layer (dextran) using commercial lithography techniques (i.e., photolithography), additive fabrication of the poly(styrene-block-butadiene-block-styrene) (SBS) mat via electrospinning, the release of the sacrificial layer from the carrier wafer (SiO_2), and selective wetting of

LM with Ag patterns. In comparison to the structural engineering of rigid devices and interconnects, intrinsically stretchable electronics showed advantages in terms of mechanical deformability, skin compatibility, and device density. Great progress has been achieved in fabricating polymeric thin-film stretchable electronics via transfer printing. Considering the time-consuming dissolving of the sacrificial layer (dozens of hours) and the limitations of impermeable stretchable electronics in wearing/implanting, we developed a new route for intrinsically stretchable electronics. For one thing, the porous structure enables an omnidirectional etching and dissolving of the sacrificial layer and thus enables a rapid (within minutes) and defect-free transfer, obviously enhancing the transfer efficiency. For another thing, the resulting stretchable electronics exhibit permeability towards air and moisture for long-term wearing/implanting comfort (Figure 4.1b).

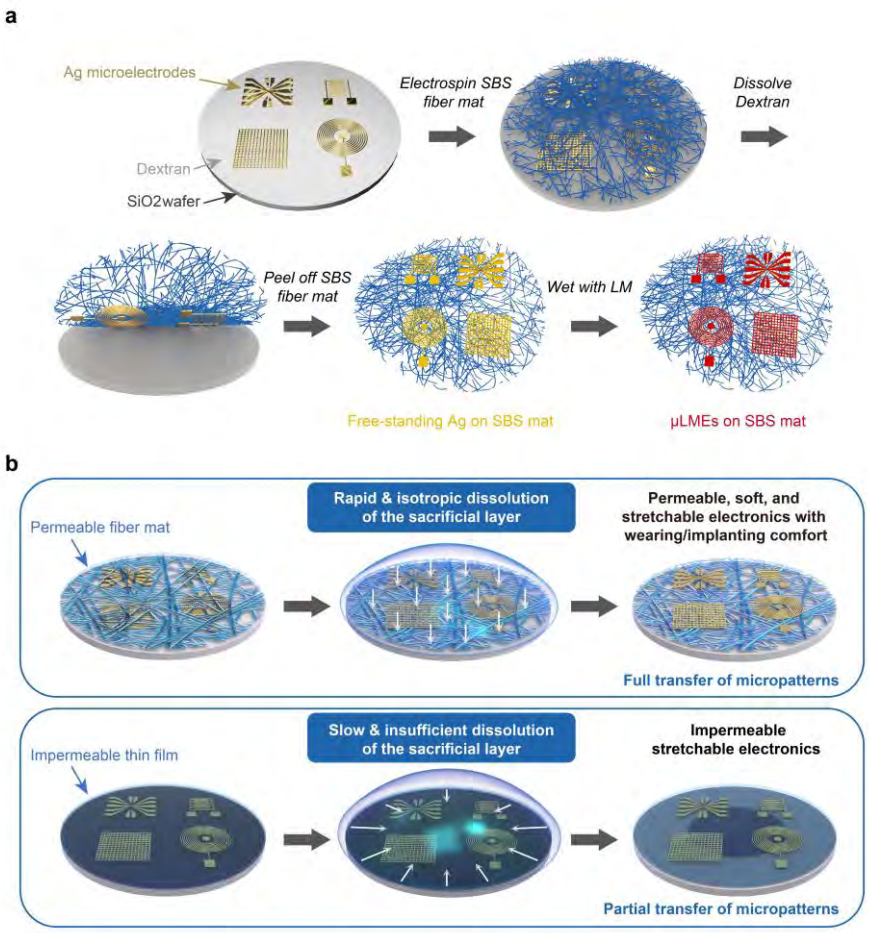

Figure 4.1 New route for permeable intrinsically stretchable electronics. a, Scalable fabrication of permeable intrinsically stretchable electronics using liquid metal microelectrodes (Plms) consisting of micropatterning of Ag electrodes on the sacrificial layer, additive electrospinning of poly(styrene-block-butadiene-block-styrene) (SBS) fiber mat, removal of the sacrificial layer, and selective wetting of LM. **b,** Schematic illustration of the routes for fabricating intrinsically stretchable electronics including on permeable substrates and impermeable substrates. Conventional transfer printing of stretchable electronics involves the etching of the sacrificial layer, of which the efficiency can be improved by orders using an impermeable stamp/receiver substrate. More importantly, the resulting intrinsically stretchable electronics on permeable substrates shows adequate air/moisture permeability for long-term wearing/implanting comfort.

Generally, the photolithography technique was adopted to fabricate micropatterns of

Ag on the sacrificial layer, followed with successful transfer facilitated by the permeable structure of the fiber mat (Figure 4.2). Firstly, the water-soluble sacrificial layer was spin-coated onto the clean carrier wafer with a very small thickness of ~10.2 nm (Figure 4.3a, b). With a weight fraction of 10 wt%, the obtained sacrificial layer showed relatively low roughness of ~0.675 nm (Figure 4.3c, d). After deposition of Ag film and lift-off process, micro-Ag patterns were obtained for subsequent selective wetting of LM.

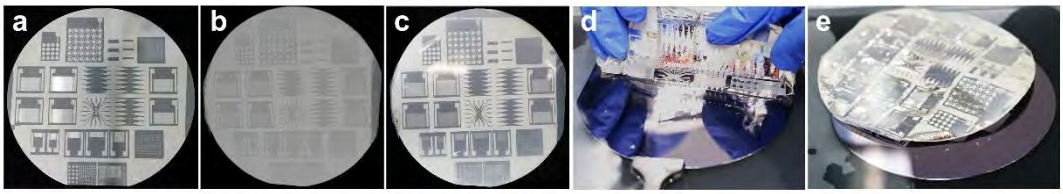

Figure 4.2 Digital images showing the process flow of wafer-scale patterning of permeable intrinsically stretchable electronics using liquid metal microelectrodes (Plms) facilitated by the permeable stamp/receiver substrate.

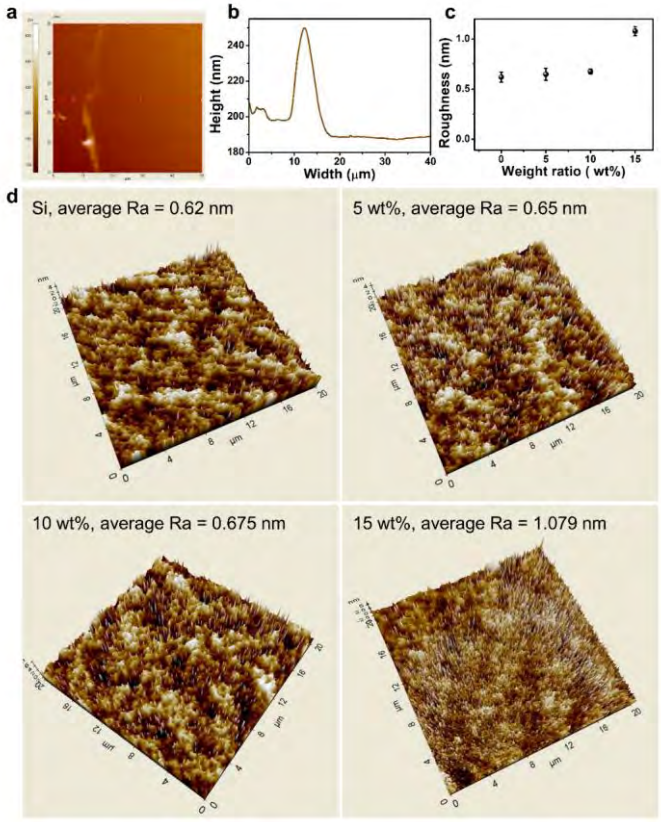

Figure 4.3 Morphology of the sacrificial layer coated on the wafer. a, Atomic Force Microscope (AFM) topographic image, and **b,** profile showing the thickness of the sacrificial layer. The polyimide (PI) tape was attached to the surface to identify the uncoated area. The white line denoted the boundary of the tape, in which the right region of the white line was the uncoated area. **c and d,** Surface roughness of the sacrificial layer prepared from various weight fractions of the solutions.

Next, we laminated the SBS mat as the substrate onto the Ag patterns via additive electrospinning. The SBS mat is both the stamp and the receiver substrate in this transfer process. With increasing electrospinning time from 20 minutes to 3h, the thickness of the SBS mat increased from 40 μm to 330 μm. The SBS mat was initially hydrophobic with a large wetting contact angle, seriously impeding the penetration of the etchant (water) and the final releasing of the water-soluble sacrificial layer. Notably, the SBS mat was rendered super-hydrophilic (contact angle ~0°) with fast penetration of the water after proper plasma treatment (Figure 4.4).

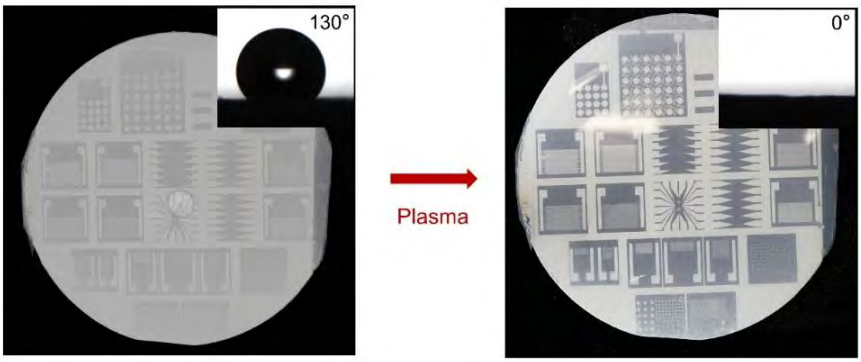

Figure 4.4 Contact angle of the water droplet on the SBS fiber mat before and after plasma treatment.

In this way, wafer-scale Ag micropatterns can be successfully transferred to the permeable stretchable SBS fiber mat (Figure 4.5a) and attached on skin (Figure 4.5b). Here the penetration speed was characterized with the absorption rate of the etchant (water) controlled via plasma treatment (Figure 4.5c). With the enhancement of the plasma treating duration from 0 to 20 minutes, the penetration speed increased from 0 to 9.12%/s. At this point, the successful rate of the pattern transfer reached over 95% (Figure 4.5d). Next, we fabricated LM micropatterns via selective wetting of Ag. Due to the high surface tension of LM, LM cannot spontaneously wet and spread onto the most polymeric surface with low surface energy. However, the wettability of LM could be improved via alloying with Ag layer with a thickness of around 300 nm (Figure 4.5e). Therefore, LM showed distinct wetting behavior on the patterned Ag area and the non-patterned SBS mat with a resolution of 2 μm (Figure 4.5f, g). We also demonstrated Plm-based electronic patch consisting of arbitrary polygons and electronic components with a density of 75,500 electrodes/cm^2.

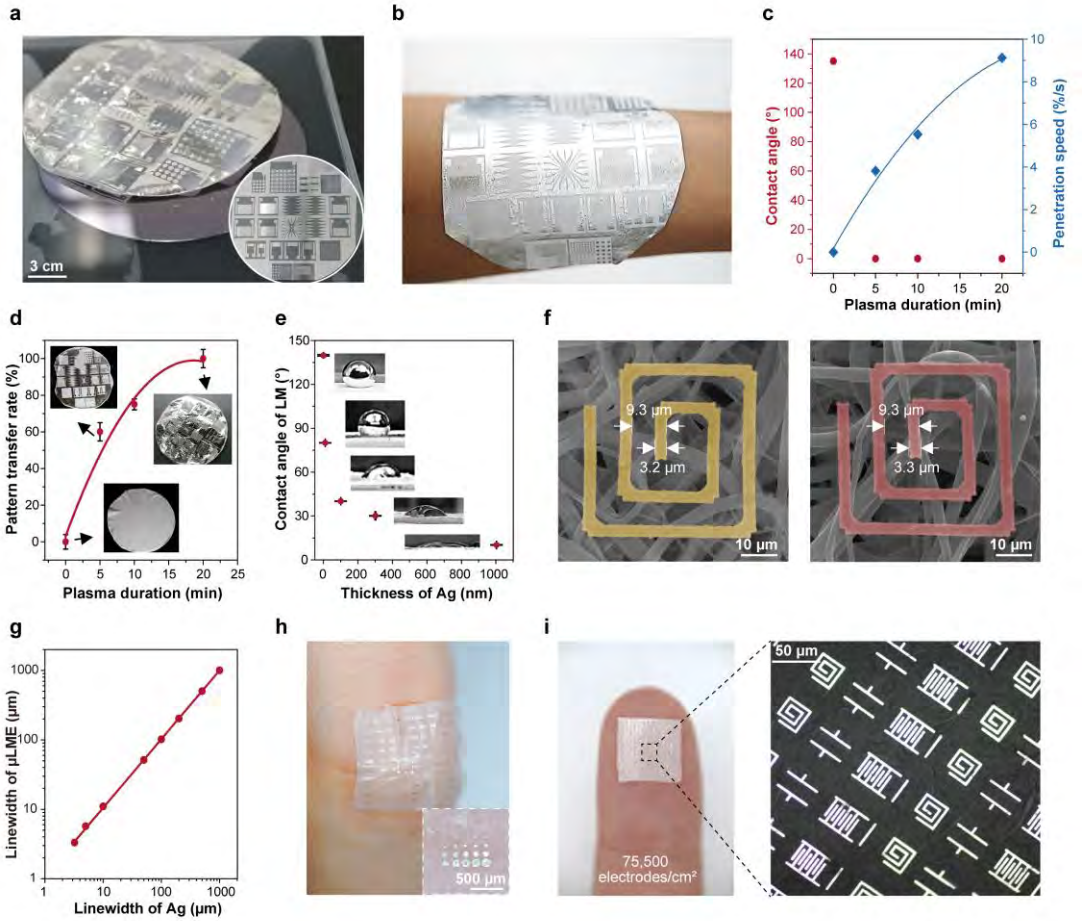

Figure 4.5 Structures of Plms. a, Digital images showing the transfer of Ag micropatterns from the wafer to the SBS fiber mat. The inset image shows the wafer-sized Ag micropatterns patterned on the wafer before transfer. **b,** Digital image of Plms attached on a human arm. **c,** Contact angle and penetration speed of the solvent to the sacrificial layer, and **d**, the pattern transfer success rate as a function of the plasma duration. **e,** Contact angle of LM on the transferred Ag layer as a function of the Ag thicknesses. **f,** Scanning electron microscope (SEM) images showing an electrode on the SBS fiber mat before and after the selective wetting with LM. **g,** Summary of the linewidths of Plms in correspondence to the original linewidths of Ag electrodes. **h and i,** Digital images of high-density Plms with a density as high as 75,500 electrodes/cm^2.

Here we adopted the impermeable spin-coated SBS film as the control substrate for the pattern transfer to explore the influence of permeable structure (Figure 4.6). After

plasma treatment, the water contact angle indeed reduced from 97° to 32°. However, after immersing the wafer in the water for 1 week, the Ag micropatterns still cannot be transferred due to the inadequate dissolution of the sacrificial layer and the strong adhesion between the SBS film and the underneath Ag micropatterns. In conclusions, permeable structure largely enhances the pattern transfer efficiency in terms of transfer speed and defect rate.

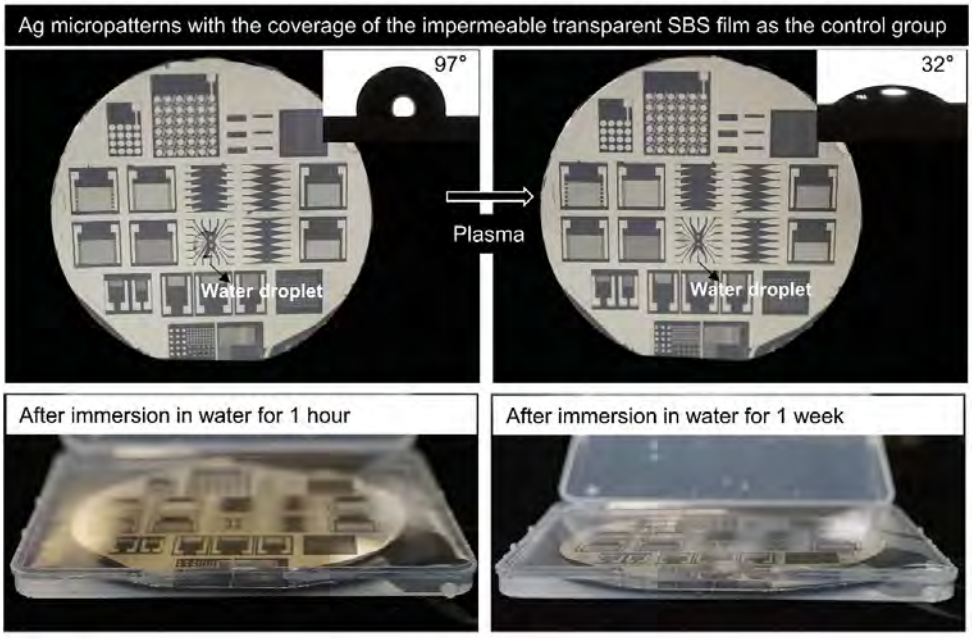

Figure 4.6 Digital images illustrating the low-efficiency transfer with the impermeable stamp/receiver substrate.

The selective wetting behavior of LM was explored with the elemental mapping of LM patterns with increasing loading amount of LM. The selectivity wetting of LM lies in the LM-lyophobic and LM-lyophilic properties of the SBS mat and the metal, respectively (Figure 4.7). The LM-lipophilicity of the Ag layer originates from the reactive alloying of LM-Ag and the formation of Intermetallic compounds (mainly In^4Ag^9, from the previous report). Firstly, when the wetting amount of LM is low (i.e. 0.2 mg/cm^2), patterned Ag electrodes were mainly selectively and reactively wetted by In. With an increasing adding amount of the LM, the alloy layer was subsequently

wetted by LM, showing the stronger signal of Ga and the weaker signal of Ag in the elemental mapping. The particle on the edge of the pattern was confirmed as the alloy of Ag-In from the elemental mapping image (Figure 4.8).

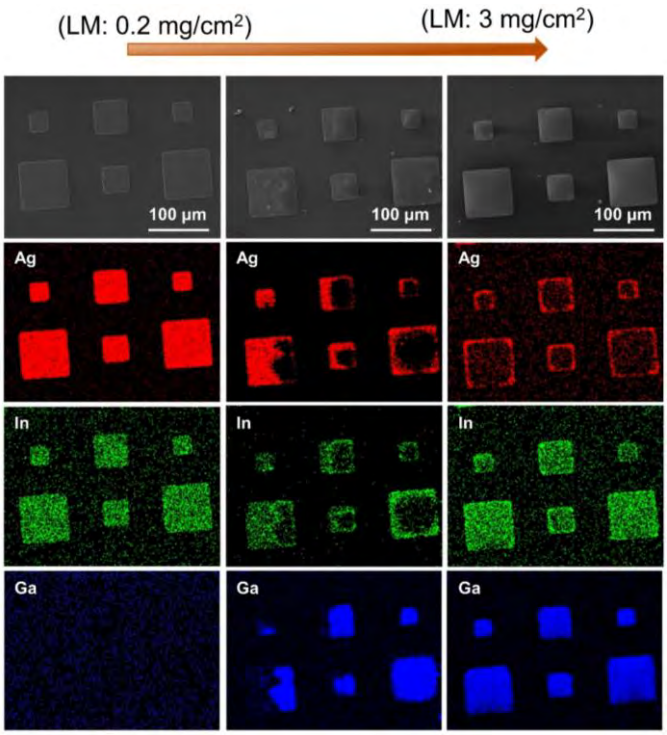

Figure 4.7 SEM and Elemental mapping images of LM-Ag patterns with an increasing amount of LM.

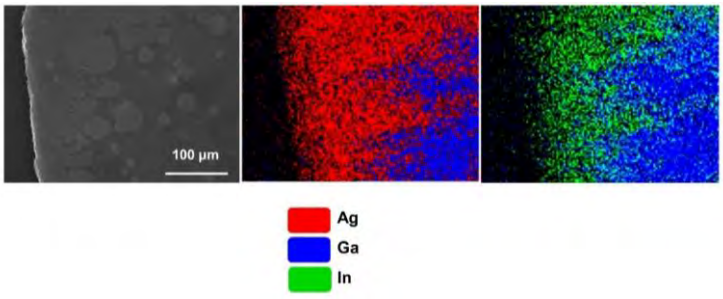

Figure 4.8 SEM and Elemental mapping images of the edge of LM-Ag patterns with In-Ag alloy particles.

Similarly, Plms were obtained via the selective wetting of LM on the fiber mat (Figure 4.9). In this way, we can obtain Plm with various shapes and dimensions including line

arrays, dot arrays, source/train electrodes, interdigital electrodes, and mesh electrodes, which could serve as the key component for various devices covering resistive sensors, micro-supercapacitors, interconnects, and antennas (Figure 4.10, 4.11).

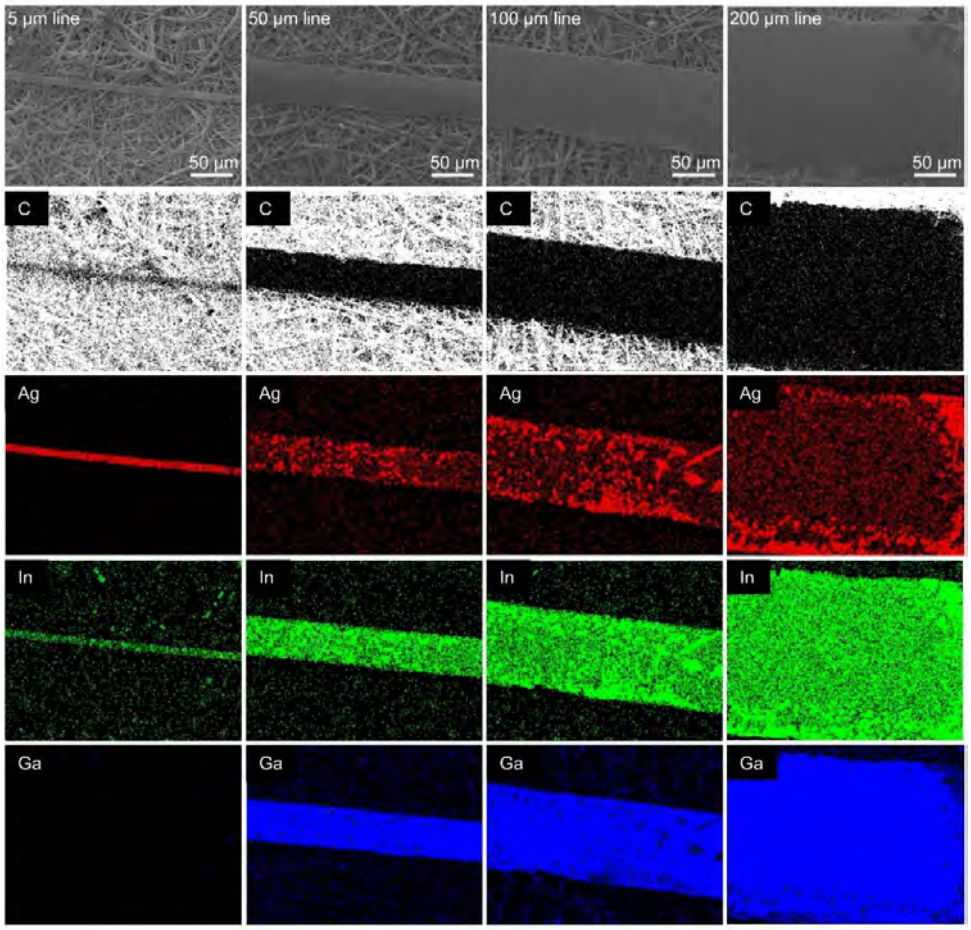

Figure 4.9 SEM images and elemental mapping images of Plms lines with various linewidths.

Furthermore, various dimensions and shapes of Plms were also obtained including line arrays, dot arrays, antenna, micro-supercapacitor, source/drain electrodes for transistors, and electrical contacts and interconnects.

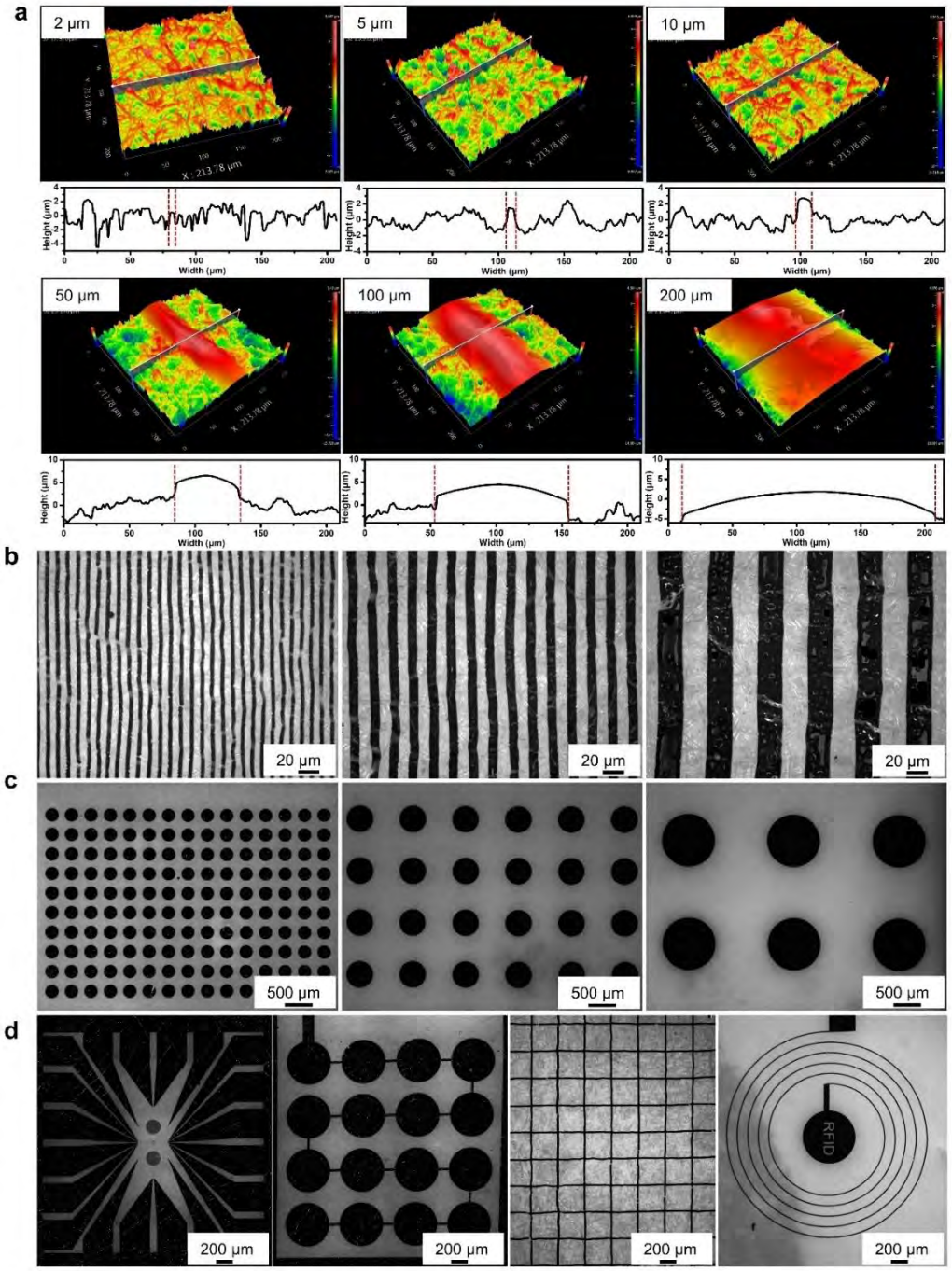

Figure 4.10 (a) Optical surface profiling images of Plms lines with various linewidths. (b) and (c) Line array and dot array of Plms with different dimensions. d, Optical images showing various Plm-based microelectrodes including a source-drain electrode, interconnect, mesh electrode, and antenna electrode.

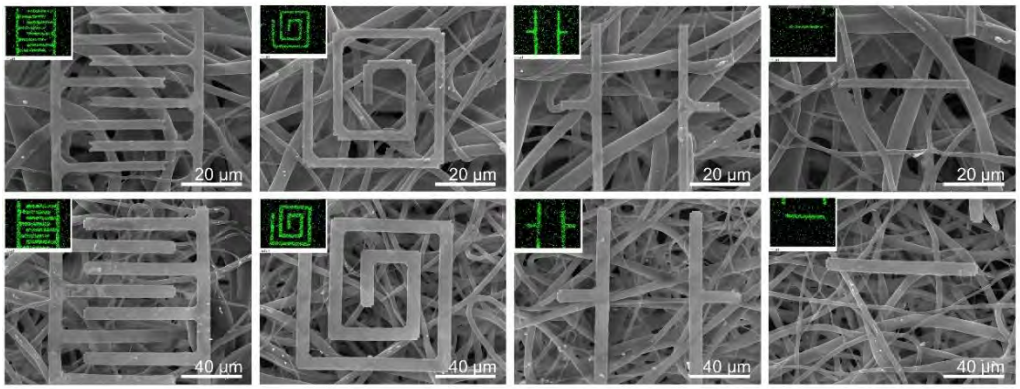

Figure 4.11 SEM images showing various electronic components using Plms including generators, inductors, capacitors, and resistors with the linewidth of 4 μm (upper) and 8 μm (lower). Inset images were the elemental mapping of element In, serving as the evidence for the selective wetting of LM.

It is worth noting that the patterning resolution can elevated to the submicron region by using the submicron mask. It also confirmed that the resolution of selective wetting of Plms can improved to the submicron region (Figure 4.12).

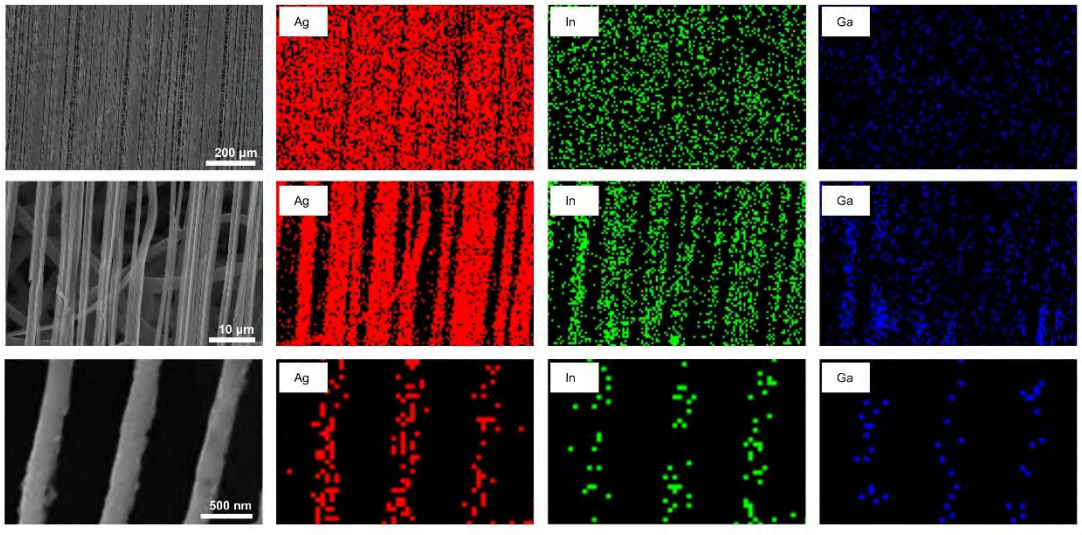

Figure 4.12 SEM image of large area sub-micron pattered LM lines on the SBS fiber mat, in which some LM lines were bundled together. The elemental mapping images confirmed the submicron resolution (down to 250 nm) of this transfer method and the selective wetting of LM.

4.3 Permeability, Stretchability, and Conductivity of Plms

Not only the porous SBS microfiber mat structure allowed fast and intact transfer but provided excellent permeability toward air, moisture, and liquid for long-term wearing comfort (Figure 4.13a) The air permeability of Plm (330 μm, ~78 mm/s) was much higher than many substrates for stretchable electronics including, Ecoflex, and polydimethylsiloxane (PDMS) (330 μm thick) (Figure 4.13b). Additionally, the moisture permeability of Plm (330 μm, ~835 $g/m^2 \cdot day$) was also much higher than that of PDMS and Ecoflex films (Figure 4.13c). Moreover, the permeability of Plm could be further enhanced with decreasing thickness to ~25 μm, of which the air permeability reached ~235 mm/s and the moisture permeability was ~990 $g/m^2 \cdot day$. Such excellent permeability of Plm could satisfy the insensible perspiration endow the wearing comfort for the human body. With increasing linewidth from 2 μm to 1000 μm, the average resistance values of LM line electrodes decreased from ~136 Ω to 0.0132 Ω, with an electrical conductivity ranging from 1.3 to 3.9×10^5 S/cm (Figure 4.13d) The resistance of the 5-μm-wide line remained relatively stable with a change of only 0.00585 at a strain of ~305%. With increasing linewidth (i.e. 10 and 50 μm), Plm could show electrical stability at higher tensile strains, with a resistance change of only ~2.3 at 1,000% strain (Figure 4.13e). Moreover, Plm with a linewidth of 10 and 50 μm showed robustness and durability during stretch-release cyclic tests. The resistance only changed by 1.03 (10 μm) after 100 cycles and 2.12 folds (50 μm) after 500cycles of stretch-release tests at a strain of 1,000% (Figure 4.13f). After the first stretching cycle, Plm formed the buckling structure, as reported previously. After the cycling test, the bucking structure was well maintained, indicating a stable and continuous conductive pathway of Plm (Figure 4.14).

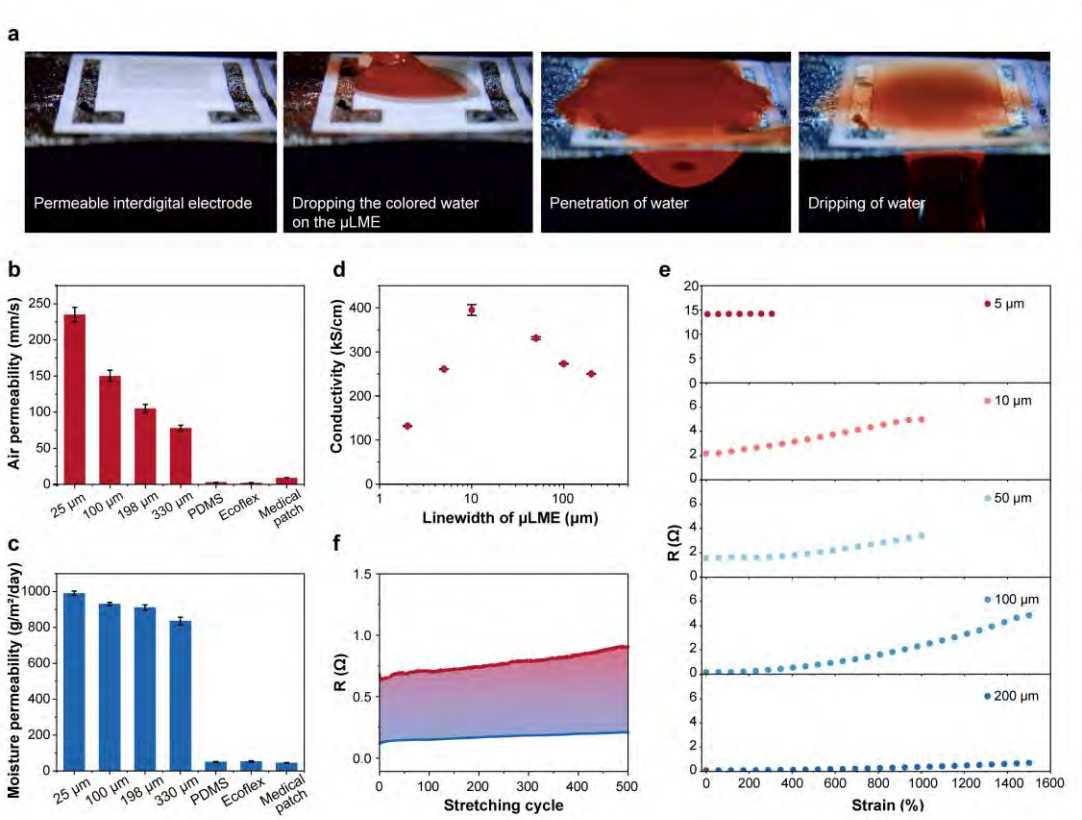

Figure 4.13 Permeability, conductivity, and stretchability of Plms. a, Digital images showing the penetration of one colored water droplet from one side of Plms to the other side. **b and c,** Air and moisture permeability of Plms on SBS mats with various thicknesses, as well as other common substrates for bioelectronics including PDMS, Ecoflex, and medical patch. **d,** Electrical conductivity of Plms of various linewidths. **e,** Resistance of Plms of various linewidths at different tensile strains. **f,** Cyclic electrical stability of Plms (linewidth 50 μm) under a large tensile strain of 1,000%.

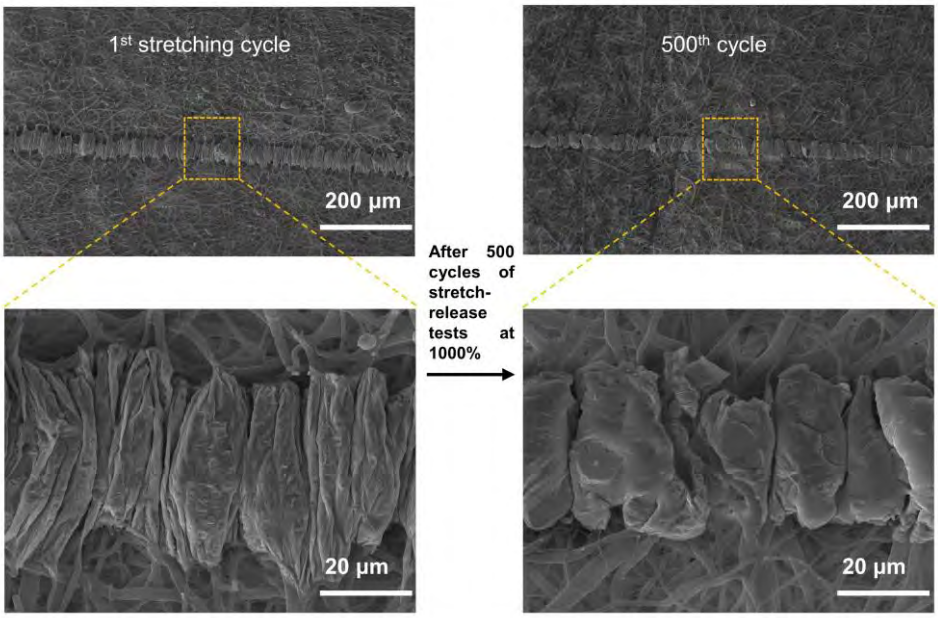

Figure 4.14 SEM images of Plms (50 μm) showing the morphological change of the buckling structure before and after the stretch-release cycling test at 1,000% strain.

4.4 Biocompatibility of Plms

Biocompatibility is crucial for wearable and on-skin applications. In this study, conductors in the shape of a serpentine structure were patterned onto various substrates, including SBS mat, PDMS, and Ecoflex, for biocompatibility tests. The PlmEs were found to have low cytotoxicity in the in vitro study using L-929 cells as the model cell (Figure 4.15a). Bright-field and fluorescent live/dead staining images showed a regular cell morphology and scarce dead cells in all groups except for the positive control group, which presented severe dead cells. Additionally, the PlmEs showed a high average cell viability of 98.74% in the quantification of the live/dead stained cells (Figure 4.15b). The absorption at 450 nm in the MTT assay (proportional to the number of cells) of all

groups was remarkably increased with incubation time from day 1 to day 3 with a similar trend indicating that there was no significant evidence of the toxicity of the PlmEs (Figure 4.15c). Further, in vivo animal experiments on rabbit skin showed that no obvious irritation was caused by PlmEs during the observation period (24, 48, and 72 hours), indicating that our PlmEs are skin-friendly (Figure 4.16).

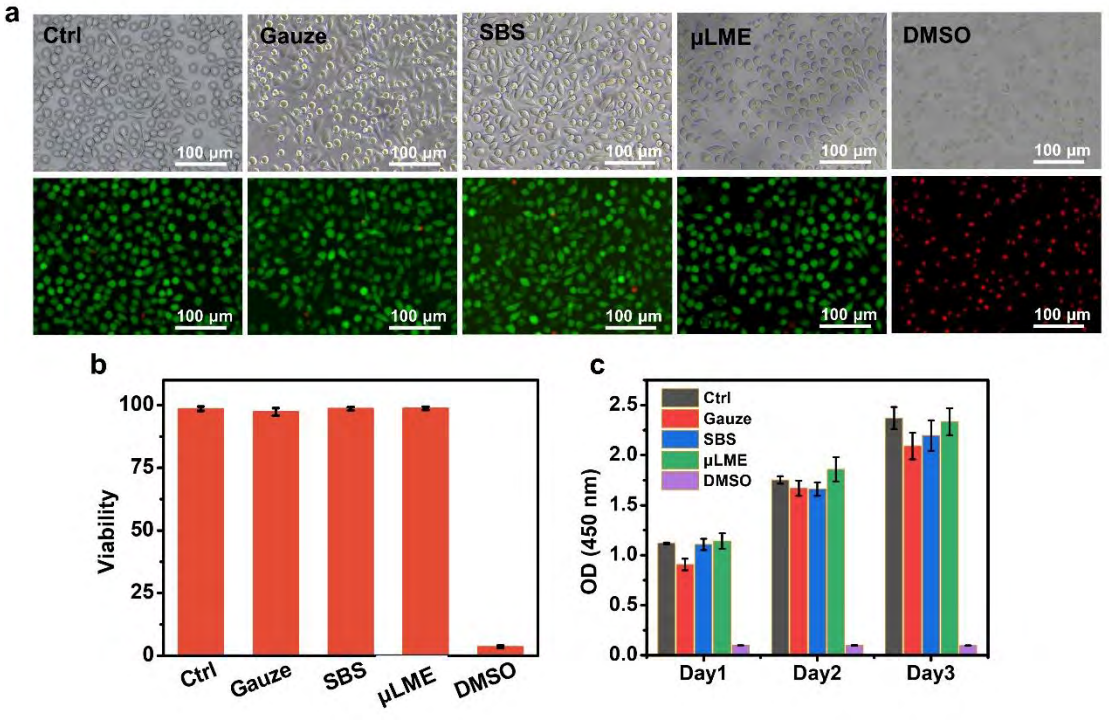

Figure 4.15 Cell biocompatibility of Plms. **a,** Bright-field and fluorescent images of cells cultured in the incubation medium with the control sample, absorbent gauze, SBS mat, Plm, and 20% DMSO. **b,** Quantification of L-929 cell viability in different incubation groups. **c,** Absorption at 450 nm in MTT assay of different incubation groups after 3 days of incubation. Bright-field and fluorescent live/dead staining images showed a regular cell morphology and scarce dead cells in all groups except for the DMSO group which presented severe dead cells. Additionally, Plm showed a high average cell viability of 98.74% in the quantification of the live/dead stained cells. The absorption at 450 nm in the MTT assay (proportional to the number of cells) of all groups was remarkably

increased with incubation time from day 1 to day 3 with a similar trend indicating that there was no significant evidence of the toxicity of the Plms.

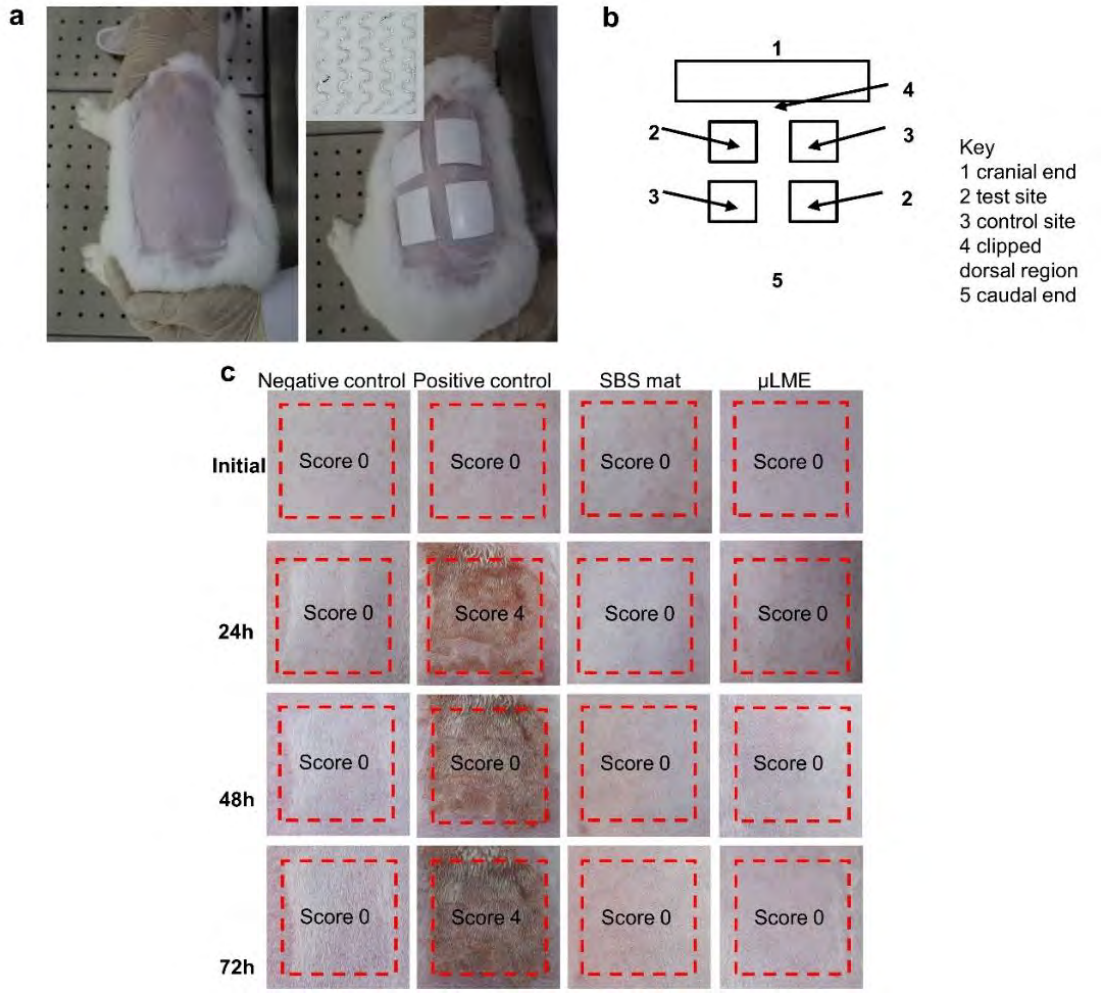

Figure 4.16 Animal test of Plms showing the on-skin biocompatibility. a and b, Digital image and schematic illustration showing the test sites of the on-skin attachment, respectively. The inset image was the tested Plms in the shape of the serpentine structure. **c,** Digital images of the rabbit skin after the attachment of various specimens during the 72-h observation.

In summary, we developed a new patterning, integration, and encapsulation technique for stretchable permeable electronics, enabling scalable fabrication of electronic

components with high resolution (2 μm), permeability (~990 g/m^2·day), density (75,500 devices per cm^2), stretchability (maximum strain ~1,000%), electrical conductance (18 Ω for the 5 μm line with the length of 10 mm), and electrical stability (resistance change of 2.3 at 1,000% strain). To date, Plm is the only strategy to confer stretchable electronics with high wearing comfort, integration density, biocompatibility, as well as electrical and mechanical properties (Table 5, 6). We envision that Plm will become a critical foundation for high-integration-density, multifunctional, microminiaturized wearable and implantable bioelectronics.

Table 5 Benchmark with other pattern techniques for permeable stretchable electrodes in terms of resolution, density, pros, and cons.

Patterning method	Resolution (μm)	Density (/cm^2)	Advantages	Disadvantages	Ref.
Inkjet printing	50~3,000	2.85~0.48	Relatively high resolution, cost-effectiveness, and low material consumption.	Limited printing speed, nozzle clogging, coffee-ring issues.	[27,53,54,75]
Screen/stencil printing	1,000~10,000	0.05~0.2	Industrially scalable capability, low resistance of thick ink.	Time-consuming screen plate preparation.	[6,56,58,76]
Laser engraving and cutting	100~10,000	0.16~0.67	High efficiency, versatility, cost-effectiveness.	Limited material selection	[32,68,69]
Pen-writing	300~10,000	0.2~0.44	Cost-effectiveness, easy handling.	Limited ink selections, only for simple structures.	[61–63,77]
PVD with mask	300~2,000	4~11	High-quality deposited thin film	Relatively low resolution.	[65,78]
Spray printing	200~10,000	0.08~1.27	Rapid processing	Poor repeatability, and low material consumption.	[59,60,79]
Textile method	100~10,000	0.4~2	Compatibility with the production of textiles.	Limited by the conductive fiber/yarn selections.	[66,67,80]
Transfer printing followed by pore drilling	110	0.15	High resolution, complex patterns, compatibility with conventional IC technology.	Multi-step fabrication, low transfer rate when the resolution is high.	[81]

Transfer printing facilitated by permeable structure	**0.25~2**	**75,500**	**Fast transfer, high resolution, complex patterns, compatibility with IC technology.**	**Multi-step fabrication.**	**This work**

Table 6 Benchmark with current patterning techniques for LM using lithography-enabled, injection, additive, and subtractive processes.

Patterning Methods	**Strategy**	**Resolution (width) (μm)**	**Spacing (μm)**	**Thickness (μm)**	**Permeability**	**Biocompatibility**	**Ref.**
Lithography-enabled process	**Transfer printing facilitated by permeable structure**	**0.25~2**	**0.5~2**	**1.3~25**	**Permeable**	**Biocompatible**	**This work**
	Hybrid lithography	0.18	1	0.3~1	Not permeable	N.A.	[100]
	Soft lithography (imprinting and reverse stamping)	2	1~2	<2	Not permeable	N.A.	[101,102]
	Additive stamping	500	500	~1.5	Not permeable	N.A.	[103]
	Metal stencil film	200	100	6~30	Not permeable	N.A.	[104]
	Microfabricated metal stencil film	10	10	~2	Not permeable	N.A.	[105]
	Photo Lithography	20	40	~10	Not permeable	N.A.	[106]
Injection	Fluidic injection	70	>70	70	Not permeable	N.A.	[107]
	Vacuum filling	~10	N.A.	>50	Not permeable	N.A.	[108]
Additive process	2D printing	~100	N.A.	>50	Not permeable	N.A.	[109]
	3D printing	~100	N.A.	~100	Not permeable	N.A.	[110]
	2D printing and transfer	2	N.A.	>80	Not permeable	N.A.	[111]
Subtractive process	Laser	4.5	100	<1	Not permeable	N.A.	[112]
	Electrochemical reduction	~1,000	N.A.	~120	Not permeable	N.A.	[113]

Chapter 5: High-density Plms-based Bioelectronics for Neural Electrophysiological Interface

5.1 Introduction

With this wafer-based patterning technique, soft and stretchable microelectrodes were well prepared on permeable substrates with much high resolution and device density than those with conventional technologies on permeable substrates. Therefore, a soft, biocompatible, and stretchable bioelectronics system with both high spatiotemporal resolution and chronic wearing/implanting comfort can be potentially achieved using this technique. As a proof of concept, here we demonstrated the implantable micro-electrocorticography (μ-ECoG) arrays for the recording and stimulation of the soft, curved, and sophisticated neural electrophysiological interface.

5.2 Design of Plm-based Electrocorticography (ECoG) Array

Major cortical subdomains of the rat consisting of motor, somatosensory, visual, and retrosplenial cortices were covered with Plm (Figure 5.1a). The diameter of the circular electrode array was 500 μm with a minimum linewidth of 40 μm and a channel count of 36 channels (Figure 5.1b).

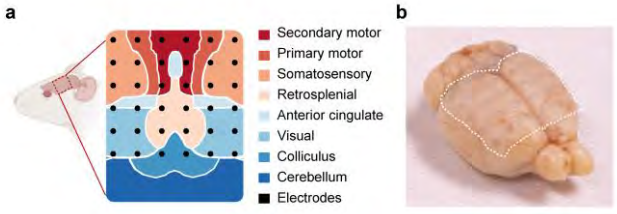

Figure 5.1 High-density Plms-based bioelectronics for the neural electrophysiological interface. a, Schematic illustration showing the application of Plms-based electrocorticography

(ECoG) array and the recorded cortical subdomains. **b,** Digital images of Plm ECoG electrode array (thickness 25 μm) with conformal attachment onto the soft, curved, and sophisticated cerebral cortex. The dashed line showed the boundary of the Plm array.

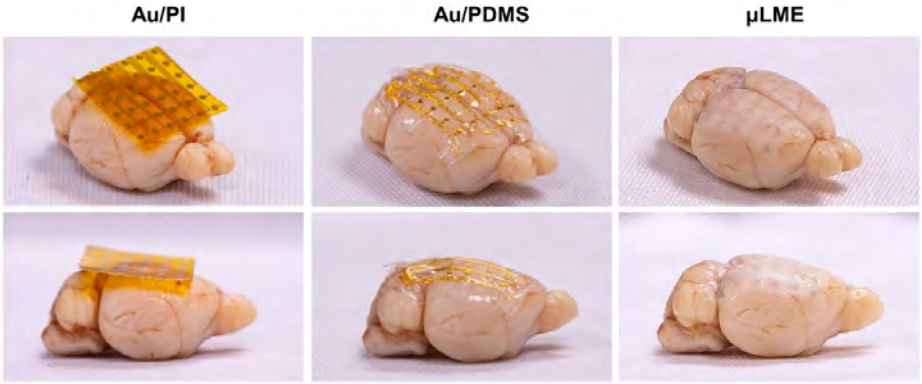

Figure 5.2 Digital images showing attachment of various electrodes (thickness 25 μm) on the cortex of a mouse including Au/polyimide (PI) film, Au/PDMS, and Plm.

This conformal attachment to the cortical surface results from the similarity in mechanical compliance between Plm and the brain tissue (Figure 5.2).

Compared with present materials for ECoG electrodes (e.g., Polyimide (PI), Parylene C, and Silicone), Plm showed much lower low Young's modulus values (Figure 5.3). Such mechanical compliance of Plm can potentially suppress immunogenetic scar formation and mitigate the risks of infection, thus benefiting chronic stability and comfort.

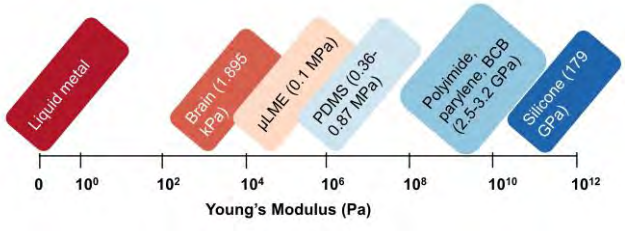

Figure 5.3 Comparison of Young's modulus of Plms with reported materials for ECoG bioelectrodes.

5.3 *In vitro* Characterizations Plm-based ECoG Array

To verify the possibility of Plm for neural electrophysiological recording and stimulation, *in vitro* impedance characterization was firstly carried out. The electrochemical impedance of Plm in phosphate-buffered saline (PBS) was slightly larger than that of the Au/PI electrode in the frequency ranges from 1 Hz to several thousand Hz with the same dimension (Figure 5.4). However, Plm can maintain relatively electrochemically stable with the maximum tensile strain of up to 500% while Au/PI electrode revealed a dramatic increase in the impedance at a strain of 30% (Figure 5.5) resulting from the mechanical failure of electrodes (Figure 5.6).

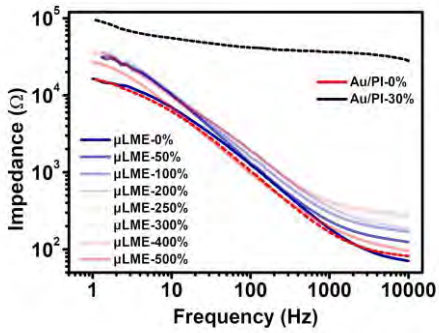

Figure 5.4 *in vitro* electrochemical impedance spectroscopy (EIS) characterizations of Plms and Au/PI electrodes under different strains.

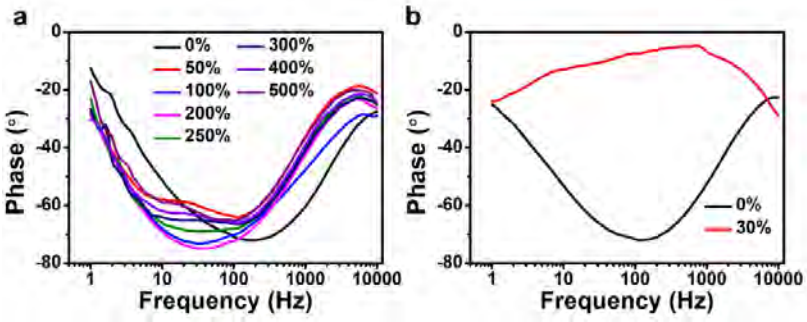

Figure 5.5 Electrochemical impedance spectroscopy (EIS) measurements of Plms and Au/PI films under various strains. a, Phase angle curves of Plms under various strains. b, Phase angle curves of Au/PI films under various strains.

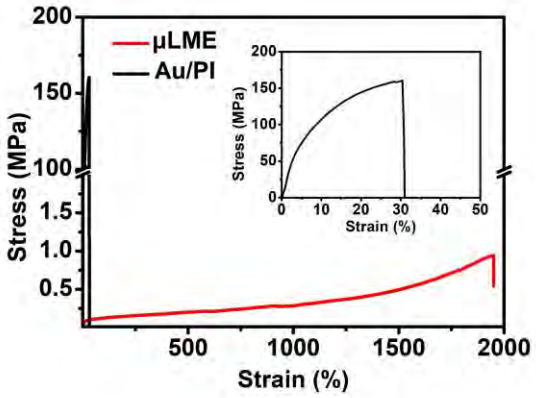

Figure 5.6 Stress-strain curves of Plm and Au/PI film. Au/PI film can only sustain a maximum strain of ~30% while Plm possessed a maximum strain of ~2000%.

In addition, from the multi-channel test, the 36-channel μ-ECoG electrode array showed low device variation (Figure 5.7).

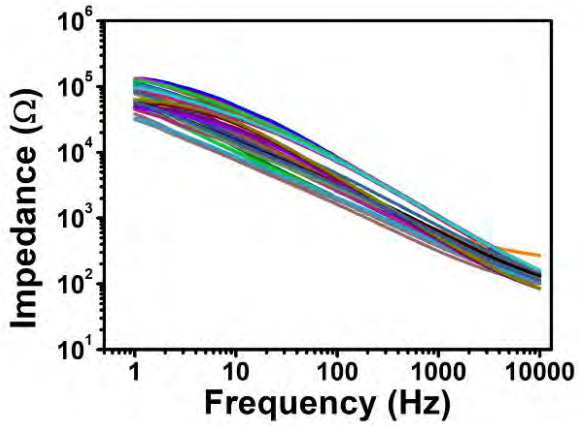

Figure 5.7 EIS measurements of multi-channel Plm array as a function of the frequency ranging from 1 to 10,000 Hz.

5.4 *In vivo* Neural Signal Recording Using Plms

For *in vivo* recording of the cortical activity, we recorded the neural signal of the rat during sleeping (Figure 5.8).

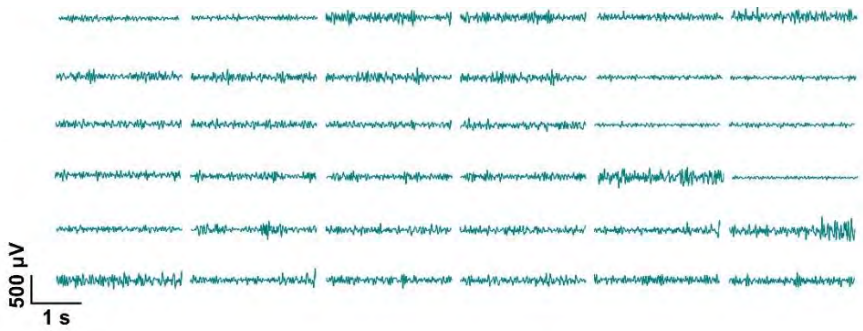

Figure 5.8 Neural signal recording through Plms at the sleep state.

From the power spectrum after band-pass filler, the rat mainly showed nonrapid eye movement (NREM) sleep, with the existence of low-frequency delta waves lower than 4 Hz and theta waves ranging from 4 to 8 Hz (Figure 5.9).

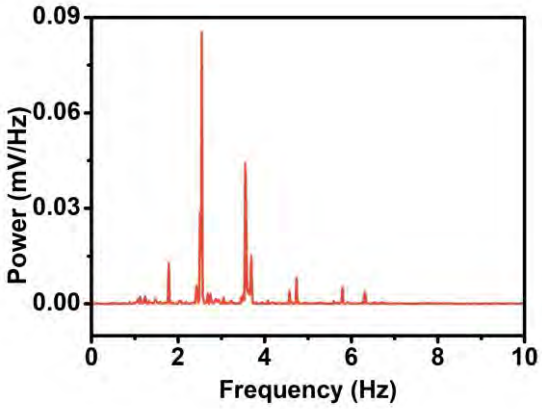

Figure 5.9 Power spectrum analysis of *in vivo* neural signals at the sleep state of a living rat.

To verify the capacity of Plm for recording region-specific cortical activity, we electrically stimulated the forelimbs and examined somatosensory evoked potentials (SEPs) in the cortex. Frequencies ranging from 1 Hz to 9 Hz (Figure 5.10a) and pulse voltages ranging from 1 V to 6V (Figure 5.10b) were selected for the electrical stimulation, to which the SEPs responded correspondingly.

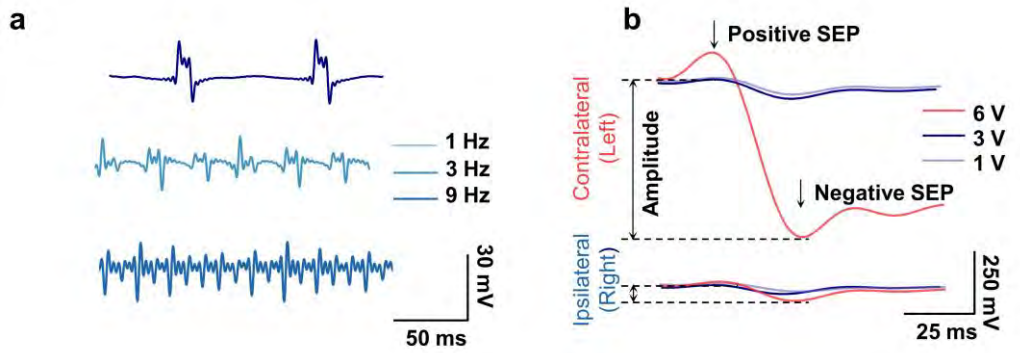

Figure 5.10 a, Somatosensory evoked potentials (SEPs) recorded with Plms under electrical stimulations with pulse voltage of various frequencies. **b**, Comparison of SEPs in the contralateral and ipsilateral somatosensory cortices under electrical stimulations with pulse voltage of various intensities.

The amplitude of the neural signal displayed an intensity-dependent manner, from 15 to 107 mV in the positive SEP and 44 to 630 mV in the negative SEP with increasing pulse voltage. Notably, the neural signals in the contralateral hemisphere were much stronger than those in the ipsilateral hemisphere since these electrical stimulations were applied on the right forelimb (Figure 5.10b). Additionally, from the spectrogram of the stimulated contralateral somatosensory cortex, reproducible rhythm (7-14 Hz) of the electrocorticographic signal increased predominantly resulting from the electronic stimulation (Figure 5.11)

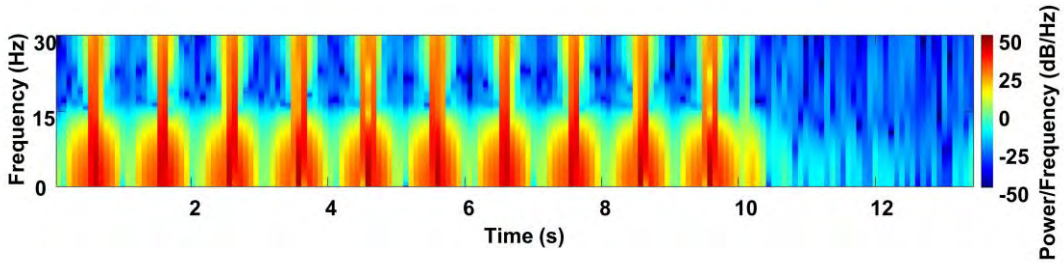

Figure 5.11 Spectrogram of the signals of the contralateral somatosensory cortex under ten continuous electrical stimulations with the intensity of 6V and the frequency of 1 Hz.

The spatiotemporal properties of SEP were explored (Figure 5.12). In response to forelimb stimulations, positive SEP peaks at approximately 20 ms on the stimulated hemispheres after stimulation onsets were detected from the somatosensory cortex in the stimulations of both forelimbs, whereas the counterpart hemispheres lacked these responses. In contrast, negative SEP peaks emerged in both hemispheres, representing a cognitive response to the stimulus. Other cortical areas such as motor (primary and secondary) cortexes, and visual cortex also showed weaker SEP signals compared with the somatosensory cortex.

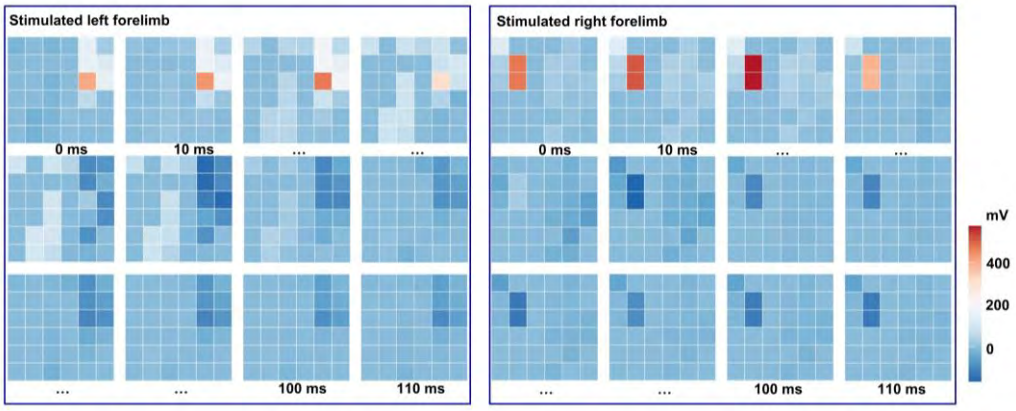

Figure 5.12 Spatiotemporal properties for the Plm array in response to the electrical stimulations of left and right forelimbs.

5.5 Chronic Biocompatibility of Plms for Biointerfaces

Further, we explored the chronic biocompatibility and long-term implanting comfort of Plm for implants in the brain and skeletal muscle. After implantation of the ECoG electrodes, no damage or inflammatory responses were found in the tissues and cells from the immunohistological analysis of the brain slice (Figure 5.13a). Additionally, after implantation for one month, no significant difference was found between Plm group and control group, while PI and PDMS showed an increasing amount of the 1bar1 and the soma size of the microglia (Figure 5.13b-d).

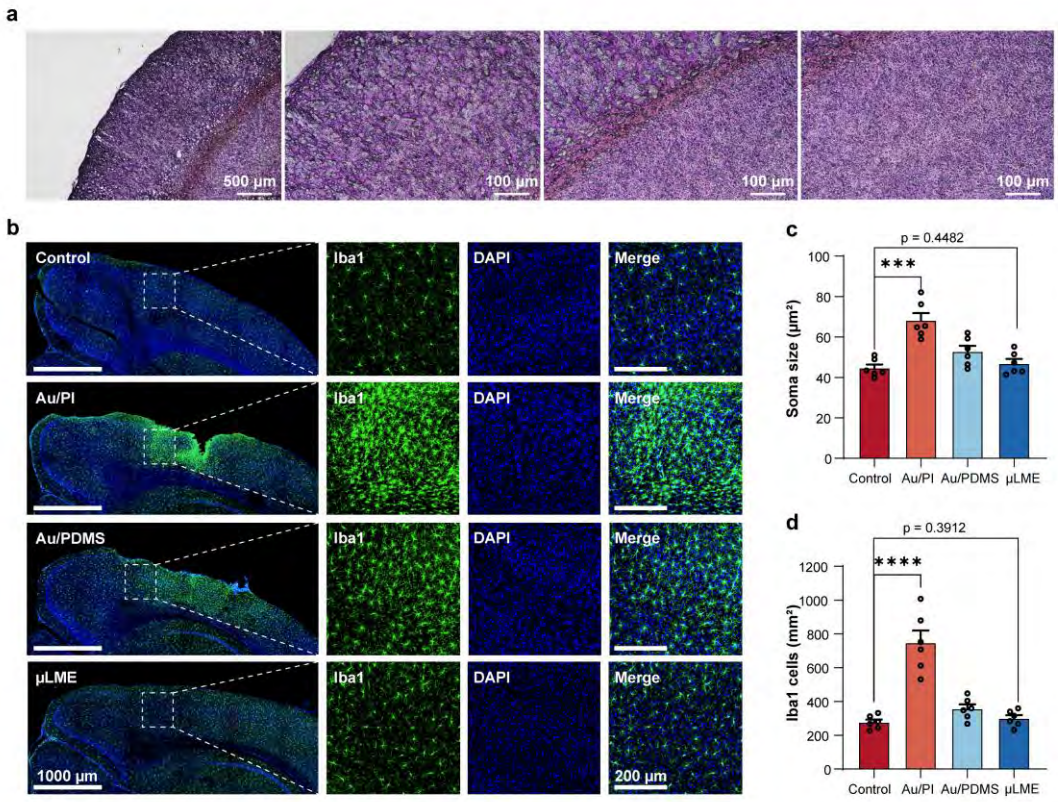

Figure 5.13 Chronic biocompatibility of Plms for chronic neural implants. a, Immunohistological analysis of a stained brain slice after implantation for 2 hours. **b,** Immunohistochemistry staining of the microglia (Ibar1, green), and nuclei (DAPI, blue) at 2 weeks post-implantation of the control, Au/PI electrodes, Au/PDMS electrodes, and Plm electrodes. **c,** Statistical analysis of the microglia soma size (n = 6). **d,** Statistical analysis of the total microglia cells intensity (n = 6).

Similarly, Plm showed good biocompatibility after implanting in the skeletal muscle of rats for one week (Figure 5.14). This mainly results from the soft and biocompatible electrode material with reduced size from the fabrication technique. In conclusion, the utility of the integration technique for soft, stretchable, permeable, and biocompatible Plm enabled a comfortable and high-density/channel-count neural-machine interface, which cannot be achieved with previous fabrication techniques.

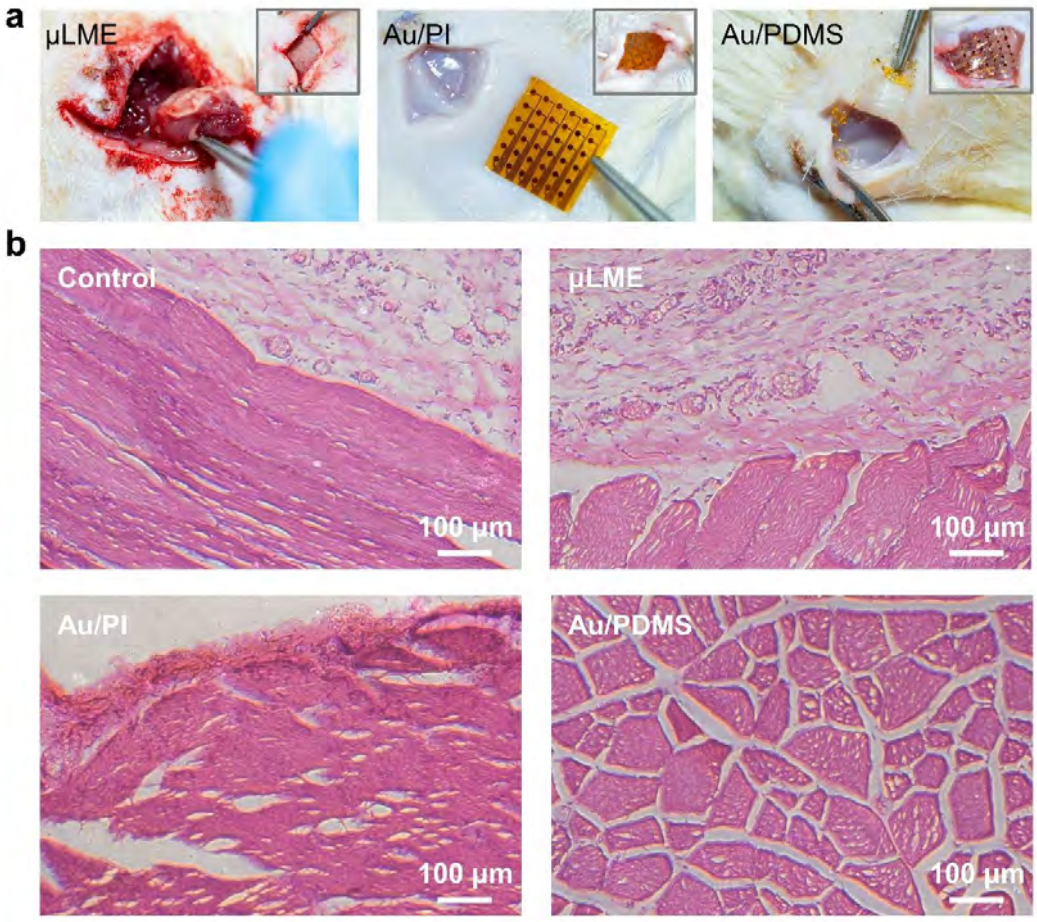

Figure 5.14 Chronic biocompatibility of Plms for implants in skeletal muscle. a, Digital images of taking out the electrodes including Plm, Au/PI, and Au/PDMS after implantation for one week. Inset images showing the insertion of electrodes on the surface of skeletal muscle. **b,** Hematoxylin and eosin (H&E) staining images of the skeletal muscle after implantation of various electrodes.

After the examination of the implanted devices, no fibrotic tissues were found. Meanwhile, we did not find the existence of LM, which may be degraded or dissolved by the biofluidic.

Figure 5.15 Digital images showing the devices after implantation.

In summary, we developed high-density neural electrophysiological interface using Plms-based microelectrodes. With a wafer-scale patterning technique on the supersoft and superelastic fiber mat, Plms-based microelectrodes enabled advanced neural bioelectronics with high temporal-spatial resolution in neural signal recording and interventions. Due to the highly soft, permeable, and stretchable characteristics, Plms-based ECoG devices showed superior chronic biocompatibility with an implantation duration of over eight months (Table 7).

Table 7 Summary of recent flexible/stretchable ECoG devices.

Electrode materials	Subject	Active or passive	Linewidth (μm)	Density (/cm^2)	Implant duration for study	Ref.
Au/PI	Rat	Passive	50	177	N.A.	[114]
Au/PI	Rat	Passive	20	266	42 days	[115]
Pt/Au	NHP	Passive	70	155	N.A.	[116]
Pt/PI	NHP	Passive	15	12	137 days	[117]
Pt/ Parylene C	Rat	Passive	60	400	N.A.	[118]
Pt disks	Human	Passive	500	1	N.A.	[119]
Si/Pt/PI	Cat	Active	50	400	N.A.	[120]
PEDOT:PSS/ Parylene C	Rat	Passive	10	6,400	10 days	[121]
Si/Pt/PI	Rat	Active	50	1,600	N.A.	[122]
Pt	Human	Passive	1,000	11	N.A.	[123]
Pt microwires	Human	Passive	100	100	N.A.	[124]
PEDOT:PSS/ parylene	Human	Passive	10	28	N.A.	[125]
Au/Parylene	NHP	Passive	25	2	N.A.	[126]
Si/Au/PI	Rat	Active	15	625	435 days	[98]

Micro LM	**Rat**	**Passive**	**40**	**100**	**>130 days**	**This work**

Chapter 6: Permeable Stretchable Hydrogel Bioelectronics Using LM

6.1 Introduction

Bioelectronics interfacing with the human body is the basis of the rapidly growing field of physiological monitoring[44,127,128], imaging[129,130], modulations[131,132], neural science[133,134], and tissue repairing[135]. Remarkable progress has been achieved in the development of compatible, effective, and stable interfaces between biology and electronics overcoming the intrinsic dissimilarities between soft and living biological tissues and rigid, dry, and synthetic electronic systems[16,136–138].

Hydrogels, crosslinked polymer networks infiltrated with water, showing great promise in bridging of the human body and machines with exceptional advantages including tissue-like softness and wetness, permeability of small molecules (water, ions, and nutrient molecules), biocompatibility, and adhesion[139]. However, the development of hydrogel bioelectronics is still limited by several challenges. Firstly, the electrical conductivities (10^{-5} to 10^{-1} S/cm) of most hydrogel electrodes[140,141] are inadequate for digital circuits and advanced bioelectronic devices[142]. To enhance the electrical properties, conductive fillers (metals, conducting polymers, and carbon-based materials)[143–146] or direct coating/printing[147–149] of conductive films were typically introduced. Notably, gallium-based liquid metal (LM) shows superior softness and stretchability as liquid, high electrical conductivity, and biocompatibility for the fabrication of highly electrically conductive hydrogel bioelectronics.

However, when patterned at small feature sizes (e.g., 10 μm), to combine high mechanical robustness with good electrical conduction of the supersoft and wet hydrogel-based electrodes is very challenging. Therefore, the patternable resolution is

very low ranging from mm to cm. This is far from meeting the demand for advanced bioelectronics aiming for mapping and intervention with a high spatial and temporal resolution, which typically requires a patterning resolution down to a few micrometers.

Here we develop wafer-scale micropatterned gallium-based LM hydrogel bioelectrodes (PlmHs) with high stretchability, electrical conductivity, and patterning resolution up to 5 μm. The PlmH show tissue-like softness, outstanding electrical conductance when stretched up to 1,500% strain, high transparency with a linewidth of 5 μm. Highlighting its versatility, we use this platform to demonstrate multi-channel implantable hydrogel optogenetic bioelectronics with high temporal-spatial resolution for neural-machine interface.

6.2 Fabrication of Plm Hydrogel (PlmH) Bioelectrodes

Figure 6.1a shows a schematic illustration of the fabrication process of wafer-scale transparent micro-LM bioelectronics, which consists of four main steps: 1) photolithography of Ag on a SiO_2 wafer pre-modified with a thin layer of water-soluble dextran; 2) generation of surface bonding via oxygen plasma treatment, 3) in situ gelation of a hydrogel receiver substrate onto the Ag micropatterns; 4) transfer of the Ag micropatterns from the SiO_2 wafer onto the hydrogel, and 5) selective wetting of LM on the Ag-cover areas to generate transparent micro-LM on hydrogel.

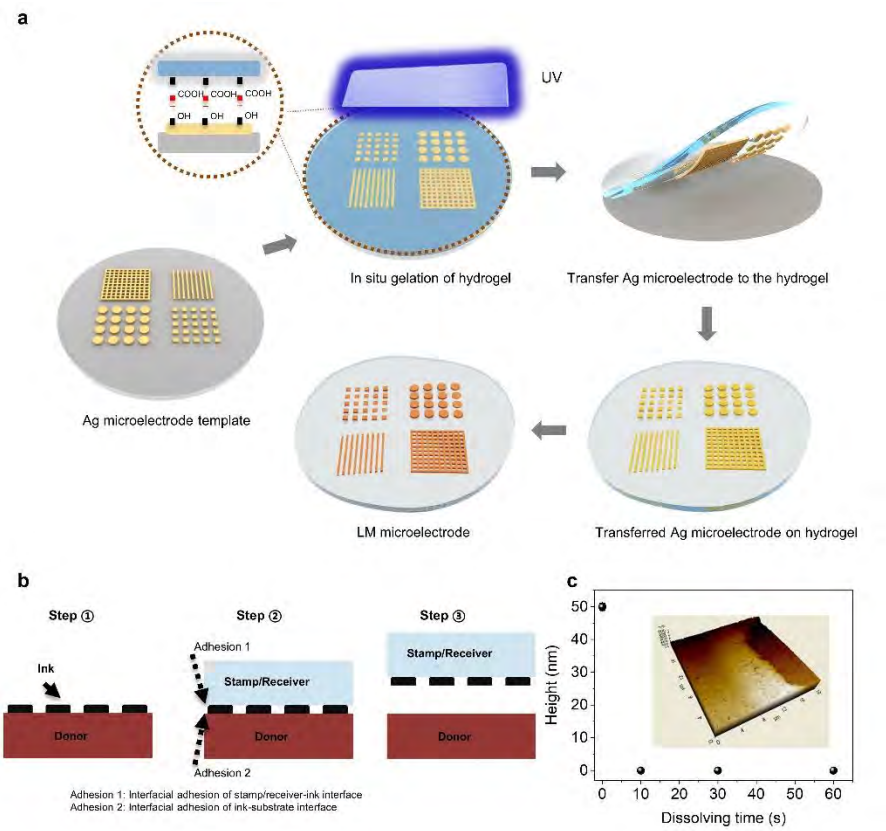

Figure 6.1 Fabrication process of micropatterned LM hydrogel bioelectrodes (PlmHs). a, Schematic illustration of the fabrication process of PlmHs, which consists of five main steps: 1) photolithography of Ag on a SiO_2 wafer pre-modified with a thin layer of water-soluble dextran; 2) generation of surface bonding via oxygen plasma treatment, 3) in situ gelation of a hydrogel receiver substrate onto the Ag micropatterns; 4) transfer of the Ag micropatterns from the SiO_2 wafer onto the hydrogel, and 5) selective wetting of LM on the Ag-cover areas to generate PlmHs. **b,** Schematic illustration of the modulation of the interfacial adhesion during the transfer process. Transfer printing process consists of retrieval/pick-up of inks from the donor substrate and printing/delivery of inks onto the receiver substrates. **c,** Atomic force microscopic topographic images showing the dissolving rate of the sacrificial layer (dextran).

Here we adjust two interfacial adhesions during the gelation process. Generally, the transfer printing process consists of retrieval/pick-up of inks from the donor substrate and printing/delivery of inks onto the receiver substrate (Step 1 and step 3 in Figure

6.1b). First of all, with increasing of the gelation duration, the hydrogel stamp is brought into more contact with the ordered and releasable micropatterned inks on the SiO_2 wafer (donor substrate) through the bonding between the hydrophilic groups (e.g., hydroxy and carboxyl groups). Meanwhile, the water-soluble sacrificial layer was gradually dissolved by the precursor solution for the hydrogel. Moreover, the as-formed hydrogel film is water-permeable, therefore even with the coverage of hydrogel on top of the micropatterns, the sacrificial layer can be continuously dissolved by the water. The dissolving rate of the sacrificial layer was ~ 1nm/s for a 10 nm thick coating (Figure 6.1c). Therefore, during gelation, the adhesion of the stamp/ink interface is stronger than the ink/substrate interface during retrieval while be weaker when printing. After peeling off the hydrogel from the wafer, the micropatterns were selectively wetted with LM (eutectic gallium indium (EGaIn) alloy) to generate the micro-LM hydrogel bioelectrodes.

As a proof of concept, polyacrylic acid (PAA) hydrogel was adopted owning to the hydrophilic surface bonding, high adhesion, good biocompatibility and mechanical properties. The preparation of the hydrogel receiver substrate was shown in Figure 6.2a. To maintain a relatively stable water content, organic solvent (glycerine) was introduced here to form the organohydrogel. Here the crosslinking density of PAA enhanced with increasing crosslinking duration, in which the sol-gel transition was found at around 58 s (Figure 6.2b). Meanwhile, the interfacial adhesion strength enhanced with increasing gelation duration, which triggered the transfer of the patterns (Figure 6.2c). At this point, the pattern transfer rate reached around 95% (Figure 6.2d).

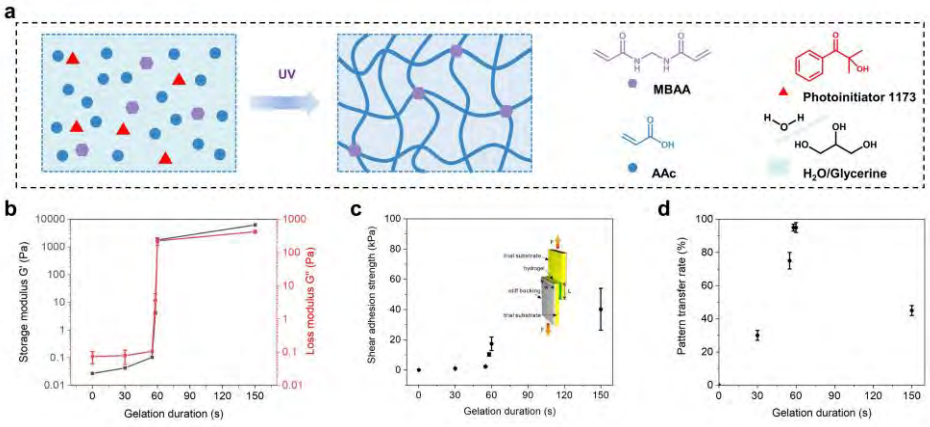

Figure 6.2 Patterning features of PlmHs. a, Schematic illustration of the preparation of the polyacrylic acid (PAA) organohydrogel substrate for micropattern transfer. **b,** Storage modulus and loss modulus of PAA as the function of gelation duration. **c, d,** Interfacial adhesion of the transfer stamp (PAA) and pattern transfer rate of Ag microelectrodes as the function of the gelation duration. Inset image is the schematic illustration of the testing setup for the interfacial sheer adhesion strength.

AA was fully crosslinked and polymerized into PAA upon UV exposure for 150 s, which was confirmed by the chemical shift of the proton nuclear magnetic resonance (NMR) spectroscopy, as well as the strengthened signal of C=O stretching, and the weakened signal of C=C stretching in the Raman spectra (Figure 6.3).

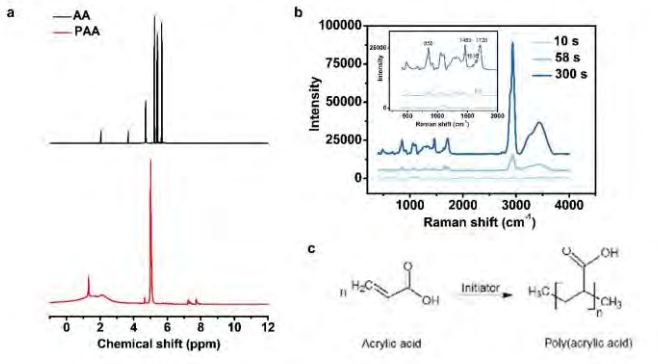

Figure 6.3 Characterization of PAA hydrogels. a, Proton nuclear magnetic resonance (NMR) spectroscopy of AA and PAA. **b,** Raman spectra of PAA as a function of crosslinking duration. **c**, Schematic representation of the synthesis of PAA.

After transfer of Ag micropatterns onto the organohydrogel and selective wetting of LM, transparent LM micropatterns with a typical resolution of ~9 μm in a shape of mesh structure were obtained (Figure 6.4). The transferred LM microelectrodes show no difference in the resolution. With increasing storage period, the linewidth can be further narrowed down to 8.9 μm due to the moderate dehydration of the organohydrogel substrate.

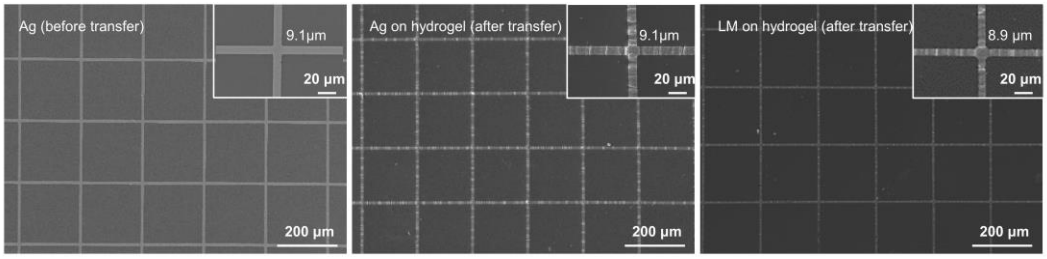

Figure 6.4 SEM images showing an transparent mesh electrode on the polyimide (PI, before transfer), on the PAA (after transfer) before and after the selective wetting with LM.

With this linewidth, the mass loading of LM ranged from to 0 to 4.09 mg/cm^2 during the selective wetting process (Figure 6.5).

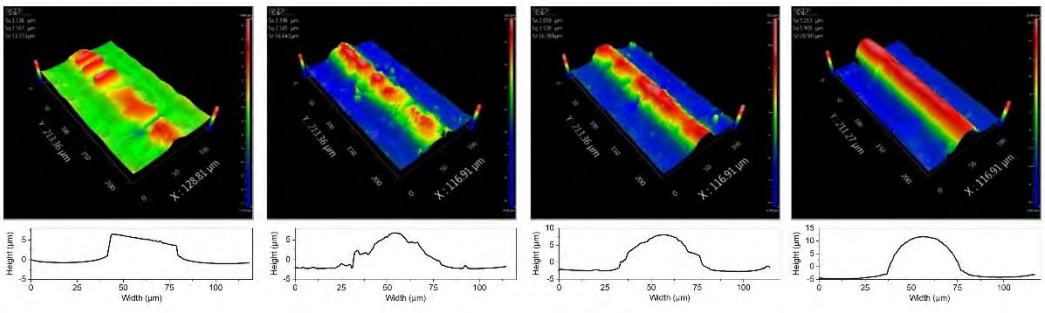

Figure 6.5 Optical surface profiling images of PlmH with various mass loading of LM.

In this way, PlmHs with various dimensions including ranging from 5 μm to 1,000 μm and a wide variety of shapes, including dots, lines, meshes, and analog circuits were obtained.

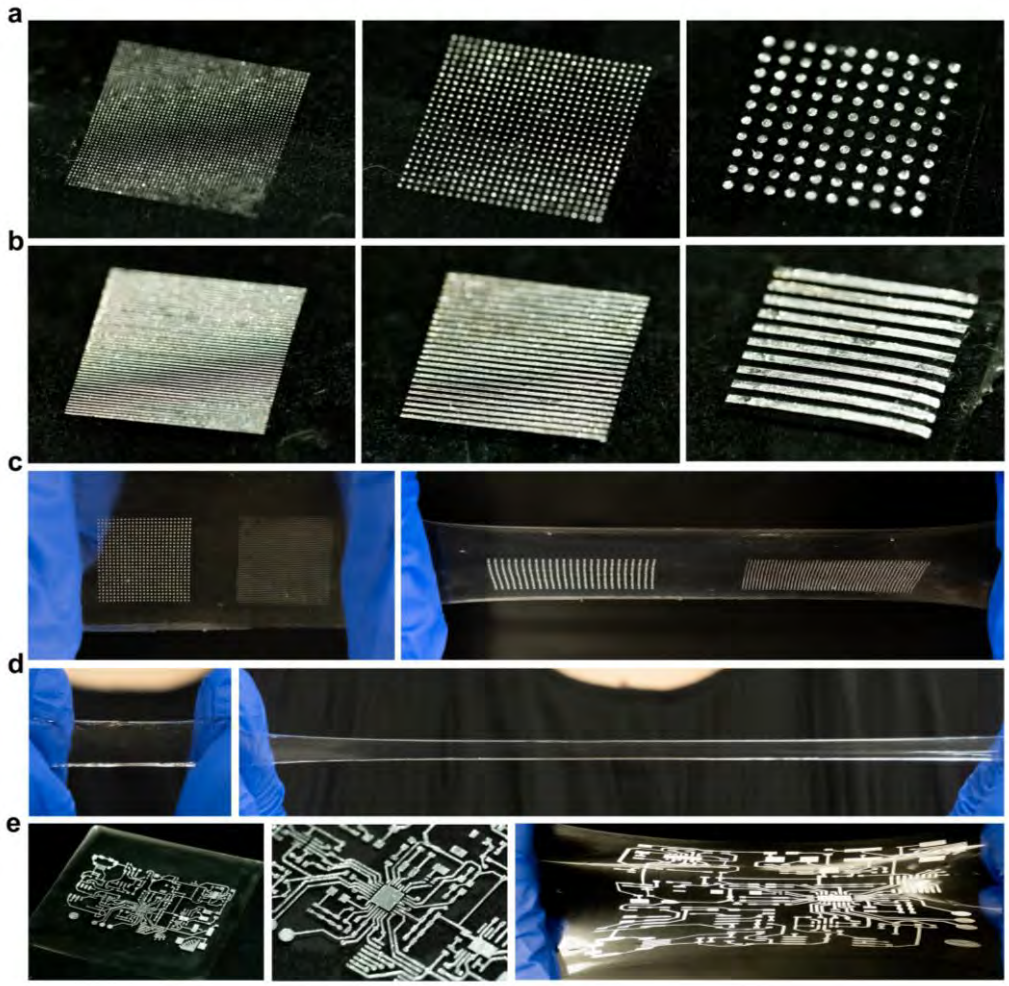

Figure 6.6 Various LM micropatterns on hydrogels including (a) dot arrays, (b) and (c) line arrays, (d) transparent micro LM mesh, and (e) LM microcircuits.

Figure 6.7 Digital images of PlmH for the analog circuit board with power management functions.

6.3 Conductivity, Stretchability, and Transparency of PlmHs

PlmHs possess outstanding stretchability and softness. With increasing of the weight fraction of precursor solution (AA in water/ glycerin), the maximum strain (Figure 6.8a) and Young's modulus (Figure 6.8b) of the hydrogel elevated. To obtain a soft and stretchable substrate, 30 wt% was selected with a maximum strain of ~ 2,500% and low modulus of ~ 25 kPa. In addition, the transmittance of PlmHs enhanced with the reducing patterning linewidth, with an average transparency of ~89.8% at the wavelength of 550 nm (Figure 6.8c). Additionally, the electrical conductivity enhanced from with the increasing LM mass loading, with a maximum electrical conductivity of 31,968 S/cm (Figure 6.8d). During the stretch-release tests, PlmHs showed good electrical stability. For highly conductive PlmHs (50 μm linewidth and gap, average transmittance 53.7 at 550 nm), the electrical resistance changed only~3.8 at 1,000% strain (Figure 6.8e). For highly transparent PlmHs (10 μm linewidth and gap, average transmittance 79.8 at 550 nm), the electrical resistance changed only~2.1 at 1,000% strain (Figure 6.8f).

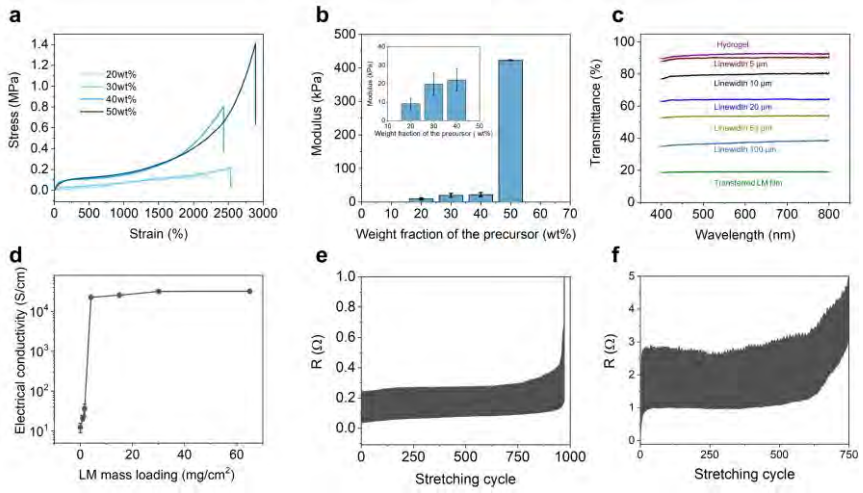

Figure 6.8 Conductivity, stretchability, and transparency of PlmHs. a, b, Stress-strain curves and Young's modulus of PlmHs prepared with various weight ratios of PAA in the precursor

solutions. **c,** Transmittance of as the function of wavelength of mesh PlmHs with various patterning resolution ranging from 5 μm to 100 μm (linewidths and gaps). **d,** Electrical conductivity of PlmHs with various mass loading of LM. **e, f,** Electrical resistance of PlmHs (50 μm linewidth and gap, average transmittance 53.7 at 550 nm), and PlmHs (10 μm linewidth and gap, average transmittance 79.8 at 550 nm) during the stretch-release tests from 0% strain to 1,000% strain.

6.4 PlmH-based Implantable Bioelectronics for Neural Interface with Optogenetics Mapping

With this wafer-based patterning technique, transparent, soft, and stretchable PlmHs were well prepared on hydrogel surface with much high resolution than those with conventional technologies. We demonstrated the electrocorticography (ECoG) arrays for the recording and intervention of the soft, curved, and sophisticated neural electrophysiological interface using optogenetics. Multilayer ECoG device was developed consisting of PAA substrate, 32-channel micro LM electrodes and trances, polyacrylamide (PAM) hydrogel packaging layer preventing signal crosstalk, LM ECoG electrodes (Figure 6.9a). Major cortical subdomains of the rat consisting of motor, somatosensory, visual, and retrosplenial cortices were covered with PlmHs (Figure 6.9b). The diameter of the circular electrode array was 600 μm with a minimum linewidth of 200 μm and a channel count of 32 channels (Figure 6.9c). Due to the similarity in mechanical compliance (25 kPa) with brain tissue, PlmHs was conformally attached to the cortical surface.

To verify the possibility of PlmHs for neural electrophysiological recording and stimulation, *in vitro* impedance characterization was firstly carried out. PlmHs with increasing linewidth showed low electrochemical impedance in phosphate-buffered saline (PBS) (Figure 6.9d). In addition, from the multi-channel test, the 32-channel PlmH electrode array showed low device variation (Figure 6.9e).

For *in vivo* recording of the cortical activity, we recorded the neural signal of the rat during sleeping. To verify the capacity of PlmHs for recording region-specific cortical activity with optogenetics mapping functions, we stimulated the cortex using 473-nm blue light and examined somatosensory evoked potentials (SEPs) in the cortex. Notably, the neural signals with light stimulus were twice stronger than those without light stimulus (Figure 6.9f). Furthermore, the spatiotemporal properties of SEP were explored (Figure 6.9g). In response to light stimulations, SEP peaks at ~80 ms after the stimulation onsets. Moreover, rhythms (0-50 Hz) of the electrocorticographic signals were observed reproducibly throughout the continuous light stimulations (Figure 6.9h).

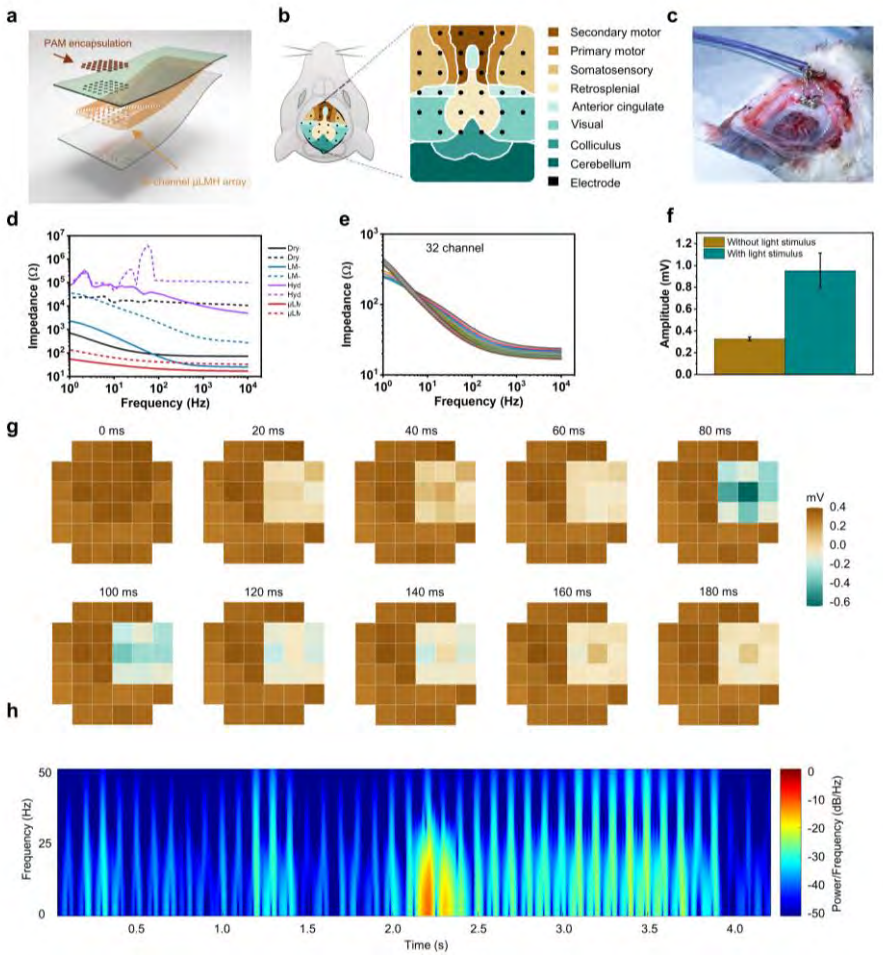

Figure 6.9 High-density PlmHs-based hydrogel bioelectronics for the neural electrophysiological interface with optogenetic mapping functions. a, Schematic illustration of

the multilayer and multichannel PlmHs-based electrocorticography (ECoG) array for hydrogel bioelectronics b, c, Schematic illustration and digital image showing the recorded cortical subdomains using PlmHs for optogenetics, respectively. d, *in vitro* electrochemical impedance spectroscopy (EIS) characterizations of PlmHs, dry Ag electrodes, and hydrogel electrodes. e, Multi-channel EIS characterizations of PlmHs. f, Amplitude of the ECoG signal of a living rat at the sleep state (without light stimulus), and with light stimulus (473 nm blue light). g, Spatiotemporal properties for the PlmH array in response to the light stimulations (473 nm blue light). h, Spectrogram of the ECoG signals of the contralateral somatosensory cortex under continuous light stimulations (473 nm blue light).

Chapter 7: Wireless Permeable Three-dimensional Integrated Electronic Skins

7.1 Introduction

Three-dimensional (3D) integrated electronics provide high-integration-density and multifunctionality, and have been generally adopted in the current printed circuit boards (PCBs) industry[150,151]. Incorporating commercial electronics such as unobtrusive, inexpensive, high-performance chips with stretchable printed circuits can potentially provide clinical-quality health monitoring capabilities for continuous use[44], beyond the confines of traditional hospitals or laboratories.

Soft and stretchable integrated electronics with continuous physiological monitoring and intervention are essential for a broad range of emerging fields, including intensive care[152], close-loop diagnosis, and treatment[153], rehabilitations[154], and virtual reality/augmented reality[91]. Encouraging progress has been made in developing novel materials and architectures for stretchable functional circuits integrating components such as transistors, sensors, and logics[16,136,155]. However, creating stretchable circuits with these ICs with a robust interface between each circuit element is very challenging. Imparting stretchability to various functional components and integration at the system level is generally regarded as a key challenge in achieving fully integrated electronic systems with global stretchability[156]. To solve this issue, three general approaches have been established including buckling engineering[157,158], oxidation engineering[159,160], and intrinsic-stretchability engineering[9,10].

Moreover, permeability is of paramount significance during continuous use[85]. Very recently, permeable stretchable electronic materials and devices that are fabricated on porous elastomeric substrates can offer high stretchability, supersoftness (skin

compatibility), and permeability to air, moisture, and even liquid[6,7,27,65,68]. Such types of electronic skins can endow chronic (long-term) wearing comfort and biocompatibility in comparison to conventional impermeable thin-film counterparts[8,161]. Nevertheless, current permeable skin electronics still cannot achieve signal processing, computation, and communication on a system level owing to the lack of a full integration with existing rigid components.

To fill this research gap, here we propose 3D integrated wireless permeable electronic skins (WPE-skins) with skin-like softness, adequate permeability for daily wearing, reliable electrical functions, and potentially serving as portable, fully-integrated, and comfortable wearables in long-term applications. Liquid-phase metal (LM, e.g. gallium-based alloys) is selected for the electrode materials due to its unlimited stretchability and low modulus as a liquid, high electrical conductivity, and biocompatibility[26,162,163]. The key technology is to engineer a reliable 3D integrated electrical interface with microchips on the multilayered porous fiber mat using the micropatterned oxidation-engineered LM. Stiff LM serves as the pads, and soft fluidic LM as the connections between pad and pins (bonding sites) enabling both in-plane and interlayer electrical connection with components, ensuring electrically stable connections both in-plane and out-of-plane even under a large strain. We demonstrate two types of wireless permeable microelectronic systems using Bluetooth circuits (communication distance: 15 m), and near-field communication (NFC, working distance: 12 mm) technology. The WPE-skins are skin-attachable, stretchable, and wirelessly communicated with a mobile device capable of electrophysiological (EP) data acquisition, filtering, amplification, RF transmission, and EP intervention.

7.2 Design of Wireless Permeable 3D Integrated Electronic Skin (WPE-skins)

Using previously developed micropatterning technique for permeable and stretchable LM microelectrodes (Figure 7.1a), we fabricated the permeable stretchable multilayered circuits. After additive electrospinning of the paste mask layer and stencil printing of the LM pads and paste, we placed the commercial electric components with a robust and stable electrical interface to achieve the electrical functions. Finally, a permeable stretchable encapsulation superstrate was fabricated on top of the multilayered circuits via electrospinning of the SBS fiber mat. Figure 7.1b showed the structure and functions of each layer in WPE-skins.

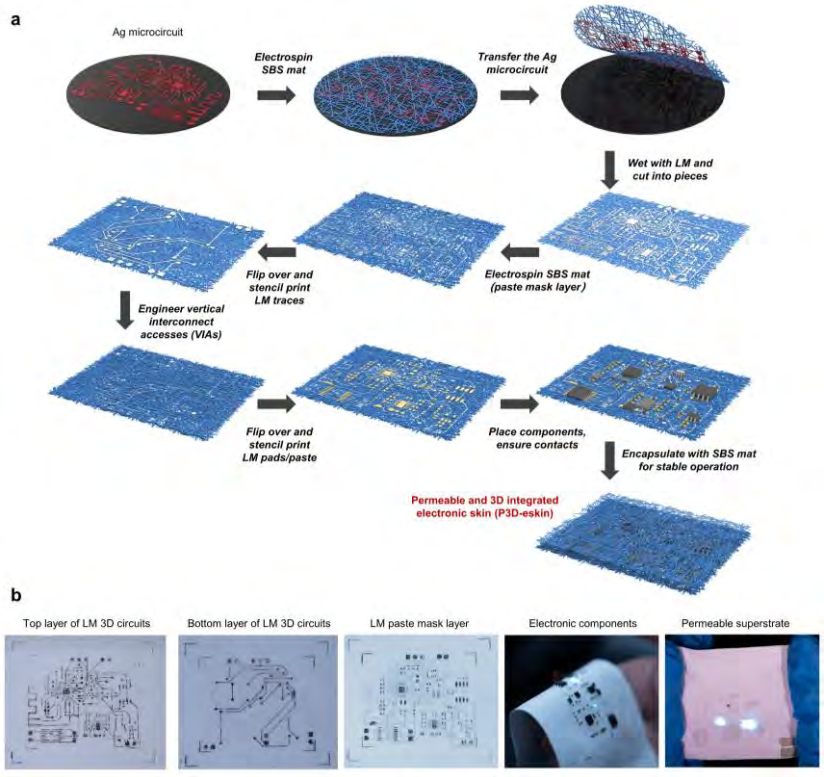

Figure 7.1 a, Schematic illustration showing the process flow of layer-by-layer fabrication of wireless permeable three-dimensional integrated electronic skins (WPE-skin). **b,** Digital images showing the structure and functions of each layer in WPE-skin.

As shown in Figure 7.2a, the 3D integration of WPE-skins typically involves the four-layer architecture consisting of 1) the bottom layer and 2) the top layer of the permeable stretchable 3D LM circuits, in which permeable and stretchable LM microelectrodes serve as antenna, traces, pads, paste, contacts, and vertical interconnect accesses (VIAs) for the 3D LM circuits, 3) paste mask layer reliably interfacing with the electronic components using oxidation-engineered LM microelectrodes consisting of oxidized LM (oLM) pads and paste (Figure 7.2b) and fluidic LM bonding sites (inset image in Figure 7.2c), and 4) permeable stretchable encapsulation layer using electrospun fiber mat. The encapsulation is air and moisture permeable, however, it is waterproof with a large water contact angle. Therefore, the LM circuits can be well protected with stable electrical functions.

The device is built layer by layer, and the components include a microcontroller unit (MCU), oscillator, multiplexer (MUX), current mirror, digital-analog-convertor (DAC), operational amplifier (OP-AMP), high voltage module (HV, 20V), and low dropout regulator (LDO, 3.3 V). Moreover, WPE-skins are highly flexible (Figure 7.2d) and stretchable, with a stable electrical output even under a large strain (Figure 7.2e). Such a 3D integration of wireless permeable microelectronic systems can not only achieve electronic functions on a system level but endow the long-term wearing comfort owning to adequate permeability, softness, and superelasticity when attached to the skin (Figure 7.2f). Therefore, WPE-skins can provide wireless, continuous, and comfortable physiological monitoring and intervention of the bodynet using a customized graphic user interface (GUI) and mobile devices during long-term wear. The WPE-skins are skin-attachable and stretchable, showing good permeability to moisture and liquid (Figure 7.2g), which are inflammation-free (Figure 7.2h) during chronic on-skin attachment for over one week in comparison to the impermeable thin-film E-skins (Film-skin) (Figure 7.3).

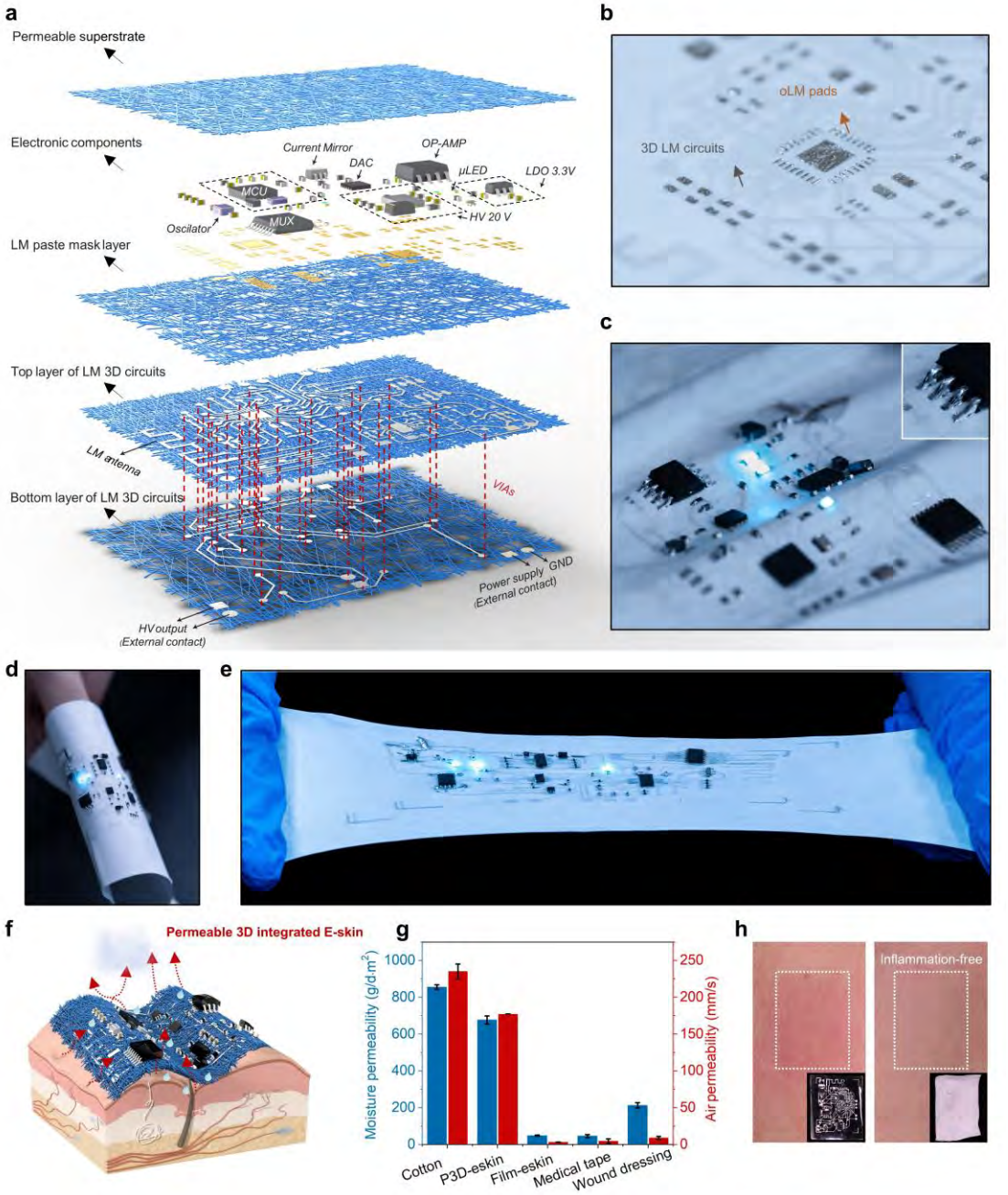

Figure 7.2 Design of the wireless permeable three-dimensional (3D) integrated electronic skins (WPE-skins). a, Exploded schematics of wireless permeable three-dimensional integrated electronic skins. Oxidation-engineered liquid metal (LM) microelectrodes are adopted as the reliable interface between the soft, rough fiber mat substrate and the rigid components. Vertical interconnect accesses (VIAs) are used for interlayer electrical connections. Key components in each layer are labeled. Microcontroller unit (MCU), oscillator, multiplexer (MUX), current mirror,

digital-analog-convertor (DAC), operational amplifier (OP-AMP), high voltage module (HV, 20V), and low dropout regulator (LDO, 3.3 V). The dashed lines indicate the distribution and positions of the VIAs in the system. **b,** Digital images of permeable 3D LM circuits and the oxidized LM (oLM) pads. **c,** Digital images of flexible and stretchable WPE-skins. **d, e,** Digital image showing the electrically stable output of the WPE-skin under flexing and stretching states, respectively. **f,** Schematic illustration showing the importance of permeability to air, moisture, and liquid for E-skins. **g,** Air and moisture permeability of WPE-skins, thin-film type of E-skin (Film-eskin, e.g. Polydimethylsiloxane (PDMS)-based), wound dressing, medical tape, and cotton fabric. **h,** Digital images showing the inflammation status of chest skins after the attachment of thin-film E-skin (FE skin, left), and WPE-skin for over a week. The inset images were the four-layer PDMS-based E-skin and the WPE-skin with the same device structure.

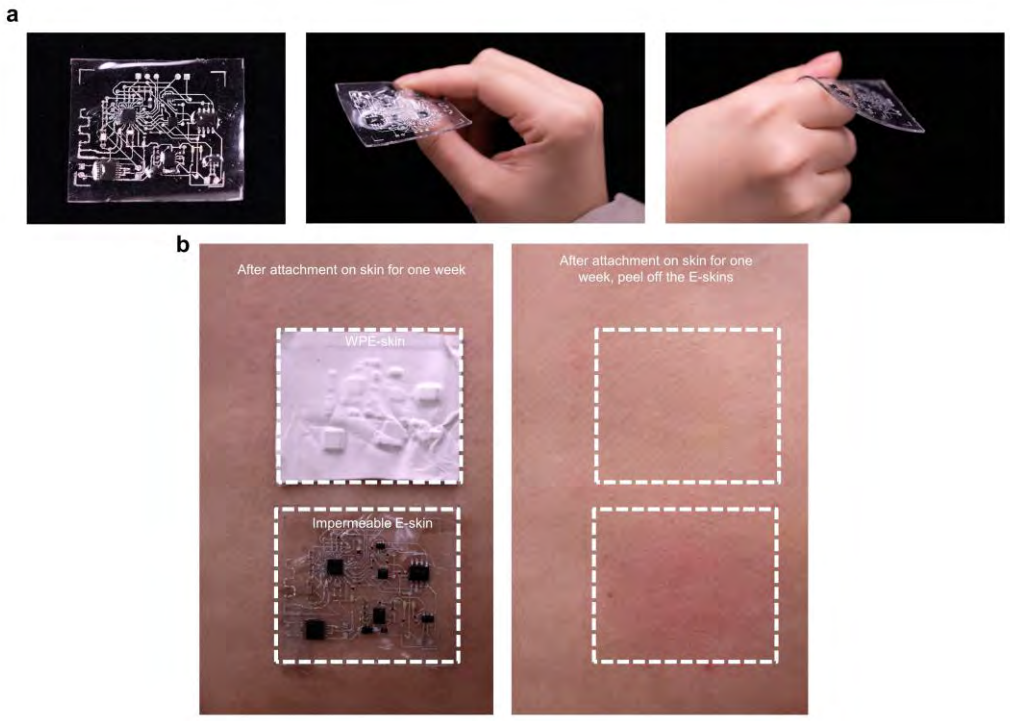

Figure 7.3 a, Digital images of impermeable thin-film type E-skin using the same circuit design (thickness: ~1mm). **b,** Digital images of the skin after the attachment of WPE-skin and impermeable E-skin for one week. After the removal of E-skins, WPE-skin did not cause obvious inflammation while the impermeable one did cause inflammation.

7.3 3D Integrated Reliable Electrical Interface with Components Using Oxidation-engineered LM

The key technology is to engineer a reliable 3D integrated electrical interface with microchips on the multilayered porous fiber mat using the micropatterned oxidation-engineered LM. Stiff LM serves as the pads and paste, and soft fluidic LM as the connections between pad and pins (bonding sites) enabling both in-plane and interlayer electrical connection with components, ensuring electrically stable connections both in-plane and out-of-plane even under a large strain. One critical challenge for current stretchable 3D electronics is the robust electrical interface with commercially well-developed components for both in-plane and out-of-plane integrations, which is even more challenging on those permeable but rough fiber mats. Here we adopted oxidation-engineered LM as the reliable electrical interface for the paste mask layer (Figure 7.4a), in which stiff oLM serves as the pads and paste, and soft fluidic LM as the connections between pads and pins (bonding sites), enabling both in-plane and interlayer electrical connection with components (Figure 7.4b). For thin interlayers (i.e., paste mask layer with a thickness of ~30 μm) (inset image in Figure 7.4c), LM pads can easily penetrate through the permeable structure with a maximum penetration depth of ~40 μm. For interlayer electrical connections. For thick interlayer (i.e., insulator layer between two layers of LM circuits), the LM pad can fill the laser-cutting Vertical interconnect accesses (VIAs) for the interlayer electrical connections (Figure 7.4c). In this way, stiff LM (with a heating duration of 16 h) can serve as the interconnections for the rigid components and the soft substrate, and soft and fluidic LM functions as the bonding sites for the circuits (Figure 7.4d). Conventionally, fluidic LM is difficult to be directly applied on various solid surfaces due to its intrinsic high surface tension of fluidic LM. Here the stiff LM pads were wettable to the pins of the component, soft fluidic LM, and the fiber mat, which ensured electrically stable connections in these electrical interfaces

under stretching status (Figure 7.4d, 7.4e). Here the maximum stress of the WPE-skin occurred around the chips of the system. By using oxidation-engineered LM, the stress concentration factor (Figure 7.4f) was also lower than that of using the bare chip (Figure 7.5).

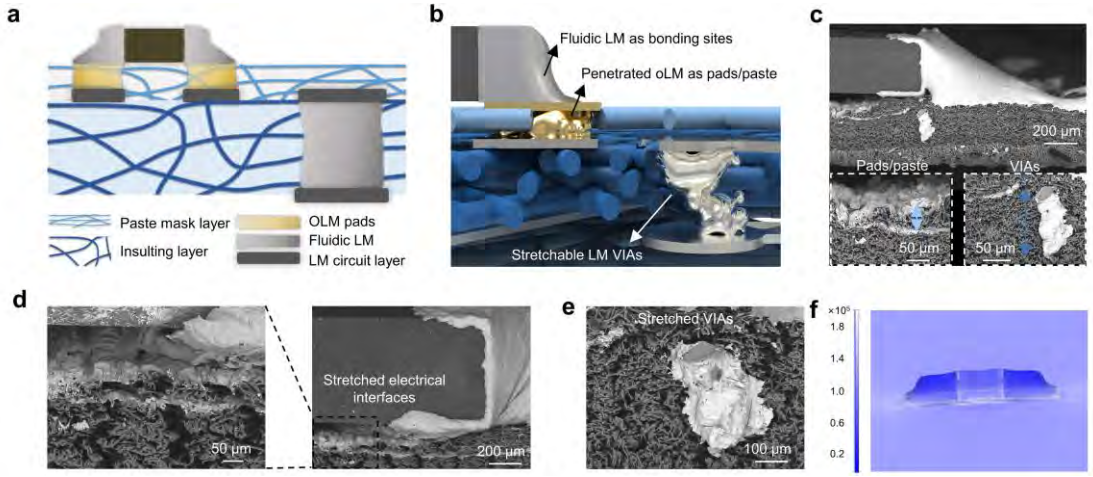

Figure 7.4 3D integrated reliable electrical interface with components using oxidation-engineered LM. a, Schematic illustration of the 3D integrated electrical interface of which stiff LM serves as the pads, soft fluidic Plm as the connections between pad and pins (bonding sites) enabling both in-plane and interlayer electrical connection with components. Conventionally, fluidic LM is difficult to be directly applied on various solid surfaces due to its intrinsic high surface tension. Here the stiff LM pads were wettable to the pins of the component, soft fluidic LM, and the fiber mat, which ensured electrically stable connections both in-plane and out-of-plane even under a large strain. **b,** Schematic-specific illustration of the interlayer electrical integration of the WPE-skins. For thin interlayers (i.e., paste mask layer with a thickness of ~30 μm, colored light blue in the image, LM pads can easily penetrate through the permeable structure for interlayer electrical connections. For thick interlayers (i.e., insulator layer between two layers of LM 3D circuits, the LM pad can fill the Vertical interconnect accesses (VIAs) for the interlayer electrical connections. **c,** Scanning electron microscope (SEM) image showing the electrical interface of a microresistor (0603) and the oxidation-engineered LM. Inset SEM images show the penetration depth of the oLM pads through the paste mask layer and the VIA. **d and e,** SEM images showing the 3D integrated

electrical interfaces, and the VIA under stretching status, respectively. **f,** Finite element analysis (FEA) of the stress distribution of the electrical interface of a chip with the oxidation-engineered LM.

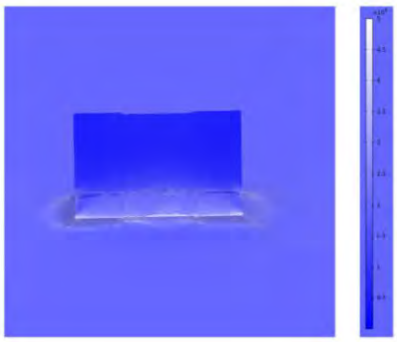

Figure 7.5 Finite element analysis (FEA) of the stress distribution of the electrical interface of a bare chip on the substrate at a tensile strain of 50%.

Here the stiff LM was prepared by oxidizing LM in air. The oxidation of LM could facilitate the wetting and spreading of LM onto solid surface. After heating LM with increasing duration ranging from 0 to 24 h, the size of the gallium (Ga) oxide enhanced from several μm to several hundred μm (Figure 7.6a). After pre-stretch under 1500% strain for 12 cycles, the continuous thin film (heating duration no more than 16 h) can self-organized into a laterally mesh-like and vertically buckled structure, with the formation of nodes from the strong oxide layer. Ga 2p (3/2) spectrum shows a predominant peak with a binding energy of 1118.8 eV from Ga_2O_3, with the presence of Ga metal (1116.5 eV) and Ga_2O (1118.2 eV) (Figure 7.6b). With increasing heating duration, the signals of the Ga oxides including Ga_2O_3 and Ga_2O became stronger (Figure 7.6c). Due to the strong oxidation of LM, the modulus from ~0.1 MPa to 0.3 MPa (Figure 7.6d). Accordingly, the oxidation enhanced by 2 folds with the same thickness of the specimens. The oxidized LM with a heating duration of 16 h remained high electrical conductivity of over 28,300 S/cm (Figure 7.6e) and low resistance change of 2.55 under a large strain of 1,500% (Figure 7.6f).

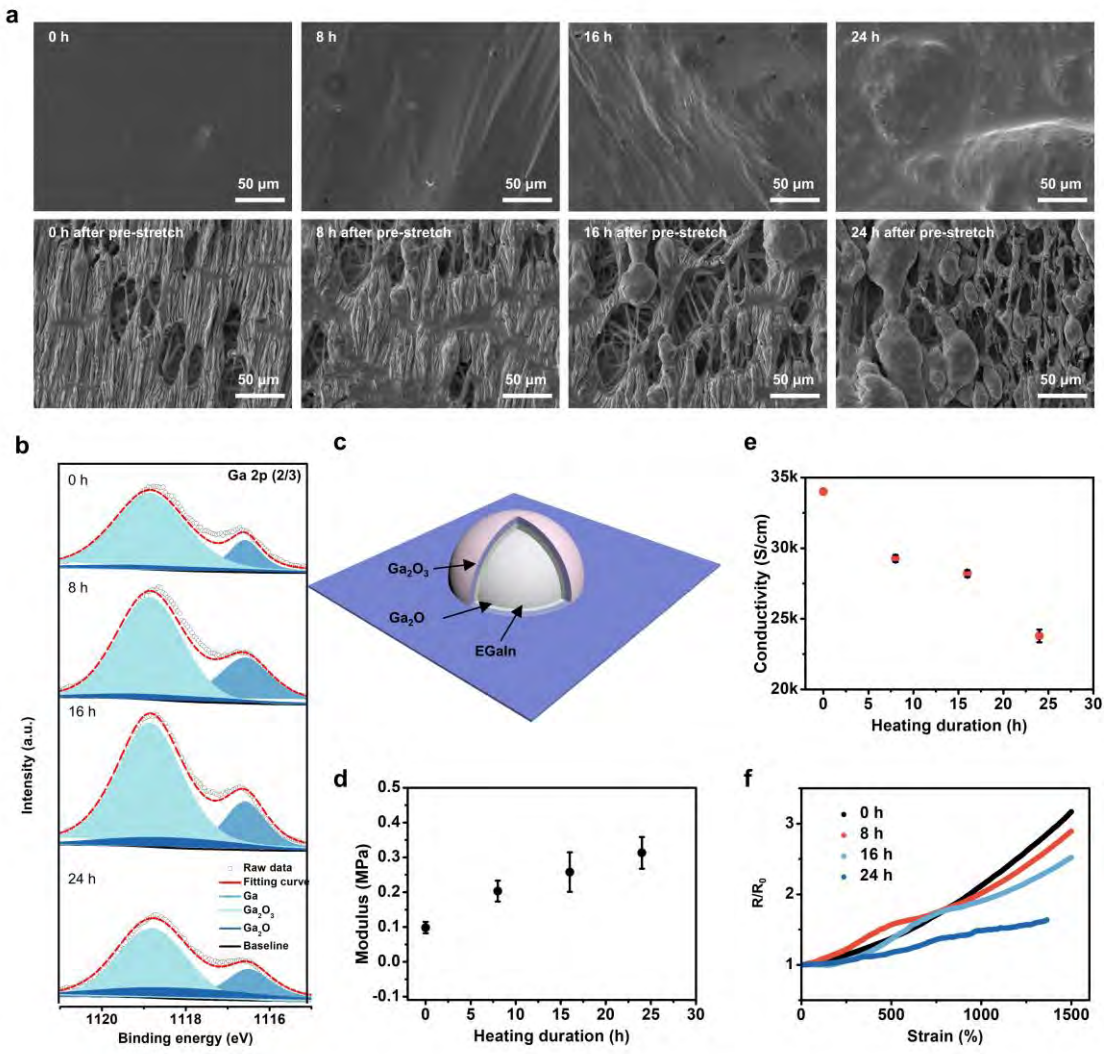

Figure 7.6 Characterizations of the stiff liquid metal (LM). a, Scanning electron microscope (SEM) images of LM with various heating duration before and after stretch. **b,** X-ray photoelectron spectroscopy (XPS) results of treated LM after various heating duration. **c,** Schematic illustration of the formation of the gallium (Ga) oxides (Ga_2O_3, and Ga_2O) during the heating of LM. Here LM is the eutectic gallium-indium (EGaIn). **d and e,** Young's modulus and electrical conductivity of treated LM after various heating duration. **f,** Resistance changes of treated LM as the function of tensile strain with various heating duration, respectively.

Compared with interconnections using soft LM, and stiff LM only, oxidation-engineered LM can be a reliable interface for the stretchable circuits under stretching (Figure 7.7a). We then employed the LM as a stretchable interconnect to interface with

commercial microresistors and light-emitting diodes (LEDs) to explore electrical stability. Compared with interconnections using soft or stiff LM only, the oxidation-engineered LM showed a much lower resistance change when interfacing with the zero-ohm microresistor (Figure 7.7b)

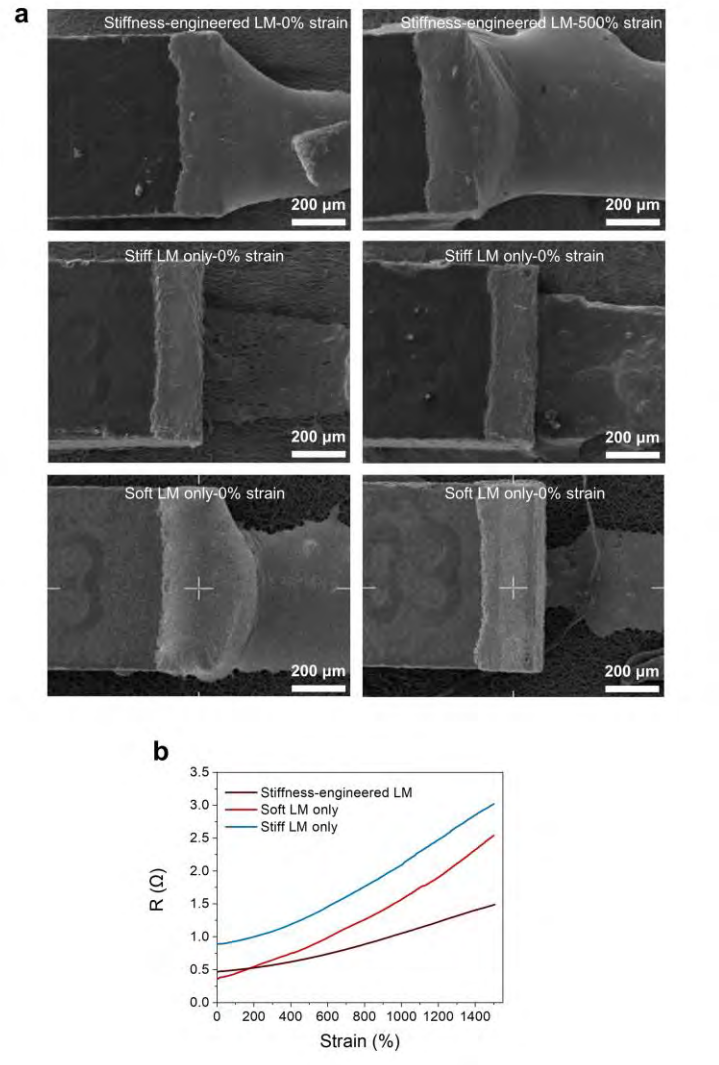

Figure 7.7 a, SEM images of LM the electrical interface with a zero-ohm microresistor (0603) before and under stretch using stiff LM or soft LM only or using oxidation-engineered LM. **b,** Electrical resistance change as the function of tensile strain showing the electrical stability of various electrical interfaces of soft or stiff LM only or using both stiff LM and soft LM integrating with a zero-ohm microresistor (0603).

For the microresistors with resistance ranging from 0 Ω to 1 MΩ, the resistance change is marginal under a large strain of 1,500% (Figure 7.8a). Additionally, the resistance was very stable in the cycling test of 100% strain, and under the large strain of 1500% strain (Figure 7.8b,). The luminance of the LED remained nearly the same during the stretching process (Figure 7.9).

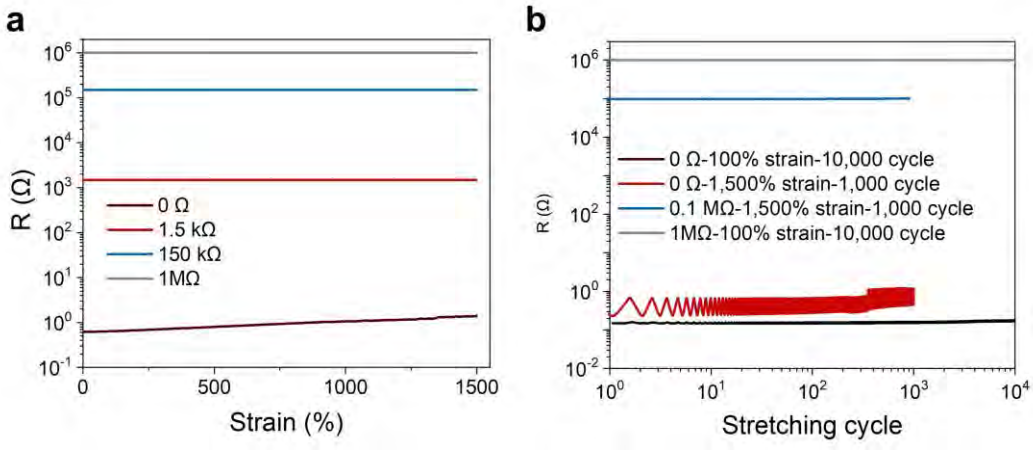

Figure 7.8 Electrical stability of the interface of oxidation-engineered LM with various microresistors as the function of (a) the tensile strain, and (b) stretching cycles, respectively.

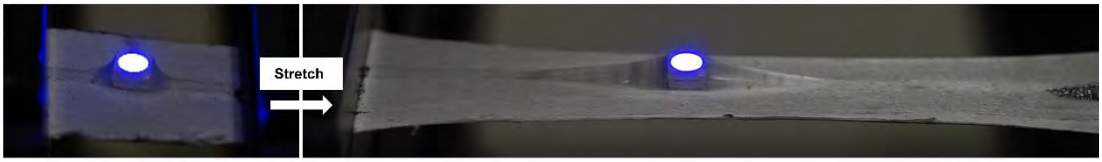

Figure 7.9 Digital image showing the electrically stable interface of oxidation-engineered LM with a LED under stretch. Conventionally, fluidic LM is difficult to be directly applied on various solid surfaces due to its intrinsic high surface tension. Here the stiff LM pads were wettable to the pins of the component, soft fluidic LM, and the fiber mat, which ensured electrically stable connections both in-plane and out-of-plane even under a large strain. Further, with the encapsulation of a thin permeable superelastic fiber mat, the electronic components can be immobilized onto the oxidation-engineered LM, leading to a better stability.

We have tested the long-term electrical stability of the sample (a thin LM circuit trace, 200 μm linewidth) that was stored in air (room temperature: ~25 °C, relative humidity: ~40 %) for eight months. The initial electrical resistance changed from 0.33 to 0.45 Ω, with marginal resistance change of only 0.113 at 100 % tensile strain after stretch-release cycles for over 17500 cycles (Figure 7.10).

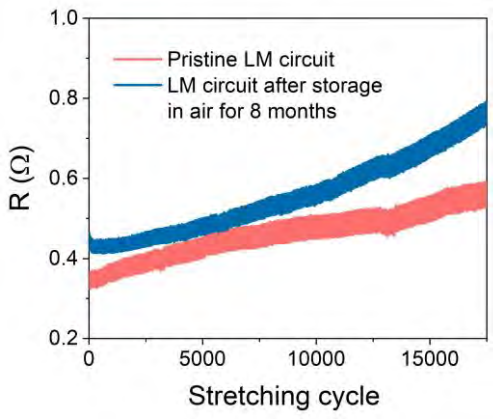

Figure 7.10 Electrical resistance changes of LM circuit traces (200 μm linewidths, with and without storage in air for 8 months) during stretch-release cycling tests of 100% strain.

We further demonstrated stretchable functional circuits using commercial metal–oxide–semiconductor field-effect transistors (MOSFETs), including P-Channel enhancement mode FETs (Figure 7.11a-c) and N-Channel logic level enhancement mode FETs (Figure 7.11d, e). The stretchable MOSFETs can operate even under large strains of up to 500% strain, with nearly no change in the driving voltage and transconductance.

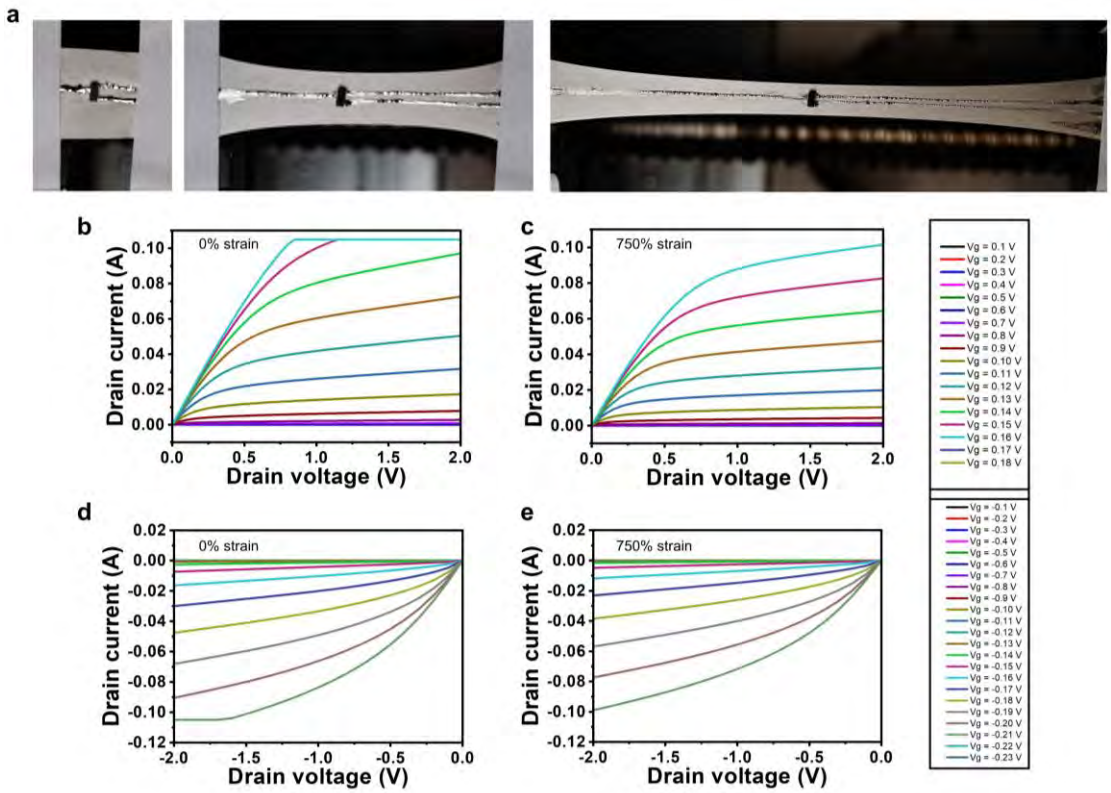

Figure 7.11 a, Digital image of stretchable Metal–oxide–semiconductor field-effect transistors (MOSFETs) using oxidation-engineered LM under stretch. **b and c,** Output characteristics of the stretchable P-Channel enhancement mode FETs at 0% strain, and 750% strain, respectively. **d and e,** Output characteristics of the stretchable N-Channel enhancement mode FETs at 0% strain, and 750% strain, respectively.

We proceeded to fabricate an inverse gate, Not-OR (NOR) gate, and clock-controlled switch (Figure 7.12a, 61b). These logics can operate normally in the logic output states under various strains (Figure 7.12c-h).

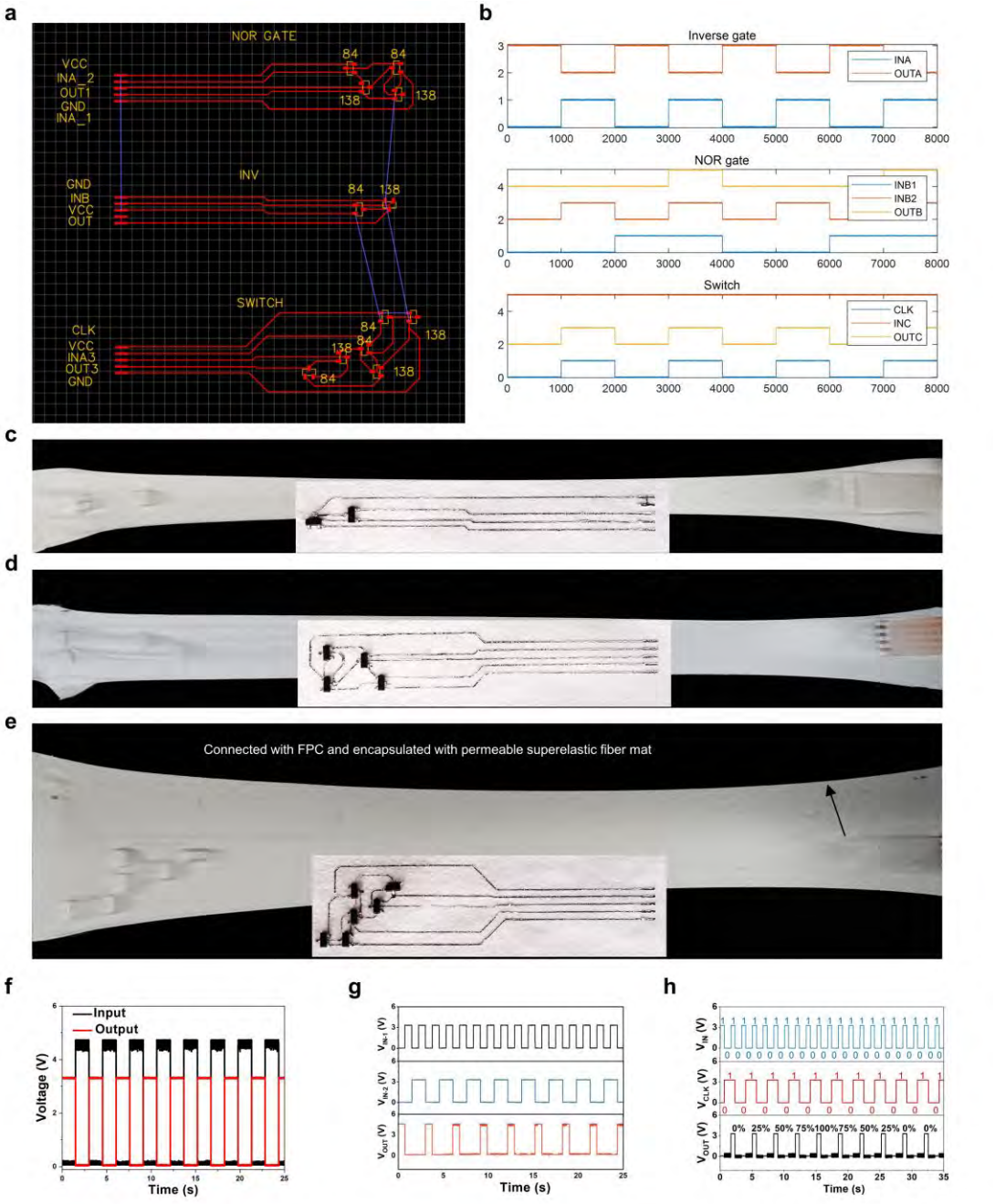

Figure 7.12 a, Design of the permeable stretchable logics including inverse gate, Not-OR (NOR) gate, and clock-controlled switch. **b,** Outputs of the logics with the hard printed circuit boards. **c, d, e,** Digital images of the inverse gate, Not-OR (NOR) gate, and clock-controlled switch. **f, g, h,** Logic outputs of the inverse gate, Not-OR (NOR) gate, and clock-controlled switch.

In addition, we developed the 3D integrated switch array layer by layer (Figure 7.13). The switches were used for controlling loads and in CMOS digital circuits as they

operate between their cut-off and saturation regions. The multi-channel switch array showed a uniform threshold driving voltage (Vg) of ~1.75 V at a strain of 50% and an average transconductance of ~100 mS (Figure 7.14).

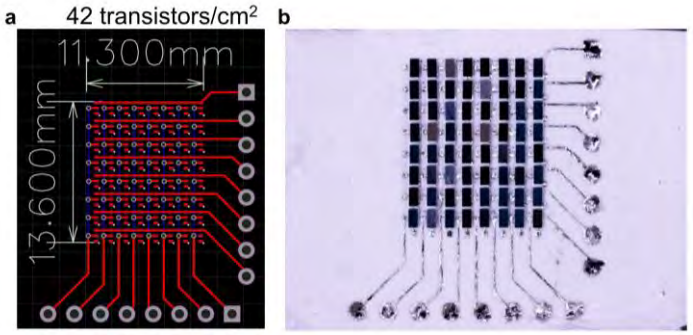

Figure 7.13 a, Design of the permeable stretchable multilayer switch array. **b,** Digital image of the permeable stretchable multilayer switch array.

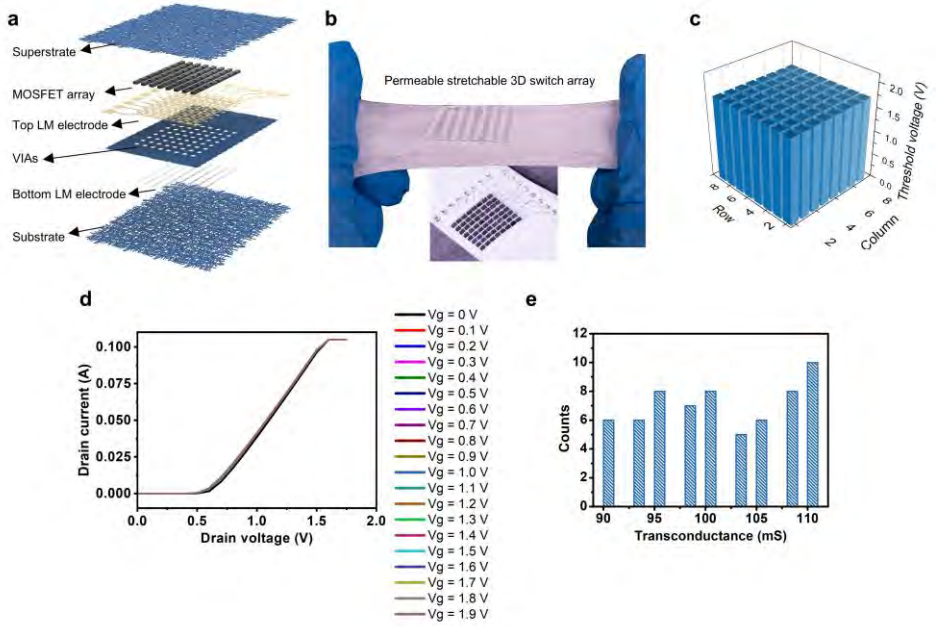

Figure 7.14 a and b, Schematic illustration and digital images of the permeable 3D integrated stretchable switch array. **c,** Threshold driving voltage of the switch array at a strain of 100%. **d,** Output characteristics of the 64-channel switch. **e,** Statistic analysis of the transconductance of the 64-channel switch array.

7.4 Characterizations of WPE-skin Systems Using Bluetooth

This WPE-skin can generate high-voltage electrical pulses with precisely controlled current intensity, frequency, and duty cycle, for delivering electrical stimulation to the user/animal's body. Therefore, we utilized this WPE-skin as a wearable transcutaneous electrical stimulator for the muscle and proved that it is fully functional to deliver stimulation to the bicep femoris on an experimental animal (Figure 7.15a). The electrical stimulation (ES) electrode and the electromyography (EMG) electrode was integrated with the WPE-skin, wirelessly communicated with a mobile device capable of EP data acquisition, filtering, amplification, RF transmission, and EP intervention. As illustrated in Figure 7.15b, The WPE-skin system was equipped with a Bluetooth Low Energy 5.1 (BLE) built-in MCU and matched 2.4 GHz liquid metal BLE antenna (planar inverted F-shaped Antenna), which endowed it with wireless control and data transmission functions by simply using a smartphone with customized GUI. To verify the wireless communication capability, we tested the furthest BLE connection distance, and it could stay stably connected from up to 15 meters away (Figure 7.15c). The power of WPE-skin is supplied by a lithium-ion battery, and the voltage is regulated by the LDO. By controlling the ON/OFF period of the MUX, the generated DC high voltage is transformed into periodical pulses in 2 channels, with a wide and precisely controlled frequency range (1-200 Hz, Figure 7.15d), and different duty cycles (1-10%, Figure 7.15e). By the skin-interfacing LM electrodes, the generated current pulses pass through the body and flowed into the current mirror of the current control module, where the current intensity is precisely set in the range from 0 to 10 mA (Figure 7.15f) by the output voltage of the DAC with different sent commands (Figure 7.15g), and the actual current intensity is transformed into a safely sensible voltage for MCU by an OP-AMP, as it's been described elsewhere[91]. To verify that it successfully stimulated the muscle, we placed a couple of stimulating LM electrodes (connected to WPE-skin) and a set of electrodes for real-time EMG monitoring at adjacent areas on the rat's bicep

femoris. During the stimulation period, corresponding EMG responses whose repetition frequency (1, 5, and 10 Hz) matched with stimulation current signals were observed (Figure 7.15h) clearly, which proved that electrical stimulation was successfully delivered.

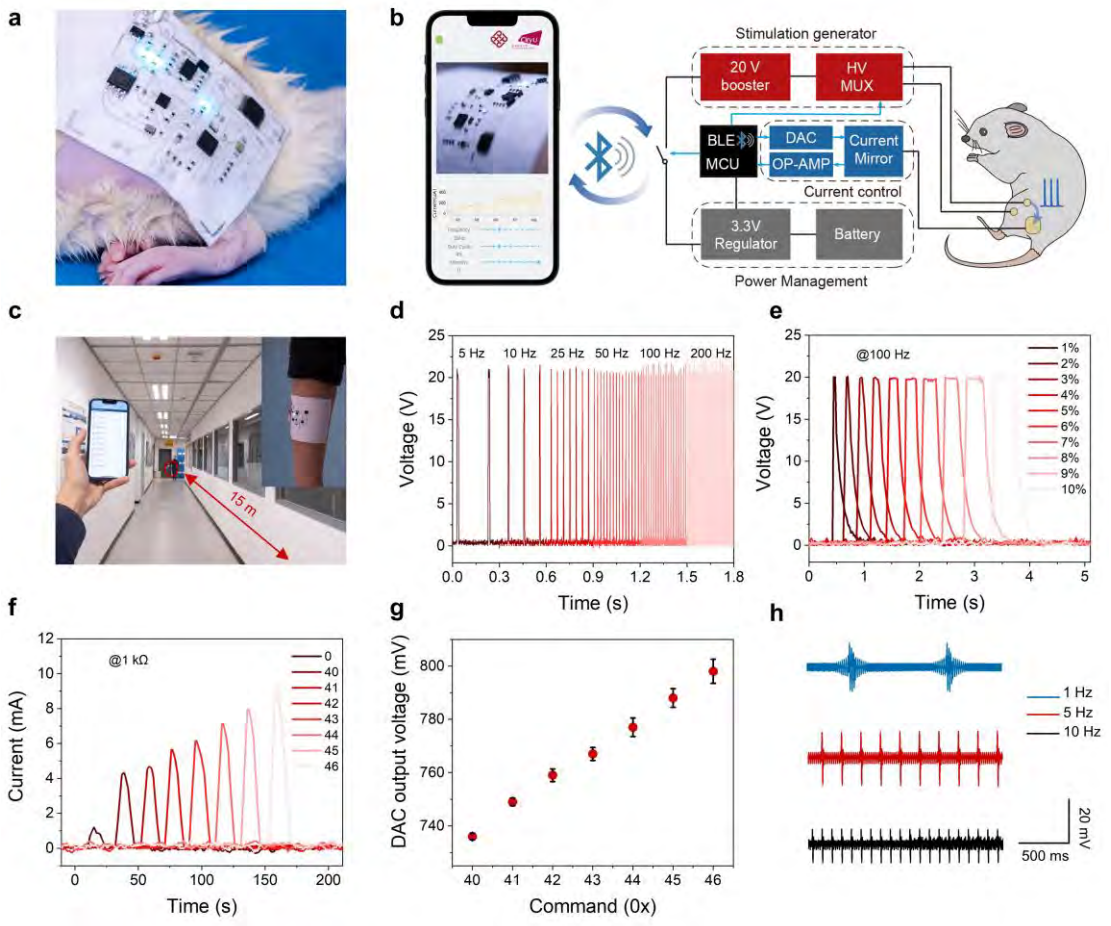

Figure 7.15 Characterizations of the WPE-skins using Bluetooth technology. a, Digital images showing the experimental setup, in which electrical stimulations can be delivered to the bicep femoris on a rat using the WPE-skin, and the corresponding EMG signals were recorded using the LM electrode. **b,** Brief block diagram of the WPE-skin system and the customized mobile app. OP-AMP, operational amplifier. DAC, digital to analog converter. **c,** Digital image showing the communication distance of the WPE-skin system. **d,** Generated stimulation pulses with controlled repetition frequency ranging from 5 Hz to 200 Hz. **e,** Generated stimulation pulses with controlled duty cycle ranging from 5 Hz to 200 Hz, frequency fixed at 100 Hz. **f,** Generated stimulation pulses

with controlled current intensity under different wirelessly sent commands (0 and 40~46) with a fixed load of 1 kΩ. **g.** Output control signal output voltages of DAC under different commands (40~46). **h.** Evoked EMG response signals under stimulation frequencies of 1, 5, and 10 Hz, respectively.

7.5 Characterizations of WPE-skin Systems Using Near-field Communication (NFC)

Likewise, we can develop the battery-free type of WPE-skin using near-field communication (NFC) technology, involving stretchable LM NFC antenna, paste mask layer, rigid components (MCU for NFC, ADC, sensors), permeable superelastic supporting surface (substrate, fiber mat), and encapsulation layer (superstrate, fiber mat) (Figure 7.16a). The NFC WPE-skin is highly stretchable with a maximum tensile strain of over 250% (Figure 7.16b).

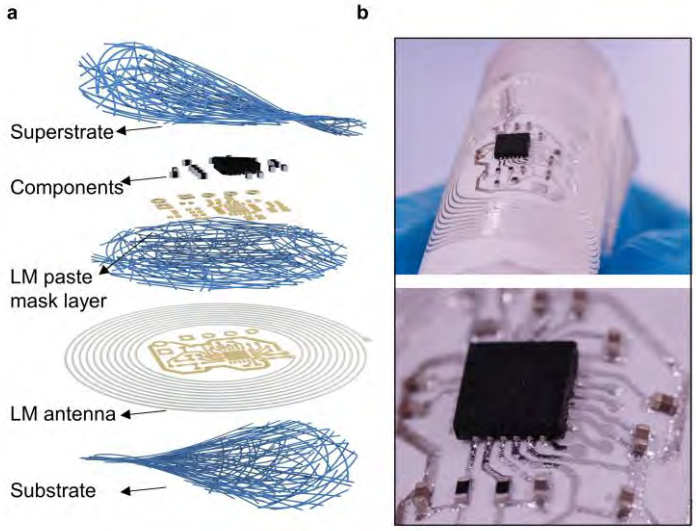

Figure 7.16 (a) Exploded schematics and (b) digital images of battery-free type of WPE-skins using near-field communication (NFC) technology. The system included the stretchable LM antenna, stretchable printed LM microcircuit integrated with microchips (MCU for NFC, ADC, sensors, transistors), and permeable fiber mats as the encapsulation and the substrates.

Such an assembling strategy possesses several advantages for wireless stretchable systems in terms of design compactness, stretchability, and electromagnetic stability. In comparison to a conventional stretchable Cu antenna in the shape of a serpentine structure with the same occupied area, the turn number (Figure 7.17a) of the LM coil was twice that of the Cu antenna. Moreover, the Cu antenna could only sustain a stretchability of up to 40% strain, at which the jump wire and the interconnects with the components were disconnected (Figure 7.17b) while the maximum strain of the LM antenna was ~250% strain.

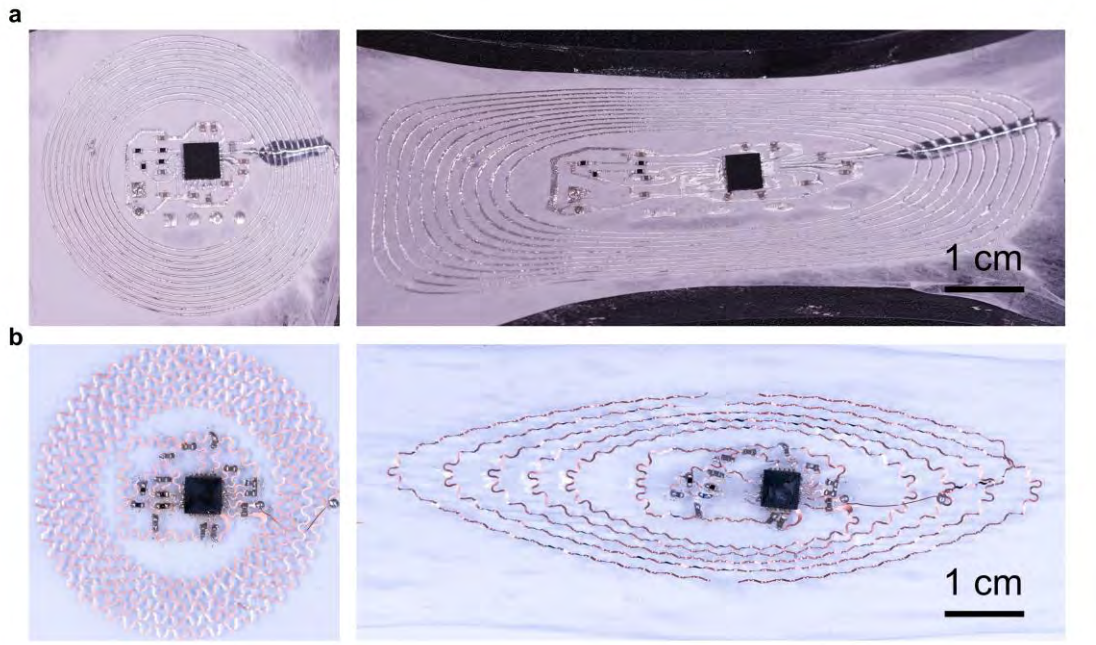

Figure 7.17 Digital images of (a) the intrinsically stretchable LM antenna, and (b) structured Cu antenna before and under stretching (40% strain).

According to the finite element analysis, the maximum stress of LM antenna (Figure 7.18a) was four orders smaller than that of the serpentine Cu antenna (Figure 7.18b). In addition, the stress concentration factor ($\sigma_{max}/\sigma_{avg}$) of the LM antenna was also 585 folds smaller than that of the serpentine Cu antenna, indicating a much more uniform stress distribution.

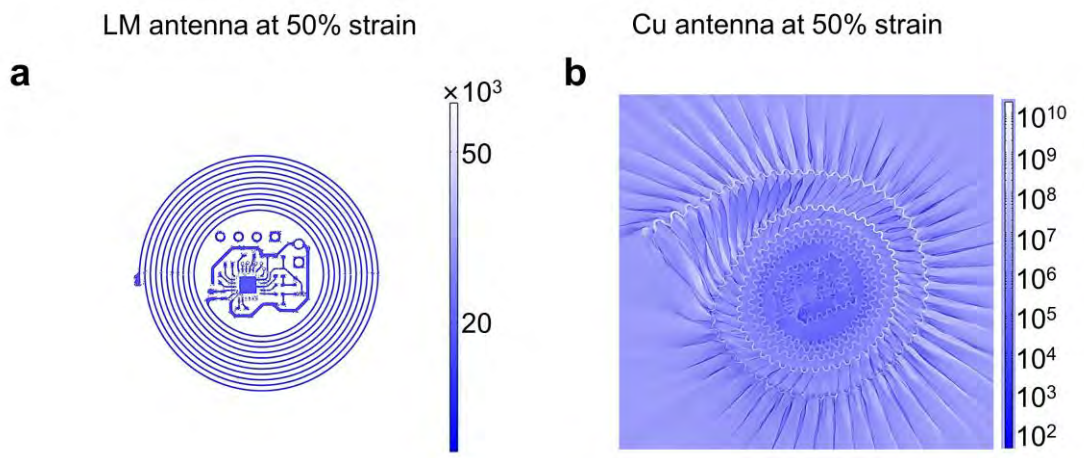

Figure 7.18 FEAs of the stress distribution of stretchable antennas using (a) the intrinsically stretchable LM antenna, and (b) structured Cu antenna, respectively.

Additionally, the LM coil showed higher inductance (Figure 7.19a, b) at various strains. , and operate normally in terms of impedance (Figure 7.20a), phase (Figure 7.20b), and Q factor (Figure 7.20c), and within the readable frequency around 13.56 MHz during the stretching process to ~100% strain.

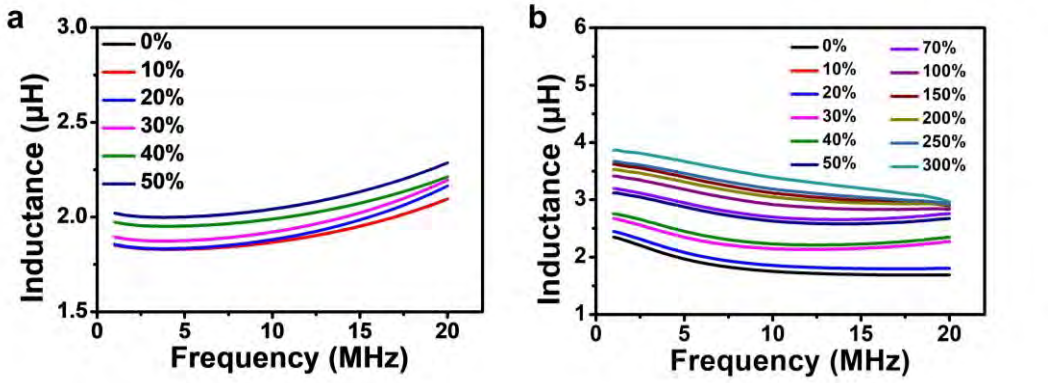

Figure 7.19 a, Inductance of the structured Cu antenna as the function of frequency at various strains. **b,** Inductance of the intrinsically stretchable LM antenna as the function of frequency at various strains.

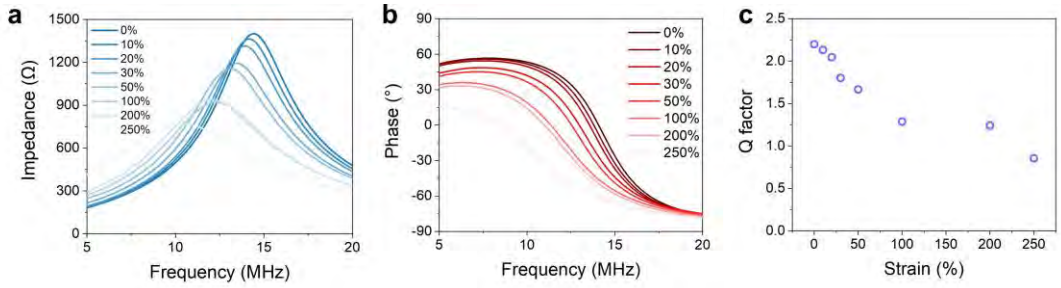

Figure 7.20 a-c, Q factor, impedance, and phase of the stretchable LM antenna at various strains, respectively.

The NFC WPE-skin can provide multi-position and continuous physiological monitoring for the on-skin bodynet with a working distance of ~12mm (Figure 7.21).

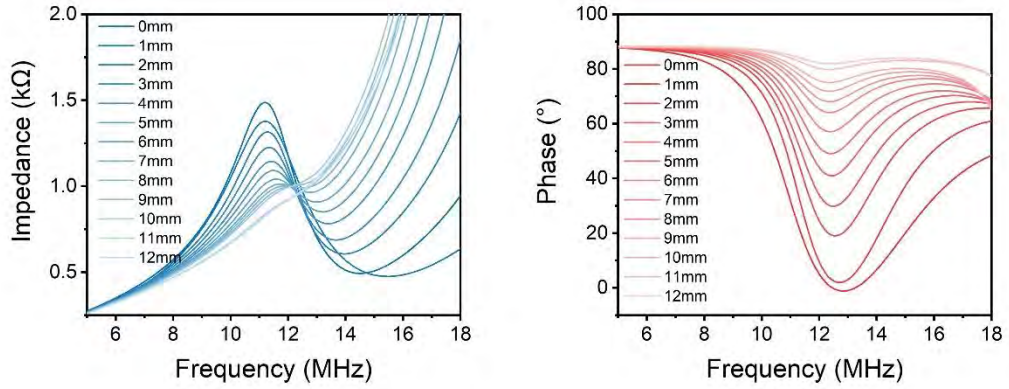

Figure 7.21 Impedance and phase of the LM antenna as the function of frequency at various working distances

As a proof of concept, the temperature sensor was soldered onto the E-skin. The temperature of the human body can be recorded continuously using a customized app. Thermal imagery of an adult male body in cool (Figure 7.22a) and warm (Figure 7.22b) environments can be depicted using the temperature body net consisting of 40 NFC WPE-skins all over the body. Moreover, continuous temperature of the human body during daily activities including sitting, walking, and exercising were monitored using the app (Figure 7.22c).

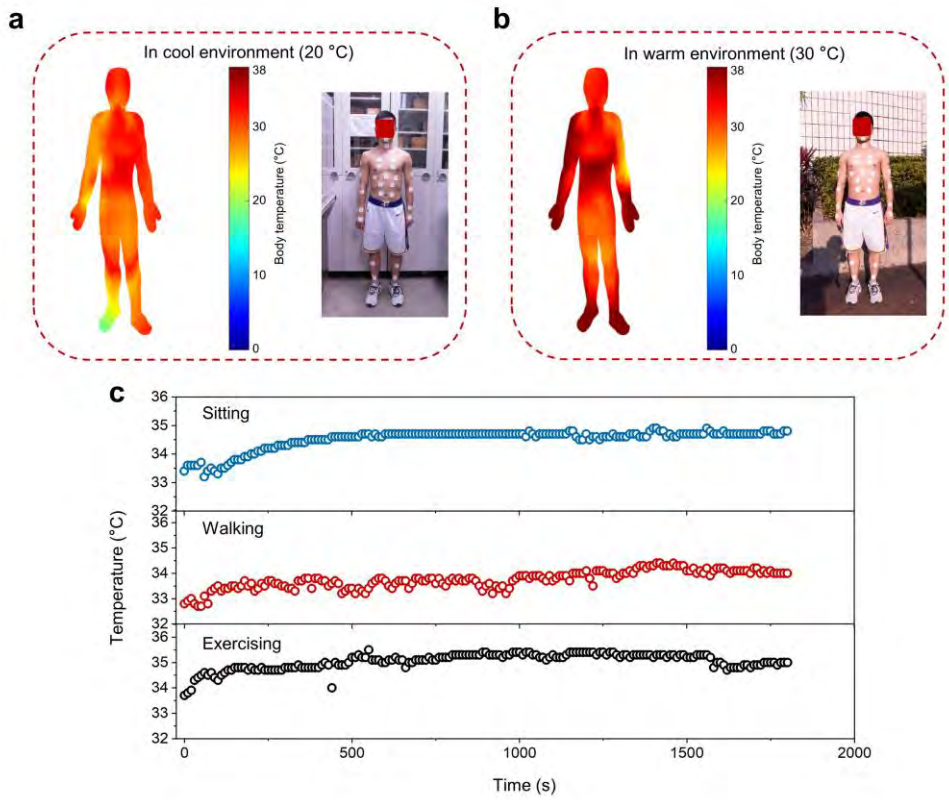

Figure 7.22 a and b, Thermal imagery of an adult male body using 40 NFC tags in cool and warm environments. **c,** Continuous temperature monitoring of an adult body during sitting, walking, and exercising.

In summary, 3D integrated electronics provide high-integration-density and multifunctionality and have been generally adopted in the current PCB industry. Incorporating commercial electronics such as unobtrusive, inexpensive, high-performance chips with stretchable printed circuits can potentially provide clinical-quality health monitoring capabilities for continuous use, beyond the confines of traditional hospitals or laboratories. Moreover, for long-term wearing ability, permeable stretchable type of 3D integrated electronics can endow chronic (long-term) wearing comfort and biocompatibility in comparison to conventional impermeable thin-film counterparts. Nevertheless, current permeable skin electronics still cannot achieve signal processing, computation, and communication on a system level owing to the lack of full integration with existing rigid components.

To fill this research gap, here we propose 3D integrated wireless permeable electronic skins (WPE-skins) with skin-like softness, adequate permeability for daily wearing, reliable electrical functions, potentially serving as portable, skin-like, and comfortable wearables in long-term applications. The 3D integration of WPE-skins typically involves the multilayer architecture consisting of 1) the bottom layer and 2) the top layer of the permeable stretchable LM 3D circuits, in which permeable and stretchable LM microelectrodes serve as antenna, traces, pads, paste, contacts, and vertical interconnect accesses (VIAs) for the multilayer LM circuits, 3) paste mask layer reliably interfacing with the electronic components using oxidation-engineered LM microelectrodes; and 4) permeable stretchable encapsulation layer using electrospun fiber mat.

We demonstrate two types of wireless permeable microelectronic systems using near-field communication (NFC, working distance: 12 mm) technology and Bluetooth circuits (communication distance: 15 m). WPE-skins can provide wireless, continuous, and comfortable physiological monitoring and intervention of the bodynet using a customized graphic user interface.

Chapter 8 Conclusions and Suggestions for Future Research

8.1 Conclusions

In this study, we developed a universal patterning, integration, and encapsulation technique for stretchable permeable liquid-metal-based microelectrodes (Plms, PlmHs), and microelectronic systems (WPE-eskins). So far, some progress has been made:

(1) We have successfully fabricated the micropatterns of Ag by the photolithography technique. The porous structure enables an omnidirectional etching and dissolving of the sacrificial layer and thus enables a rapid (within seconds) and defect-free transfer. Therefore, various shapes and dimensions of Ag patterns were transferred onto the SBS mat. By taking advantage of the wetting selectivity of LM on the SBS mat and Ag patterns, LM was later coated Ag patterns only, resulting in the successful patterning of LM electrodes on the permeable SBS mats (Plms).

(2) The successful preparation of Plms over a large-size, permeable, and stretchable fiber mat paves the way toward high-density, integrated, implantable, and chronically biocompatible LM electronics. At this moment, Plms display a typical patterning resolution of 2 μm by laboratory-equipped photolithography, moisture permeability of 990 $g/m^2/day$, device density over 75,000 $electrodes/cm^2$, electrical conductivity in the order of 10^5 S/cm, and stretchability up to 1,500% strain. In principle, the patterning resolution of Plms can be further enhanced to sub-micrometer (0.25~1 μm) regions, e.g., by using a high-resolution lithographic tool and fiber mat of smaller fiber diameters.

(3) We also developed wafer-scale tissue-like LM hydrogel bioelectrodes (PlmHs) with high stretchability, electrical conductivity, and patterning resolution up to 5 μm. The

PlmH shows tissue-like softness, outstanding electrical conductance when stretched up to 1,500% strain, low impedance, and high transparency with a linewidth of 5 μm. Highlighting its versatility, we use this platform to demonstrate multi-channel implantable hydrogel optogenetic bioelectronics with a high temporal-spatial resolution for the neural interface.

(4) We further propose the system-level integration of permeable and stretchable bioelectronics using LM. 3D integrated electronics providing high-integration density and multifunctionality have been generally adopted in the current PCB industry. Incorporating commercial electronics such as unobtrusive, inexpensive, high-performance chips with stretchable printed circuits can potentially provide clinical-quality health monitoring capabilities for continuous use, beyond the confines of traditional hospitals or laboratories. Moreover, for long-term wearing ability, permeable and stretchable type of 3D integrated electronics can endow chronic wearing comfort and health in comparison to conventional impermeable thin-film counterparts.

(5) The WPE-eskin platform reported herein offers the first demonstration of how to achieve 3D integrated circuit board with unique advantages of high-density functionalities, skin-like softness and stretchability, and high permeability to air and moisture. It provides a reliable and scalable solution to integrating well-developed rigid electronic components with stretchable fibrous substrates in a 3D configuration. In comparison to eskins made with stretchable thin film substrates, the WPE-eskin is significantly lighter, thinner, softer, more stretchable, and most importantly, offers chronic biocompatibility in the on-skin test.

8.2 Suggestions for Future Research

Throughout my Ph.D. studies, I have conducted comprehensive research on the development of LM based permeable stretchable bioelectronics and wireless systems

for both wearable and implantable applications. My research has encompassed materials preparation, microfabrication, device testing, and system-level integrations. In the future, I will explore their applications in continuous and comfortable healthcare monitoring, biomedicine, immersive VR/AR, and soft robotics. There are significant improvements that need to be done.

(1) The electrochemical stability of LM based bioelectronics is one of the key issues for chronic and stable signal recording. Therefore, I will investigate a better encapsulation strategy for these LM based permeable stretchable bioelectronics.

(2) The rheological behavior of LM during the patterning process needs further exploration.

(3) The photoinitiator (HMPP) adopted for preparation of hydrogel substrate was not very biocompatible for animals and human body. Biocompatible photoinitiator such as peroxides, peresters, iminosulphones will be included to further optimize this preparation protocol.

(4) The interfacial adhesion between current LM bioelectronics and skin/organ under wet conditions needs improvement to ensure a robust contact and stable signal recording.

(5) To further optimize the device performance in terms of signal-to-noise ratio, response time, and sensitivity.

References

1. Choi, S., Han, S. I., Kim, D., Hyeon, T. & Kim, D. H. High-performance stretchable conductive nanocomposites: Materials, processes, and device applications. *Chem. Soc. Rev.* **48**, 1566–1595 (2019).

2. Ma, R., Chou, S. Y., Xie, Y. & Pei, Q. Morphological/nanostructural control toward intrinsically stretchable organic electronics. *Chem. Soc. Rev.* **48**, 1741–1786 (2019).

3. Van der Valk, P. G. M. & Maibach, H. I. Post-application occlusion substantially increases the irritant response of the skin to repeated short-term sodium lauryl sulfate (SLS) exposure. *Contact Dermatitis* **21**, 335–338 (1989).

4. Zhai, H. & Maibach, H. I. Skin occlusion and irritant and allergic contact dermatitis: An overview. *Contact Dermatitis* **44**, 201–206 (2001).

5. Nakajima, M. NII-Electronic Library Service. *Chem. Pharm. Bull.* **120**, 2091 (2002).

6. Ma, Z. *et al.* Permeable superelastic liquid-metal fibre mat enables biocompatible and monolithic stretchable electronics. *Nat. Mater.* **20**, 859–868 (2021).

7. Miyamoto, A. *et al.* Inflammation-free, gas-permeable, lightweight, stretchable on-skin electronics with nanomeshes. *Nat. Nanotechnol.* **12**, 907–913 (2017).

8. Chen, F., Huang, Q. & Zheng, Z. Permeable Conductors for Wearable and On-Skin Electronics. *Small Struct.* **3**, 2100135 (2022).

9. Zheng, Y. Q. *et al.* Monolithic optical microlithography of high-density elastic circuits. *Science* **373**, 88–94 (2021).

10. Wang, S. *et al.* Skin electronics from scalable fabrication of an intrinsically stretchable transistor array. *Nature* **555**, 83–88 (2018).

11. Garnier, F., Hajlaoui, R., Yassar, A. & Srivastava, P. All-polymer field-effect transistor realized by printing techniques. *Science* **265**, 1684–1686 (1994).

12. Bao, Z., Feng, Y. & Dodabalapur, A. High-Performance Plastic Transistors. *Chem. Mater.* **4756**, 1372–1374 (1997).

13. Gelinck, G. H. *et al.* Flexible active-matrix displays and shift registers based on solution-processed organic transistors. *Nat. Mater.* **3**, 106–110 (2004).

14. Menard, E. *et al.* Micro- and nanopatterning techniques for organic electronic and optoelectronic systems. *Chem. Rev.* **107**, 1117–1160 (2007).

15. Rogers, J. A. *et al.* Paper-like electronic displays: Large-area rubber-stamped plastic sheets of electronics and microencapsulated electrophoretic inks. *Proc. Natl. Acad. Sci. U. S. A.* **98**, 4835–4840 (2001).

16. Rogers, J. A., Someya, T. & Huang, Y. Materials and mechanics for stretchable electronics. *Science* **327**, 1603–1607 (2010).

17. Kim, D.-H. stretch force reduction due to nanotube meander- ing. This structure provides a volume per strut of D′L 2 sin(120°) and a calculated density of r. *Nature* **320**, 507–511 (2008).

18. Park, S. Il *et al.* Theoretical and experimental studies of bending of inorganic electronic materials on plastic substrates. *Adv. Funct. Mater.* **18**, 2673–2684

(2008).

19. Kim, D. H. *et al.* Materials and noncoplanar mesh designs for integrated circuits with linear elastic responses to extreme mechanical deformations. *Proc. Natl. Acad. Sci. U. S. A.* **105**, 18675–18680 (2008).

20. Huang, K. & Peumans, P. Stretchable silicon sensor networks for structural health monitoring. *Smart Struct. Mater. 2006 Sensors Smart Struct. Technol. Civil, Mech. Aerosp. Syst.* **6174**, 617412 (2006).

21. Hung, P. J., Jeong, K., Liu, G. L. & Lee, L. P. Microfabricated suspensions for electrical connections on the tunable elastomer membrane. *Appl. Phys. Lett.* **85**, 6051–6053 (2004).

22. Mitrus, M. & Moscicki, L. Extrusion-cooking of starch protective loose-fill foams. *Chem. Eng. Res. Des.* **92**, 778–783 (2014).

23. Ravi Kumar, D. V., Woo, K. & Moon, J. Promising wet chemical strategies to synthesize Cu nanowires for emerging electronic applications. *Nanoscale* **7**, 17195–17210 (2015).

24. Sun, J. Y. *et al.* Highly stretchable and tough hydrogels. *Nature* **489**, 133–136 (2012).

25. Cole, T., Khoshmanesh, K. & Tang, S.-Y. Liquid Metal Enabled Biodevices. *Adv. Intell. Syst.* **3**, 2000275 (2021).

26. Daeneke, T. *et al.* Liquid metals: Fundamentals and applications in chemistry. *Chem. Soc. Rev.* **47**, 4073–4111 (2018).

27. Zhuang, Q. *et al.* Liquid–Metal-Superlyophilic and Conductivity–Strain-

Enhancing Scaffold for Permeable Superelastic Conductors. *Adv. Funct. Mater.* **31**, 2105587 (2021).

28. Wang, Y. *et al.* Robust, self-adhesive, reinforced polymeric nanofilms enabling gas-permeable dry electrodes for long-term application. *Proc. Natl. Acad. Sci. U. S. A.* **118**, 38 e2111904118 (2021).

29. Park, M. *et al.* Highly stretchable electric circuits from a composite material of silver nanoparticles and elastomeric fibres. *Nat. Nanotechnol.* **7**, 803–809 (2012).

30. Jiang, Z. *et al.* Highly Stretchable Metallic Nanowire Networks Reinforced by the Underlying Randomly Distributed Elastic Polymer Nanofibers via Interfacial Adhesion Improvement. *Adv. Mater.* **31**, 1903446 (2019).

31. Li, Y. *et al.* A Highly Stretchable and Permeable Liquid Metal Micromesh Conductor by Physical Deposition for Epidermal Electronics. *ACS Appl. Mater. Interfaces* **14**, 13713–13721 (2022).

32. Sun, B. *et al.* Gas-Permeable, Multifunctional On-Skin Electronics Based on Laser-Induced Porous Graphene and Sugar-Templated Elastomer Sponges. *Adv. Mater.* **30**, 1804327 (2018).

33. Chae, H. *et al.* Laser-Processed Nature-Inspired Deformable Structures for Breathable and Reusable Electrophysiological Sensors toward Controllable Home Electronic Appliances and Psychophysiological Stress Monitoring. *ACS Appl. Mater. Interfaces* **11**, 28387–28396 (2019).

34. Yang, X. *et al.* Ultrathin, Stretchable, and Breathable Epidermal Electronics Based on a Facile Bubble Blowing Method. *Adv. Electron. Mater.* **6**, (2020).

35. Wang, X., Guo, R. & Liu, J. Liquid Metal Based Soft Robotics: Materials, Designs, and Applications. *Adv. Mater. Technol.* **4**, 1800549 (2019).

36. Park, J. *et al.* Three-dimensional nanonetworks for giant stretchability in dielectrics and conductors. *Nat. Commun.* **3**, 916 (2012).

37. Parida, K. *et al.* Extremely stretchable and self-healing conductor based on thermoplastic elastomer for all-three-dimensional printed triboelectric nanogenerator. *Nat. Commun.* **10**, 2158 (2019).

38. Markvicka, E. J., Bartlett, M. D., Huang, X. & Majidi, C. An autonomously electrically self-healing liquid metal-elastomer composite for robust soft-matter robotics and electronics. *Nat. Mater.* **17**, 618–624 (2018).

39. Zheng, L. *et al.* Conductance-stable liquid metal sheath-core microfibers for stretchy smart fabrics and self-powered sensing. *Sci. Adv.* **7**, eabg4041 (2021).

40. Li, X. *et al.* Liquid Metal Droplets Wrapped with Polysaccharide Microgel as Biocompatible Aqueous Ink for Flexible Conductive Devices. *Adv. Funct. Mater.* **28**, 1804197 (2018).

41. Hirsch, A., Dejace, L. & Michaud, H. O. Harnessing the Rheological Properties of Liquid Metals To Shape Soft Electronic Conductors for Wearable Applications. *Acc. Chem. Res.* **52**, 534–544 (2019).

42. Joshipura, I. D., Ayers, H. R., Majidi, C. & Dickey, M. D. Methods to pattern liquid metals. *J. Mater. Chem. C* **3**, 3834–3841 (2015).

43. Khan, Y. *et al.* A New Frontier of Printed Electronics: Flexible Hybrid Electronics. *Adv. Mater.* **32**, 1905279 1905279 (2020).

44. Xu, S. *et al.* Soft microfluidic assemblies of sensors, circuits, and radios for the skin. *Science* **344**, 70–74 (2014).

45. Xu, S. *et al.* Stretchable batteries with self-similar serpentine interconnects and integrated wireless recharging systems. *Nat. Commun.* **4**, (2013).

46. Zhang, Y. *et al.* A hierarchical computational model for stretchable interconnects with fractal-inspired designs. *J. Mech. Phys. Solids* **72**, 115–130 (2014).

47. Keum, H., Mccormick, M., Liu, P., Zhang, Y. & Omenetto, F. G. RESEARCH ARTICLES Epidermal Electronics. **333**, (2011).

48. Webb, R. C. *et al.* Ultrathin conformal devices for precise and continuous thermal characterization of human skin. *Nat. Mater.* **12**, 938–944 (2013).

49. Chang, J. F., Gwinner, M. C., Caironi, M., Sakanoue, T. & Sirringhaus, H. Conjugated-polymer-based lateral heterostructures defined by high-resolution photolithography. *Adv. Funct. Mater.* **20**, 2825–2832 (2010).

50. Gaikwad, A. M. *et al.* Identifying orthogonal solvents for solution processed organic transistors. *Org. Electron.* **30**, 18–29 (2016).

51. Zakhidov, A. A. *et al.* Hydrofluoroethers as orthogonal solvents for the chemical processing of organic electronic materials. *Adv. Mater.* **20**, 3481–3484 (2008).

52. Shendure, J. *et al.* Molecular biology: Accurate multiplex polony sequencing of an evolved bacterial genome. *Science* **309**, 1728–1732 (2005).

53. Tavakoli, M. *et al.* EGaIn-Assisted Room-Temperature Sintering of Silver Nanoparticles for Stretchable, Inkjet-Printed, Thin-Film Electronics. *Adv. Mater.* **30**, 1801852 (2018).

54. Albrecht, A., Rivadeneyra, A., Abdellah, A., Lugli, P. & Salmerón, J. F. Inkjet printing and photonic sintering of silver and copper oxide nanoparticles for ultra-low-cost conductive patterns. *J. Mater. Chem. C* **4**, 3546–3554 (2016).

55. Bihar, E. *et al.* Inkjet-Printed PEDOT:PSS Electrodes on Paper for Electrocardiography. *Adv. Healthc. Mater.* **6**, (2017).

56. Ke, S. H. *et al.* Printing the ultra-long ag nanowires inks onto the flexible textile substrate for stretchable electronics. *Nanomaterials* **9**, 686 (2019).

57. Shen, Y. *et al.* Solvent-free electrically conductive Ag/ethylene vinyl acetate (EVA) composites for paper-based printable electronics. *RSC Adv.* **9**, 19501–19507 (2019).

58. Liang, Y. *et al.* Electric power generation: Via asymmetric moisturizing of graphene oxide for flexible, printable and portable electronics. *Energy Environ. Sci.* **11**, 1730–1735 (2018).

59. Zhang, Q., Gao, Y. & Liu, J. Atomized spraying of liquid metal droplets on desired substrate surfaces as a generalized way for ubiquitous printed electronics. *Appl. Phys. A Mater. Sci. Process.* **116**, 1091–1097 (2014).

60. Wang, Y., Wang, J., Cao, S. & Kong, D. A stretchable and breathable form of epidermal device based on elastomeric nanofibre textiles and silver nanowires. *J. Mater. Chem. C* **7**, 9748–9755 (2019).

61. Quain, E. *et al.* Direct Writing of Additive-Free MXene-in-Water Ink for Electronics and Energy Storage. *Adv. Mater. Technol.* **4**, 1800256 (2019).

62. Zhang, Y. *et al.* Flexible electronics based on micro/nanostructured paper. *Adv.*

Mater. **30**, 1801588 (2018).

63. Shrivas, K., Ghosale, A., Kant, T., Bajpai, P. K. & Shankar, R. The direct-writing of low cost paper based flexible electrodes and touch pad devices using silver nano-ink and ZnO nanoparticles. *RSC Adv.* **9**, 17868–17876 (2019).

64. Zhang, M. *et al.* Time-space-resolved origami hierarchical electronics for ultrasensitive detection of physical and chemical stimuli. *Nat. Commun.* **10**, (2019).

65. Lee, S. *et al.* Nanomesh pressure sensor for monitoring finger manipulation without sensory interference. *Science* **370**, 966–970 (2020).

66. Yun, M. J., Sim, Y. H., Lee, D. Y. & Cha, S. I. Highly stretchable large area woven, knitted and robust braided textile based interconnection for stretchable electronics. *Sci. Rep.* **11**, 4038 (2021).

67. Wicaksono, I. *et al.* A tailored, electronic textile conformable suit for large-scale spatiotemporal physiological sensing in vivo. *npj Flex. Electron.* **4**, 5 (2020).

68. Zhou, W. *et al.* Gas-Permeable, Ultrathin, Stretchable Epidermal Electronics with Porous Electrodes. *ACS Nano* **14**, 5798–5805 (2020).

69. Dallinger, A., Keller, K., Fitzek, H. & Greco, F. Stretchable and Skin-Conformable Conductors Based on Polyurethane/Laser-Induced Graphene. *ACS Appl. Mater. Interfaces* **12**, 19855–19865 (2020).

70. Linghu, C., Zhang, S., Wang, C. & Song, J. Transfer printing techniques for flexible and stretchable inorganic electronics. *npj Flex. Electron.* **2**, (2018).

71. Carlson, A. *et al.* Active, programmable elastomeric surfaces with tunable

adhesion for deterministic assembly by transfer printing. *Adv. Funct. Mater.* **22**, 4476–4484 (2012).

72. Yoo, B., Cho, S., Seo, S. & Lee, J. Elastomeric angled microflaps with reversible adhesion for transfer-printing semiconductor membranes onto dry surfaces. *ACS Appl. Mater. Interfaces* **6**, 19247–19253 (2014).

73. Wu, W. Stretchable electronics: functional materials, fabrication strategies and applications. *Sci. Technol. Adv. Mater.* **20**, 187–224 (2019).

74. Fernandes, D. F., Majidi, C. & Tavakoli, M. Digitally printed stretchable electronics: A review. *J. Mater. Chem. C* **7**, 14035–14068 (2019).

75. Bihar, E. *et al.* Inkjet-Printed PEDOT:PSS Electrodes on Paper for Electrocardiography. *Adv. Healthc. Mater.* **6**, 1601167 (2017).

76. Lim, T., Kim, H. J., Zhang, H. & Lee, S. Screen-printed conductive pattern on spandex for stretchable electronic textiles. *Smart Mater. Struct.* **30**, 075006 (2021).

77. Zhang, M. *et al.* Time-space-resolved origami hierarchical electronics for ultrasensitive detection of physical and chemical stimuli. *Nat. Commun.* **10**, 1120 (2019).

78. Miyamoto, A. *et al.* Inflammation-free, gas-permeable, lightweight, stretchable on-skin electronics with nanomeshes. *Nat. Nanotechnol.* **12**, 907–913 (2017).

79. Park, M. *et al.* Highly stretchable electric circuits from a composite material of silver nanoparticles and elastomeric fibres. *Nat. Nanotechnol.* **7**, 803–809 (2012).

80. Wang, C. *et al.* Intrinsically Stretchable and Conductive Textile by a Scalable

Process for Elastic Wearable Electronics. *ACS Appl. Mater. Interfaces* **9**, 13331–13338 (2017).

81. Tian, L. *et al.* Large-area MRI-compatible epidermal electronic interfaces for prosthetic control and cognitive monitoring. *Nat. Biomed. Eng.* **3**, 194–205 (2019).

82. Zhuang, Q. *et al.* Wafer-patterned, permeable, and stretchable liquid metal microelectrodes for implantable bioelectronics with chronic biocompatibility. *Sci. Adv.* **9**, eadg8602 (2023).

83. Sim, K. *et al.* An epicardial bioelectronic patch made from soft rubbery materials and capable of spatiotemporal mapping of electrophysiological activity. *Nat. Electron.* **3**, 775–784 (2020).

84. Tian, L. *et al.* Large-area MRI-compatible epidermal electronic interfaces for prosthetic control and cognitive monitoring. *Nat. Biomed. Eng.* **3**, 194–205 (2019).

85. Wang, Y. *et al.* Skin bioelectronics towards long-term, continuous health monitoring. *Chem. Soc. Rev.* **51**, 3759–3793 (2022).

86. Kwon, K. *et al.* A battery-less wireless implant for the continuous monitoring of vascular pressure, flow rate and temperature. *Nat. Biomed. Eng.* (2023) doi:10.1038/s41551-023-01022-4.

87. Yang, Y. & Gao, W. Wearable and flexible electronics for continuous molecular monitoring. *Chem. Soc. Rev.* **48**, 1465–1491 (2019).

88. Tu, J. *et al.* A wireless patch for the monitoring of C-reactive protein in sweat.

Nat. Biomed. Eng. (2023) doi:10.1038/s41551-023-01059-5.

89. Wang, M. *et al.* A wearable electrochemical biosensor for the monitoring of metabolites and nutrients. *Nat. Biomed. Eng.* **6**, 1225–1235 (2022).

90. Yu, X. *et al.* Skin-integrated wireless haptic interfaces for virtual and augmented reality. *Nature* **575**, 473–479 (2019).

91. Yao, K. *et al.* Encoding of tactile information in hand via skin-integrated wireless haptic interface. *Nat. Mach. Intell.* **4**, 893–903 (2022).

92. Bardi, E. *et al.* Upper limb soft robotic wearable devices: a systematic review. *J. Neuroeng. Rehabil.* **19**, 87 (2022).

93. Yoo, J., Tang, S. & Gao, W. Micro- and nanorobots for biomedical applications in the brain. *Nat. Rev. Bioeng.* **1**, 308–310 (2023).

94. Xue, J., Wu, T., Dai, Y. & Xia, Y. Electrospinning and electrospun nanofibers: Methods, materials, and applications. *Chem. Rev.* **119**, 5298–5415 (2019).

95. Kaltenbrunner, M. *et al.* An ultra-lightweight design for imperceptible plastic electronics. *Nature* **499**, 458–463 (2013).

96. Salatino, J. W., Ludwig, K. A., Kozai, T. D. Y. & Purcell, E. K. Glial responses to implanted electrodes in the brain. *Nat. Biomed. Eng.* **1**, 862–877 (2017).

97. Doloff, J. C. *et al.* The surface topography of silicone breast implants mediates the foreign body response in mice, rabbits and humans. *Nat. Biomed. Eng.* **5**, 1115–1130 (2021).

98. Chiang, C. H. *et al.* Development of a neural interface for high-definition, long-

term recording in rodents and nonhuman primates. *Sci. Transl. Med.* **12**, eaay4682 (2020).

99. Zhuang, Q. *et al.* Wafer-patterned , permeable , and stretchable liquid metal microelectrodes for implantable bioelectronics with chronic biocompatibility. *Sci. Adv.* **9**, eadg8602 (2023).

100. Kim, M. gu, Brown, D. K. & Brand, O. Nanofabrication for all-soft and high-density electronic devices based on liquid metal. *Nat. Commun.* **11**, 1002 (2020).

101. Kim, M. G., Alrowais, H., Pavlidis, S. & Brand, O. Size-Scalable and High-Density Liquid-Metal-Based Soft Electronic Passive Components and Circuits Using Soft Lithography. *Adv. Funct. Mater.* **27**, 1604466 (2017).

102. Gozen, B. A., Tabatabai, A., Ozdoganlar, O. B. & Majidi, C. High-density soft-matter electronics with micron-scale line width. *Adv. Mater.* **26**, 5211–5216 (2014).

103. Kim, M. gu, Kim, C., Alrowais, H. & Brand, O. Multiscale and Uniform Liquid Metal Thin-Film Patterning Based on Soft Lithography for 3D Heterogeneous Integrated Soft Microsystems: Additive Stamping and Subtractive Reverse Stamping. *Adv. Mater. Technol.* **3**, 1800061 (2018).

104. Jeong, S. H. *et al.* Liquid alloy printing of microfluidic stretchable electronics. *Lab Chip* **12**, 4657–4664 (2012).

105. Lazarus, N., Bedair, S. S. & Kierzewski, I. M. Ultrafine pitch stencil printing of liquid metal alloys. *ACS Appl. Mater. Interfaces* **9**, 1178–1182 (2017).

106. Park, C. W. *et al.* Photolithography-Based Patterning of Liquid Metal

Interconnects for Monolithically Integrated Stretchable Circuits. *ACS Appl. Mater. Interfaces* **8**, 15459–15465 (2016).

107. Gao, Y. *et al.* Wearable Microfluidic Diaphragm Pressure Sensor for Health and Tactile Touch Monitoring. *Adv. Mater.* **29**, 1701985 (2017).

108. Lin, Y. *et al.* Vacuum filling of complex microchannels with liquid metal. *Lab Chip* **17**, 3043–3050 (2017).

109. Boley, J. W., White, E. L., Chiu, G. T. C. & Kramer, R. K. Direct writing of gallium-indium alloy for stretchable electronics. *Adv. Funct. Mater.* **24**, 3501–3507 (2014).

110. Ladd, C., So, J. H., Muth, J. & Dickey, M. D. 3D printing of free standing liquid metal microstructures. *Adv. Mater.* **25**, 5081–5085 (2013).

111. Kim, D., Yoon, Y., Kauh, S. K. & Lee, J. Towards Sub-Microscale Liquid Metal Patterns: Cascade Phase Change Mediated Pick-n-Place Transfer of Liquid Metals Printed and Stretched over a Flexible Substrate. *Adv. Funct. Mater.* **28**, 1800380 (2018).

112. Pan, C. *et al.* Visually Imperceptible Liquid-Metal Circuits for Transparent, Stretchable Electronics with Direct Laser Writing. *Adv. Mater.* **30**, 1706937 (2018).

113. Khan, M. R., Bell, J. & Dickey, M. D. Localized Instabilities of Liquid Metal Films via In-Plane Recapillarity. *Adv. Mater. Interfaces* **3**, 1600546 (2016).

114. Molina-Luna, K. *et al.* Cortical stimulation mapping using epidurally implanted thin-film microelectrode arrays. *J. Neurosci. Methods* **161**, 118–125 (2007).

115. Hollenberg, B. A., Richards, C. D., Richards, R., Bahr, D. F. & Rector, D. M. A MEMS fabricated flexible electrode array for recording surface field potentials. *J. Neurosci. Methods* **153**, 147–153 (2006).

116. Kim, J., Wilson, J. A. & Williams, J. C. A cortical recording platform utilizing microECoG electrode arrays. *Conf. Proc. IEEE Eng. Med. Biol. Soc.* **2721**, 5353–5357 (2007).

117. Rubehn, B., Bosman, C., Oostenveld, R., Fries, P. & Stieglitz, T. A MEMS-based flexible multichannel ECoG-electrode array. *J. Neural Eng.* **6**, 036003 (2009).

118. Ledochowitsch, P. *et al.* Fabrication and testing of a large area, high density, parylene MEMS μECoG array. *Proc. IEEE Int. Conf. Micro Electro Mech. Syst.* 1031–1034 (2011) doi:10.1109/MEMSYS.2011.5734604.

119. Besle, J. *et al.* Tuning of the human neocortex to the temporal dynamics of attended events. *J. Neurosci.* **31**, 3176–3185 (2011).

120. Viventi, J. *et al.* Flexible, foldable, actively multiplexed, high-density electrode array for mapping brain activity in vivo. *Nat. Neurosci.* **14**, 1599–1605 (2011).

121. Khodagholy, D. *et al.* NeuroGrid: Recording action potentials from the surface of the brain. *Nat. Neurosci.* **18**, 310–315 (2015).

122. Escabí, M. A. *et al.* A high-density, high-channel count, multiplexed μECOG array for auditory-cortex recordings. *J. Neurophysiol.* **112**, 1566–1583 (2014).

123. Hotson, G. *et al.* Individual finger control of a modular prosthetic limb using high-density electrocorticography in a human subject. *J. Neural Eng.* **13**, 26017

(2016).

124. Kellis, S. *et al.* Multi-scale analysis of neural activity in humans: Implications for micro-scale electrocorticography. *Clin. Neurophysiol.* **127**, 591–601 (2016).

125. Khodagholy, D. *et al.* Organic electronics for high-resolution electrocorticography of the human brain. *Sci. Adv.* **2**, e1601027 (2016).

126. Kaiju, T. *et al.* High spatiotemporal resolution ECoG recording of somatosensory evoked potentials with flexible micro-electrode arrays. *Front. Neural Circuits* **11**, 20 (2017).

127. Kim, D.-H. *et al.* Epidermal Electronics. *Science* **333**, 838–843 (2011).

128. Niu, S. *et al.* A wireless body area sensor network based on stretchable passive tags. *Nat. Electron.* **2**, 361–368 (2019).

129. Wang, C. *et al.* Imaging of Diverse Organs. *Science* **377**, 517–523 (2022).

130. Hu, H. *et al.* A wearable cardiac ultrasound imager. *Nature* **613**, 667–675 (2023).

131. Jiang, Y. *et al.* Topological supramolecular network enabled high-conductivity, stretchable organic bioelectronics. *Science* **375**, 1411–1417 (2022).

132. Deng, J. *et al.* Electrical bioadhesive interface for bioelectronics. *Nat. Mater.* **20**, 229–236 (2021).

133. Khodagholy, D. *et al.* In vivo recordings of brain activity using organic transistors. *Nat. Commun.* **4**, (2013).

134. Wang, T. *et al.* A chemically mediated artificial neuron. *Nat. Electron.* **5**, (2022).

135. Wu, J. *et al.* An off-the-shelf bioadhesive patch for sutureless repair of gastrointestinal defects. *Sci. Transl. Med.* **14**, (2022).

136. Someya, T., Bao, Z. & Malliaras, G. G. The rise of plastic bioelectronics. *Nature* **540**, 379–385 (2016).

137. Markvicka, E. J. *et al.* Materials and structural designs of stretchable conductors. *Chem. Soc. Rev.* **48**, 88–94 (2018).

138. Yuk, H., Lu, B. & Zhao, X. Hydrogel bioelectronics. *Chem. Soc. Rev.* **48**, 1642–1667 (2019).

139. Yuk, H., Wu, J. & Zhao, X. Hydrogel interfaces for merging humans and machines. *Nat. Rev. Mater.* **7**, 935–952 (2022).

140. Yang, C. & Suo, Z. Hydrogel ionotronics. *Nat. Rev. Mater.* **3**, 125–142 (2018).

141. Lu, B. *et al.* Pure PEDOT:PSS hydrogels. *Nat. Commun.* **10**, (2019).

142. Rivnay, J., Wang, H., Fenno, L., Deisseroth, K. & Malliaras, G. G. Next-generation probes, particles, and proteins for neural interfacing. *Sci. Adv.* **3**, (2017).

143. Won, D. *et al.* Digital selective transformation and patterning of highly conductive hydrogel bioelectronics by laser-induced phase separation. *Sci. Adv.* **8**, (2022).

144. Ohm, Y. *et al.* An electrically conductive silver–polyacrylamide–alginate hydrogel composite for soft electronics. *Nat. Electron.* **4**, 185–192 (2021).

145. Tan, P. *et al.* Solution-processable, soft, self-adhesive, and conductive polymer

composites for soft electronics. *Nat. Commun.* **13**, 358 (2022).

146. Zheng, L. *et al.* Conductance-stable liquid metal sheath-core microfibers for stretchy smart fabrics and self-powered sensing. *Sci. Adv.* **7**, eabg4041 28 (2021).

147. Park, J. E. *et al.* Rewritable, Printable Conducting Liquid Metal Hydrogel. *ACS Nano* **13**, 9122–9130 (2019).

148. Hao, X. P. *et al.* Self-Shaping Soft Electronics Based on Patterned Hydrogel with Stencil-Printed Liquid Metal. *Adv. Funct. Mater.* **31**, 2105481 (2021).

149. Park, J. E., Kang, H. S., Koo, M. & Park, C. Autonomous Surface Reconciliation of a Liquid-Metal Conductor Micropatterned on a Deformable Hydrogel. *Adv. Mater.* **32**, 2002178 (2020).

150. Kikuchi, K., Shimada, Y. & Utsumi, K. New high-density multilayer technology on PCB. *IEEE Trans. Adv. Packag.* **22**, 116–122 (1999).

151. Cariou, M. *et al.* Compact X-band filter based on substrate integrated coaxial line stubs using advanced multilayer PCB technology. *IEEE Trans. Microw. Theory Tech.* **65**, 496–503 (2017).

152. Chung, H. U. *et al.* Binodal, wireless epidermal electronic systems with in-sensor analytics for neonatal intensive care. *Science* **363**, 947 (2019).

153. Choi, Y. S. *et al.* A transient, closed-loop network of wireless, body-integrated devices for autonomous electrotherapy. *Science* **376**, 1006–1012 (2022).

154. Lee, K. H. *et al.* Mechano-acoustic sensing of physiological processes and body motions via a soft wireless device placed at the suprasternal notch. *Nat. Biomed. Eng.* **4**, 148–158 (2020).

155. Matsuhisa, N., Chen, X., Bao, Z. & Someya, T. Materials and structural designs of stretchable conductors. *Chem. Soc. Rev.* **48**, 2946–2966 (2019).

156. Dai, Y., Hu, H., Wang, M., Xu, J. & Wang, S. Stretchable transistors and functional circuits for human-integrated electronics. *Nat. Electron.* **4**, 17–29 (2021).

157. Kim, D. H. *et al.* Epidermal electronics. *Science* **333**, 838–843 (2011).

158. Xu, S. *et al.* Assembly of micro/nanomaterials into complex, three-dimensional architectures by compressive buckling. *Science* **347**, 154–159 (2015).

159. Libanori, R. *et al.* Stretchable heterogeneous composites with extreme mechanical gradients. *Nat. Commun.* **3**, 1265 (2012).

160. Matsuhisa, N. *et al.* Printable elastic conductors with a high conductivity for electronic textile applications. *Nat. Commun.* **6**, 7561 (2015).

161. Huang, Q. & Zheng, Z. Pathway to Developing Permeable Electronics. *ACS Nano* **16**, 15537–15544 (2022).

162. Dickey, M. D. Stretchable and Soft Electronics using Liquid Metals. *Adv. Mater.* **29**, 1606425 (2017).

163. Yan, J., Lu, Y., Chen, G., Yang, M. & Gu, Z. Advances in liquid metals for biomedical applications. *Chem. Soc. Rev.* **47**, 2518–2533 (2018).